

1 UNIVERSITY OF CALIFORNIA
2 SANTA CRUZ

3 **SEARCHES FOR ELECTROWEAK PRODUCTION OF**
4 **COMPRESSED SUPERSYMMETRY IN EVENTS WITH SOFT**
5 **LEPTONS PLUS MISSING TRANSVERSE MOMENTUM AND**
6 **HARD JET RECOIL**

7 A dissertation submitted in partial satisfaction of the
8 requirements for the degree of

9 DOCTOR OF PHILOSOPHY

10 in

11 PHYSICS

12 by

13 **Sheena Calie Schier**

14 June 2018

15 The Dissertation of Sheena Calie Schier
is approved:

16 Professor Abraham Seiden, Chair

18 Professor Jason Neilson

20 Professor Michael Hance

22 Dean Tyrus Miller
23 Vice Provost and Dean of Graduate Studies

25
26

27

28

Copyright © by

29

Sheena Calie Schier

30

2018

31

³² Table of Contents

³³ List of Figures	vi
³⁴ List of Tables	xiii
³⁵ Abstract	xv
³⁶ Dedication	xvi
³⁷ Acknowledgments	xvii
³⁸ 1 Introduction	1
³⁹ I Theoretical Motivation and Experimental Setup	2
⁴⁰ 2 Theoretical Background and Motivation	3
41 2.1 Forces and Particles	5
42 2.2 Gauge Symmetries and Spontaneous Symmetry Breaking	6
43 2.3 Shortcomings of the Standard Model	7
44 2.4 Supersymmetry	7
45 2.5 Phenomenology of Directly Produced Higgsinos and Sleptons in Com- 46 pressed Scenarios	8
47 2.5.1 Higgsino Simplified Models	9
48 2.5.2 Slepton Simplified Models	11
⁴⁹ 3 The LHC and The ATLAS Experiment	13
50 3.1 The Large Hadron Collider Machine	13
51 3.2 The ATLAS Experiment	17
52 3.2.1 Inner Tracking Detector	19
53 3.2.2 Calorimeters	21
54 3.2.3 Muon System	23
55 3.2.4 Trigger System	24

56	II Method	25
57	4 Data Collection and Simulated Events	26
58	4.1 Triggers	27
59	4.1.1 MET Triggers	27
60	4.1.2 Combined Trigger Studies	27
61	4.2 Data	29
62	4.3 Simulation	29
63	4.3.1 Signal samples	29
64	4.3.2 Background Simulation	35
65	4.4 Derivation	38
66	5 Physics Object Reconstruction and Identification	39
67	5.1 The Building Blocks	40
68	5.2 Particle Identification and Reconstruction	43
69	5.3 Treatment of Reconstructed Objects	47
70	6 Signal Region Optimization	52
71	6.1 Discriminating Variables	53
72	6.2 Optimization Studies	57
73	6.3 Slepton Signal Regions	60
74	6.4 Higgsino Signal Regions	60
75	6.5 Conclusion	61
76	7 Background Estimation	63
77	7.1 Summary of estimation strategy	63
78	7.2 Irreducible Backgrounds	66
79	7.2.1 Top Control Region (CR-top)	66
80	7.2.2 Dilepton Control Region (CR-tau)	69
81	7.2.3 Diboson Validation Region (VR-VV)	69
82	7.2.4 Different flavor validation regions	69
83	7.3 Drell-Yan Background	74
84	8 Fake Factor Method	75
85	8.1 Introduction	76
86	8.2 Description of Fake Factor Method	78
87	8.3 Fake Factor Method Applied to Low- p_T Di-lepton Events	80
88	8.3.1 Fake Lepton Composition	81
89	8.3.2 Anti-identified Lepton Definitions	85
90	8.3.3 Fake Factor Measurement	92
91	8.4 Conclusion	109

92	III Analysis and Results	110
93	9 Systematic Uncertainties	111
94	9.1 Experimental Uncertainties	111
95	9.1.1 CP Group Uncertainties	112
96	9.1.2 Fake Factor Uncertainties	113
97	9.2 Theoretical Uncertainties	115
98	9.2.1 Uncertainty on Simulated Signal Events	115
99	9.2.2 Uncertainty on Simulated Background Events	116
100	10 Statistical Analysis	121
101	10.1 Test Statistics and p-values	122
102	10.2 Fit and Nuisance Parameter Pull	125
103	11 Results	127
104	11.1 Background Only Fit	127
105	11.2 Model Independent Upper Limits on New Physics	131
106	11.3 Model Dependent Sensitivity with Shape Fit	132
107	12 Interpretations	134
108	12.1 Compressed Higgsino	139
109	12.2 Compressed Slepton	141
110	12.3 Compressed Wino	143
111	13 Conclusion	145
112	A Appendix A	146
113	A.1 Fake lepton composition study	146
114	B Appendix B	154
115	B.1 Control Region Plots	154

¹¹⁶ List of Figures

¹¹⁷ 2.1	Feynman diagram of direct Higgsino production	10
¹¹⁸ 2.2	Feynman diagram of direct Higgsino production in compressed scenario	11
¹¹⁹ 2.3	Feynman diagram of direct slepton production	12
¹²⁰ 3.1	Schematic of the LHC layout	15
¹²¹ 3.2	Cut-away view of the complete ALTAS Detector	18
¹²² 3.3	Layout of the ALTAS Inner Detector	19
¹²³ 3.4	Picture of the ALTAS Calorimeters	22
¹²⁴ 4.1	Trigger Efficiency as a function of MET after event preselection (left) and in a signal region similar to the analysis signal region (right)	28
¹²⁵ 4.2	Trigger efficiency as a function of MET for the combined single muon trigger (left) and the combined dimuon trigger (right)	28
¹²⁶ 4.3	Kinematic distributions of signal samples	33
¹²⁷ 4.4	Kinematic distributions of signal samples	34
¹²⁸ 5.1	Dilepton ΔR distribution before LepIsoCorrection (top) and after LepIsoCorrection (bottom) for the ee -channel (left) and $\mu\mu$ -channel (right).	49
¹²⁹ 5.2	Dilepton invariant mass distribution before LepIsoCorrection (top) and after LepIsoCorrection (bottom) for the ee -channel (left) and $\mu\mu$ -channel (right).	50
¹³⁰ 5.3	(left) Impact of the <code>NearbyLepIsoCorrection</code> tool on the efficiency of low-mass dilepton pairs in data. The data are shown in a region with $\Delta\phi(E_T^{\text{miss}}, p_t^{j1}) < 1.5$ to avoid the signal region. Events are triggered with the inclusive- E_T^{miss} trigger. The red trend shows events with two baseline leptons without applying any isolation; the green shows the impact of applying <code>GradientLoose</code> isolation; the blue shows the result of the <code>NearbyLepIsoCorrection</code> applied to the <code>GradientLoose</code> sample. (right) Impact of the correction on a Higgsino LSP signal sample with $\Delta m(\chi, \chi) = 3$ GeV.	51

144	6.1	Schematic illustrating the fully leptonic ($Z \rightarrow \tau\tau$) + jets system motivating the construction of $m_{\tau\tau}$	57
145	6.2	Comparison of Higgsino N2C1p (solid) and slepton (dashed) signals in the $R_{\ell\ell}$ variable for 10 GeV (dark) and 20 GeV (light) mass splittings. The E_T^{miss} here acts as a proxy for the boost of the system. Only a 2 signal lepton selection is applied.	59
146	6.3	Distributions of $E_T^{\text{miss}}/H_T^{\text{leptons}}$ for the Higgsino (left) and Slepton (right) selections, after applying all signal region cuts except those on the $E_T^{\text{miss}}/H_T^{\text{leptons}}$, m_{ll} , and m_{T2} . The black dashed line indicates the cut applied in the signal region; events in the region below the black line are rejected.	60
147	6.4	Normalized Cutflow for background-only, signal-inclusive, and non-normalized cutflow with significance plots.	62
148	7.1	CR-top $ee + \mu\mu + e\mu + \mu e$ channel, pre-fit distributions.	67
149	7.2	CR-top $ee + \mu\mu + e\mu + \mu e$ channel, pre-fit distributions.	68
150	7.3	CR-tau $ee + \mu\mu + e\mu + \mu e$ channel, pre-fit distributions.	70
151	7.4	CR-tau $ee + \mu\mu + e\mu + \mu e$ channel, pre-fit distributions.	71
152	7.5	VR-VV $ee + \mu\mu + e\mu + \mu e$ channel, pre-fit distributions.	72
153	7.6	VR-VV $ee + \mu\mu + e\mu + \mu e$ channel, pre-fit distributions.	73
154	7.7	Data events passing inclusive E_T^{miss} triggers with opposite sign baseline leptons in the dilepton invariant mass $m_{\ell\ell}$ spectrum. The $\Delta\phi(j_1, \mathbf{p}_T^{\text{miss}})$ variable is inverted to ensure this is orthogonal to the signal region.	74
155	8.1	Electron identification efficiency	78
156	8.2	Schematic illustrating the fake factor method to estimate the fake lepton contribution in the signal region.	80
157	8.3	Fake lepton composition as a function of leading and subleading lepton p_T , with and without prompt (“Isolated” plus “ $\text{lep} \rightarrow \text{gamma} \rightarrow \text{lep}$ ”) leptons, for opposite sign muon pairs in the signal region.	83
158	8.4	Fake lepton composition in opposite sign signal and control region as a function of leading and subleading lepton p_T , with and without prompt (“Isolated” plus “ $\text{lep} \rightarrow \text{gamma} \rightarrow \text{lep}$ ”) leptons, for opposite sign electron pairs in the signal region.	84
159	8.5	Anti-ID muon composition in events with exactly zero b -jets(left) and one or more b -jets(right) as a function of m_T , E_T^{miss} , muon p_T , and muon η . All but the m_T distribution corresponds to events with $m_T < 40 \text{ GeV}$	87
160	8.6	Fake electron composition as a function of m_T , E_T^{miss} , electron p_T , electron η . All distributions corresponds to events with $m_T < 40 \text{ GeV}$, excluding the m_T distribution.	89
161	8.7	Fake lepton composition as a function of the subleading lepton p_T	91

182	8.8 The E_T^{miss} (left) and m_T (right) distributions for numerator (top) and de-	
183	nominator (bottom) muons in the prescaled single-lepton-trigger sample	
184	for events with exactly zero b -jets. MC has been scaled to the data in	
185	the $E_T^{\text{miss}} > 200 \text{ GeV}$ region.	93
186	8.9 The E_T^{miss} (left) and m_T (right) distributions for numerator (top) and de-	
187	nominator (bottom) muons in the prescaled single-lepton-trigger sample	
188	for events with one or more b -jets. MC has been scaled to the data in	
189	the $E_T^{\text{miss}} > 200 \text{ GeV}$ region.	94
190	8.10 Muon p_T for numerator (left) and denominator (right) objects in the	
191	prescaled single-muon trigger sample for events with $m_T < 40 \text{ GeV}$. MC	
192	has been scaled to the data in the $m_T > 100 \text{ GeV}$ region. Distributions	
193	from [?].	95
194	8.11 Muon p_T for numerator (left) and denominator (right) objects in the	
195	prescaled single-muon trigger sample for events with $m_T < 40 \text{ GeV}$. MC	
196	has been scaled to the data in the $m_T > 100 \text{ GeV}$ region. Distributions	
197	from [?].	95
198	8.12 The numerator muon (left) and denominator denominator (right) p_T dis-	
199	tributions for prescaled single-muon triggers, normalized to 1 pb^{-1} . Blue	
200	curve: HLT_mu4, red curve: HLT_mu10, purple curve: HLT_mu14, green	
201	curve: HLT_mu18.	96
202	8.13 Muon fake factors <i>before</i> requiring a hard jet of $p_T > 100 \text{ GeV}$, computed	
203	from single-muon prescaled triggers as a function of muon p_T (top-left),	
204	as a function of leading jep p_T (top-right), and as a function of b -jet	
205	multiplicity (bottom). A red line denotes the average muon fake factor	
206	over all muon p_T	98
207	8.14 Muon fake factors computed from single-muon prescaled triggers as a	
208	function of muon p_T in events with exactly zero b -jets (left) and one	
209	or more b -jets (right). A red line denotes the average muon fake factor over	
210	all muon p_T	99
211	8.15 Muon fake factors computed from single-muon prescaled triggers as a	
212	function of muon η in events with exactly zero b -jets (left) and one	
213	or more b -jets (right). A red line denotes the average muon fake factor over	
214	all muon p_T	100
215	8.16 Muon fake factors computed from single-muon prescaled triggers as a	
216	function of $\Delta\phi_{jet-E_T^{\text{miss}}}$ in events with exactly zero b -jets (left) and one	
217	or more b -jets (right). A red line denotes the average muon fake factor over	
218	all muon p_T	100
219	8.17 Muon fake factors computed from single-muon prescaled triggers as a	
220	function of the jet multiplicity in events with exactly zero b -jets (left)	
221	and one or more b -jets (right). A red line denotes the average muon fake	
222	factor over all muon p_T	101

223	8.18 Muon fake factors computed from single-muon prescaled triggers as a function of the average number of interactions per bunch crossing in events with exactly zero b -jets (left) and one or more b -jets (right). A red line denotes the average muon fake factor over all muon p_T	101
224		
225		
226		
227	8.19 Muon fake factors computed from single-muon prescaled triggers as a function of the number of primary vertices in events with exactly zero b -jets (left) and one or more b -jets (right). A red line denotes the average muon fake factor over all muon p_T	102
228		
229		
230		
231	8.20 Relative uncertainties on muon fake factors versus muon p_T in zero b -jets bin (left) and one or more b -jets bin (right).	102
232		
233	8.21 The E_T^{miss} (left) and m_T (right) distributions for numerator (top) and denominator (bottom) electrons in the pre-scaled single-lepton-trigger sample. MC has been scaled to the data in the $E_T^{\text{miss}} > 200 \text{ GeV}$ region.	104
234		
235		
236	8.22 Electron p_T for numerator (left) and denominator (right) objects in the pre-scaled single-lepton-trigger sample for events with $m_T < 40 \text{ GeV}$. MC has been scaled to the data in the $E_T^{\text{miss}} > 200 \text{ GeV}$ region.	105
237		
238		
239	8.23 The numerator electron (left) and denominator electron (right) p_T distributions for pre-scaled single-lepton-trigger, normalized to 1 pb^{-1} . Blue curve: HLT_e5_lvhloose, red curve: HLT_e10_lvhloose_L1EM7, purple curve: HLT_e15_lvhloose_L1EM13, green curve: HLT_e20_lvhloose.	105
240		
241		
242		
243	8.24 Electron fake factors <i>before</i> requiring a hard jet of $p_T > 100 \text{ GeV}$, computed from single-electron prescaled triggers as a function of electron p_T (left) and leading jet p_T (right). Fake factors for electron p_T $4.5 - 5 \text{ GeV}$ are taken to be the same as electron p_T $5 - 6 \text{ GeV}$. A red line denotes the average electron fake factor over all electron p_T of 0.267.	106
244		
245		
246		
247		
248	8.25 Electron fake factors computed from single-electron prescaled triggers as a function of electron p_T (left) and electron η (right) in the kinematic region with leading jet $p_T > 100 \text{ GeV}$. Fake factors for electron p_T $4.5 - 5 \text{ GeV}$ are taken to be the same as electron p_T $5 - 6 \text{ GeV}$. A red line denotes the average electron fake factor over all electron p_T of 0.211.	107
249		
250		
251		
252		
253	8.26 Electron fake factors computed from single-electron prescaled triggers as a function of leading jet p_T (left) and $\Delta\phi_{jet-E_T^{\text{miss}}}$ (right). A red line denotes the average electron fake factor over all electron p_T of 0.211.	107
254		
255		
256	8.27 Electron fake factors computed from single-electron prescaled triggers as a function of the jet multiplicity (left) and the b -jet multiplicity (right). A red line denotes the average electron fake factor over all electron p_T of 0.211.	108
257		
258		
259		
260	8.28 Electron fake factors computed from single-electron prescaled triggers as a function of the average interaction per bunch crossing (left) and the number of primary vertices (right). A red line denotes the average electron fake factor over all electron p_T of 0.211.	108
261		
262		
263		
264	8.29 Relative uncertainties on electron fake factors binned electron p_T	109

265	9.1	QCD scale, α_s and PDF uncertainties on the shape and normalization of the diboson background in the Higgsino and slepton signal regions (with no lepton flavor requirement)	117
266	9.2	QCD scale, α_s and PDF uncertainties on the shape and normalization of the $Z \rightarrow \tau\tau$ background in the Higgsino and slepton signal regions (with no lepton flavor requirement)	118
267	9.3	QCD scale and PDF uncertainties on the shape and normalization of the $t\bar{t}$ background in the Higgsino and slepton signal regions (with no lepton flavour requirement)	119
268	9.4	Comparison of the $m_{\ell\ell}$ (left) and m_{T2} (right) shapes predicted by different $t\bar{t}$ (top) and VV (bottom) MC generators, in the Higgsino and slepton signal regions. All distributions are normalized to the same number of entries. The gray band displayed in the ratio pad under each distribution represents the modeling uncertainty assigned to each background in each of the bins.	120
270	10.1	Fit parameters for background-only fit in various configurations of the regions allowed to be treated as constraining.	126
272	11.1	Summary of Monte Carlo yields in control, validation and signal regions in a background-only fit using data only in the two CRs to constrain the fit.	128
274	11.2	Kinematic distributions after the background-only fit showing the data and the expected background in the different-flavor validation region VRDF- m_{T2}^{100} (top left), the diboson validation region VR-VV (top right), and the same-sign validation region VR-SS inclusive of lepton flavor (bottom). Similar levels of agreement are observed in other kinematic distributions for VR-SS and VR-VV. Background processes containing fewer than two prompt leptons are categorized as ‘Fake/nonprompt’. The category ‘Others’ contains rare backgrounds from triboson, Higgs boson, and the remaining top-quark production processes listed in Table. The last bin includes overflow. The uncertainty bands plotted include all statistical and systematic uncertainties. Orange arrows in the Data/SM panel indicate values that are beyond the y-axis range.	129
276	11.3	Kinematic distributions after the background-only fit showing the data as well as the expected background in the inclusive electroweakino SR $\ell\ell$ - $m_{\ell\ell}$ [1, 60] (top) and slepton	130

300	12.1 Comparison of observed and expected event yields after the exclusion fit with the signal strength parameter set to zero in the exclusive signal regions. Background processes containing fewer than two prompt leptons are categorized as ‘Fake/nonprompt’. The category ‘Others’ contains rare backgrounds from triboson, Higgs boson, and the remaining top-quark production processes listed in Table ???. Uncertainties in the background estimates include both the statistical and systematic uncertainties, where σ_{tot} denotes the total uncertainty.	138
301		
302		
303		
304		
305		
306		
307		
308	12.2 Expected 95% CL exclusion sensitivity (blue dashed line) with $\pm 1\sigma_{\text{exp}}$ (yellow band) from experimental systematics and observed limits (red solid) with $\pm 1\sigma_{\text{theory}}$ (dotted red) from signal cross section uncertainties. A shape fit of Higgsino signals to the $m_{\ell\ell}$ spectrum is used to derive the limit is displayed in the $m(\tilde{\chi}_2^0) - m(\tilde{\chi}_1^0)$ vs $m(\tilde{\chi}_2^0)$ plane. The chargino $\tilde{\chi}_1^\pm$ mass is assumed to be half way between the two lightest neutralinos. The grey region denotes the lower chargino mass limit from LEP [?].	140
309		
310		
311		
312		
313		
314		
315	12.3 Expected 95% CL exclusion sensitivity (blue dashed line) with $\pm 1\sigma_{\text{exp}}$ (yellow band) from experimental systematics and observed limits (red solid) with $\pm 1\sigma_{\text{theory}}$ (dotted red) from signal cross section uncertainties. A shape fit of slepton signals to the $m_{T_2}^{100}$ spectrum is used to derive the limit projected into the $m(\tilde{\ell}) - m(\tilde{\chi}_1^0)$ vs $m(\tilde{\ell})$ plane. The slepton $\tilde{\ell}$ refers to a 4-fold mass degenerate system of left- and right-handed selectron and smuon. The grey region denotes a conservative right-handed smuon $\tilde{\mu}_R$ mass limit from LEP [?], while the blue region is the 4-fold mass degenerate slepton limit from ATLAS Run 1 [?].	142
316		
317		
318		
319		
320		
321		
322		
323		
324	12.4 Expected 95% CL exclusion sensitivity (blue dashed line) with $\pm 1\sigma_{\text{exp}}$ (yellow band) from experimental systematic uncertainties and observed limits (red solid line) with pm1?theory (dotted red line) from signal cross-section uncertainties for simplified models direct wino production. A shape fit of wino signals to the $m_{\ell\ell}$ spectrum is used to derive the limit is displayed in the $m(\tilde{\chi}_2^0) - m(\tilde{\chi}_1^0)$ vs $m(\tilde{\chi}_2^0)$ plane. The chargino $\tilde{\chi}_1^\pm$ mass is assumed equal to the $m(\tilde{\chi}_2^0)$ mass. The grey region denotes the lower chargino mass limit from LEP [?], and the blue region in the lower plot indicates the limit from the $2\ell+3\ell$ combination of ATLAS Run 1.	144
325		
326		
327		
328		
329		
330		
331		
332		
333	A.1 Fake lepton composition in opposite sign signal and control region as a function of leading and subleading lepton p_T , with and without prompt (“Isolated” plus “lep \rightarrow gamma \rightarrow lep”) leptons, for opposite sign electron pairs in the signal region.	147
334		
335		
336		
337	A.2 Fake lepton composition as a function of leading and subleading lepton p_T , with and without prompt (“Isolated” plus “lep \rightarrow gamma \rightarrow lep”) leptons, for opposite sign electron pairs in the signal region.	148
338		
339		

340	A.3	Fake lepton composition as a function of leading and subleading lepton p_T , with and without prompt (“Isolated” plus “ $\text{lep} \rightarrow \text{gamma} \rightarrow \text{lep}$ ”) leptons, for same sign electron pairs in the signal region.	149
341			
342			
343	A.4	Fake lepton composition as a function of leading and subleading lepton p_T , with and without prompt (“Isolated” plus “ $\text{lep} \rightarrow \text{gamma} \rightarrow \text{lep}$ ”) leptons, for opposite sign muon pairs in the signal region.	150
344			
345			
346	A.5	Fake lepton composition as a function of leading and subleading lepton p_T , with and without prompt (“Isolated” plus “ $\text{lep} \rightarrow \text{gamma} \rightarrow \text{lep}$ ”) leptons, for opposite sign muon pairs in the fake lepton control region.	151
347			
348			
349	A.6	Fake lepton composition as a function of leading and subleading lepton p_T , with and without prompt (“Isolated” plus “ $\text{lep} \rightarrow \text{gamma} \rightarrow \text{lep}$ ”) leptons, for same sign muon pairs in the signal region.	152
350			
351			
352	A.7	Fake lepton composition as a function of leading and subleading lepton p_T , with and without prompt (“Isolated” plus “ $\text{lep} \rightarrow \text{gamma} \rightarrow \text{lep}$ ”) leptons, for same sign muon pairs in the fake lepton control region.	153
353			
354			
355	B.1	CR-top $ee + \mu\mu + e\mu + \mu e$ channel, pre-fit distributions.	155
356	B.2	$m_T^{\ell_1} + m_T^{\ell_2}$	156
357	B.3	CR-top $ee + \mu\mu + e\mu + \mu e$ channel, pre-fit distributions.	156
358	B.4	m_{T2}^{100}	157
359	B.5	CR-top $ee + \mu\mu + e\mu + \mu e$ channel, pre-fit distributions.	157
360	B.6	CR-tau $ee + \mu\mu + e\mu + \mu e$ channel, pre-fit distributions.	158
361	B.7	CR-tau $ee + \mu\mu + e\mu + \mu e$ channel, pre-fit distributions.	159
362	B.8	CR-tau $ee + \mu\mu + e\mu + \mu e$ channel, pre-fit distributions.	160
363	B.9	VR-VV $ee + \mu\mu + e\mu + \mu e$ channel, pre-fit distributions.	161
364	B.10	VR-VV $ee + \mu\mu + e\mu + \mu e$ channel, pre-fit distributions.	162
365	B.11	VR-VV $ee + \mu\mu + e\mu + \mu e$ channel, pre-fit distributions.	163

366 List of Tables

<small>367</small>	4.1 Evolution of lowest unprescaled E_T^{miss} trigger from the start of 2015 to the end of 2016. <small>add run numbers and integrated lumi for each trigger</small> .	<small>27</small>
<small>368</small>		
<small>369</small>	5.1 Summary of blah blah	<small>43</small>
<small>370</small>	5.2 Summary of object definitions	<small>46</small>
<small>371</small>	7.1 Background estimation summary	<small>66</small>
<small>372</small>	8.1 Pre-scaled single-lepton triggers from 2015 and 2016 used to compute the lepton fake factors. The pre-scaled luminosities shown are taken from <code>LumiCalc</code>	<small>81</small>
<small>373</small>		
<small>374</small>	8.2 Summary of muon definitions.	<small>86</small>
<small>375</small>		
<small>376</small>	8.3 Summary of electron definitions.	<small>88</small>
<small>377</small>		
<small>378</small>	8.4 Single-muon triggers used for fake factor computation and their corre- sponding p_T range.	<small>97</small>
<small>379</small>		
<small>380</small>	8.5 Single-Electron triggers used for fake factor computation and their cor- responding p_T range.	<small>103</small>
<small>381</small>		
	11.1 Breakdown of yields and upper limits.	<small>133</small>
<small>382</small>	12.1 Observed event yields and exclusion fit results with the signal strength parameter set to zero for the exclusive electroweakino and slepton signal regions. Background processes containing fewer than two prompt leptons are categorized as ‘Fake/nonprompt’. The category ‘Others’ contains rare backgrounds from triboson, Higgs boson, and the remaining top- quark production processes listed in Table ???. Uncertainties in the fitted background estimates combine statistical and systematic uncertainties. .	<small>136</small>
<small>383</small>		
<small>384</small>		
<small>385</small>		
<small>386</small>		
<small>387</small>		
<small>388</small>		

- 389 12.2 Observed event yields and exclusion fit results with the signal strength
390 parameter set to zero for the exclusive electroweakino and slepton signal
391 regions. Background processes containing fewer than two prompt leptons
392 are categorized as ‘Fake/nonprompt’. The category ‘Others’ contains
393 rare backgrounds from triboson, Higgs boson, and the remaining top-
394 quark production processes listed in Table ???. Uncertainties in the fitted
395 background estimates combine statistical and systematic uncertainties. . 137

Abstract

397 Searches for Electroweak Production of Compressed Supersymmetry in Events
398 with Soft Leptons Plus Missing Transverse Momentum and Hard Jet Recoil

399 by

400 Sheena Calie Schier

401 Supersymmetry (SUSY) is an extension of the Standard Model that predicts a boson
402 (fermion) partner for each fermion (boson) in the Standard Model. Weak scale SUSY
403 is attractive for reasons like improving gauge coupling unification, reducing fine-tuning
404 in the Higgs sector and providing a dark matter candidate. In this thesis, I present a
405 dedicated search for direct production of new colorless weak scale states in a compressed
406 mass spectra with final states characterized by soft visible decay products. This anal-
407 ysis uses pp collisions at $\sqrt{s} = 13$ TeV at the Large Hadron Collider and collected by
408 the ATLAS experiment during 2015 and 2016 corresponding to 36.1 fb^{-1} of integrated
409 luminosity. This analysis selects events with two soft electrons or muons and missing
410 transverse momentum (E_T^{miss}) recoiling against hadronic initial state radiation. Back-
411 grounds from $t\bar{t}$, diboson, and other production mechanisms with prompt leptons are
412 estimated with Monte Carlo simulation while reducible backgrounds with instrumental
413 E_T^{miss} and fake/non-prompt leptons is estimated with a mix of Monte Carlo and data-
414 driven methods. Results are consistent with Standard Model expectation and limits on
415 compressed supersymmetric states are extended for the first time since LEP.

416

To my father,

417

Lecil Charles Schier,

418

the person who taught me at the age of 7 that the grass in not green.

Acknowledgments

420 I want to “thank” my committee, without whose ridiculous demands, I would have

421 graduated so, so, very much faster.

422 **Chapter 1**

423 **Introduction**

424 Since the 1930's, when the world's first particle accelerator went online at
425 the Cavendish Laboratory in Cambridge, England, colliding protons against a fixed
426 lithium target, high energy collisions have been proving physicists with portals into the
427 subatomic realm where quantum physics is the supreme ruler. Progressively, particle
428 accelerators have become more and more powerful, and the depth at which physicists
429 can peer into the atom, into the structure of particles, and eventually into interactions of
430 the most fundamental, has hastened. Today, we stand at the energy frontier of particle
431 experiments with a complete map of fundamental particles and interactions in hand to
432 guide us through the sea of quantum possibilities, while astronomical observations, for
433 one, give us the distinct sense that we are holding only a small slice of the truth.

434 Currently, the Large Hadron Collider (LHC) is the largest and most powerful
435 accelerator on Earth, colliding protons with a center of mass energy of 13 TeV. With
436 this machine, we step into the realm of Big Bang physics, where all possibilities

437

Part I

438

Theoretical Motivation and

439

Experimental Setup

440 Chapter 2

441 Theoretical Background and Motivation

442 To any curious mind staring into the starry deep late in the night or gazing at
443 pictures from the Hubble Space Telescope, the universe can seem deeply mysterious as
444 a vast space containing a rich spectra of matter moving and transforming via some set
445 of complex mechanisms. Although this mysterious sense of the universe rings true even
446 in the mind of the most learned physics scholar, large leaps in understanding the true
447 nature of the matter and forces that make up the observable universe have been made
448 in human history. In the last century, particle physicists have constructed a theory that
449 incorporates all the directly observed fundamental particles and explains their existence
450 and interactions in simplicity through the field equations that describe the fundamental
451 forces in the universe. This theory is called the Standard Model of Particle Physics (SM)
452 and, apart from gravity being far too weak to be described by particle interactions, is
453 fundamentally complete. mention here to discovery of the Higgs boson in 2012, and
454 it confirming the theory of electroweak symmetry breaking, which remained the last

455 undiscovered piece of the SM puzzle.

456 But the story doesn't end here. There are reasons to think the complete and
457 successful Standard Model is a lower-order version of a much larger theory. Some of
458 these reasons are philosophical in nature; we want to understand why the SM has its
459 structure, or lack confidence in a theory that is so incredibly fine-tuned as the Standard
460 Model. Other reasons come from observations that we can not resolve with the SM,
461 like the lack of CP-violation in Standard Model mechanics to account for the baryon-
462 antibaryon asymmetry in the early universe, or the abundance of 'dark matter' that
463 drives massive galaxies to rotate contrary to predictions by models accounting only for
464 the known matter and forces of the Standard Model.

465 The proceeding structure of this chapter is as follows: Section 2.1, summarizes
466 all the forces and particles in the standard model, then Section 2.2 , describes the gauge
467 symmetries that give the Standard Model its particular structure and spontaneous elec-
468 troweak symmetry breaking that calls for the existence of the Higgs boson. Section 2.3
469 goes over some of the shortcomings of the Standard Model, and supersymmetry is intro-
470 duced in Section 2.4 as a viable model for physics beyond the Standard Model. Lastly,
471 Section 2.5 describes the phenomenology of supersymmetric Higgsinos and sleptons in
472 compressed scenarios.

473 2.1 Forces and Particles

474 The Standard Model of Particle Physics provides a quantum description of
475 three of the four known fundamental forces; the electromagnetic force, the strong force,
476 and the weak force. It leaves out the gravitational force because the energy scale at which
477 gravity does its business is many orders of magnitude below the other forces, which leads
478 to intrinsic incompatibilities in a description of quantum gravitational interactions. The
479 SM was pieced together throughout the second half of the twentieth century by several
480 progressive discoveries, and we now know that there are only a hand full of fundamental
481 particles that make up the incredible collection of particles in nature. The fundamental
482 particles separate into two distinct categories: fermions and bosons. These two types of
483 particles are characterized by their spin and interactions, and ultimately play completely
484 different roles in the state and phenomena of the universe. [?]

485 Fermions fall into two categorized, leptons and quarks. Leptons are spin $\frac{1}{2}$
486 particles that do not carry strong color charge, but they do carry electromagnetic charge
487 and weak isospin. The lepton group consists of three generations of electron and anti-
488 electron (e^\pm, μ^\pm, τ^\pm) and their associated neutrino and anti-neutrino partners
489 ($\nu_e/\tilde{\nu}_e, \nu_\mu/\tilde{\nu}_\mu, \nu_\tau/\tilde{\nu}_\tau$). Quarks are strongly charged particles that also carry weak isospin
490 and fractional electromagnetic charge. Like the leptons, there are three quark families,
491 each forming an isospin doublet and consisting of an up-type and a down-type quark:
492 (u,d), (c, s), (t,b).

493 Bosons are integer spin particles that are often called force-carriers because

494 they are responsible for mediating interactions between particles.

495 *Include one table that summarizes and categorizes all fermions and bosons.*

496 2.2 Gauge Symmetries and Spontaneous Symmetry Break- 497 ing

498 The main ingredients of the Standard Model are a set of Dirac fermion fields

499 having specific multiplet representations in group theory given by the $U(1)_Y \times SU(2)_L \times$

500 $SU(3)_S$ gauge group. In SM quantum field theory (QFT), called the "Yang Mills theory"

501 [reference here](#), fermion interactions are mediated by gauge bosons. The structure of the

502 gauge bosons and the interactions they govern is a consequence of gauge invariance in

503 $SU(n)$ type Lie groups [find reference](#).

504 Gauge invariance in QFT demands the existence of gauge boson fields, which

505 occur in two independent sectors: the electroweak sector described by quantum elec-

506 troweak dynamics (QED), and the strong sector, described by quantum chromodynam-

507 ics (QCD). The $U(1) \otimes SU(2)$ symmetry of QED produces the photon and the weak

508 gauge bosons, W^\pm and Z^0 , and the $SU(3)$ symmetry produces a color octet of massless

509 gluons. For the symmetries to be exact, all the force carriers must be massless, and

510 an external mechanism called the *Higgs mechanism* induces masses in the electroweak

511 gauge bosons, W^\pm and Z^0 . To quantize this exchange, an extra boson called the Higgs

512 boson must exist, and its discovery at the LHC was recently announced in June 2012.

513 Electrodynamics is 'gauge-invariant', meaning one obtains the same solutions

514 to Maxwell's equations under a transformation of the electromagnetic 4-vector potential:

515 $A_\mu \rightarrow A_\mu - \partial_\mu \Lambda$, where Λ is some scalar function. Under this gauge transformation, the

516 wave function changes by a phase $\psi \rightarrow \psi e^{-ie\Lambda}$, revealing a $U(1)$ symmetry.

517 2.3 Shortcomings of the Standard Model

518 As mentioned before, the Standard Model of Particle Physics in all its glory

519 has some deficiencies. **List and briefly explain.**

520 One alarming problem with the Standard Model is its incapability to explain

521 dark matter.

522 2.4 Supersymmetry

523 Supersymmetry offers an extension to the Standard Model by extending the

524 Poincare symmetry of quantum field theory. This extension leads to boson-fermion

525 symmetry which predicts a supersymmetric partner for all standard model partners

526 that are equivalent in mass and all quantum characteristics but differ intrinsically by

527 half-integer spin. So, each SM fermion has a bosonic supersymmetric partner, and

528 each SM boson has a fermionic supersymmetric partner. According to this symmetry,

529 assuming it is a perfect symmetry, these particles should have already been observed

530 with their SM masses, but this is not the case. In order for this theory to remain true,

531 the new symmetry must be broken in a way that preserves the fermion-boson symmetry

532 and all observations of the Standard Model while allowing fermion-boson partners to be

533 decoupled in mass. A description of the various models for mediating this symmetry-
534 breaking and communicating it the visible sector of observable particles is beyond the
535 scope of this thesis, but I will say a few words about electroweak symmetry breaking
536 models since they are the focus of this thesis.

537 Add a SUSY picture and make sure I have at least alluded to all the particles.

538 Explain about electroweak symmetry breaking

539 Talk about winos, binos, and Higgsinos and how they mix to make up the
540 charginos and neutralinos.

541 Explain about naturalness in electroweak SUSY and how this would make the
542 Higgsino light, at the electroweak scale, and how the winos and binos, with masses given
543 by M_1 and M_2 , can still be heavy.

544 *Try* to explain how the electroweakino mass spectrum works and that the more
545 Higgsino like they are the smaller the mass-splittings become, until pure Higgsino states
546 are completely degenerate

547 **2.5 Phenomenology of Directly Produced Higgsinos and**
548 **Sleptons in Compressed Scenarios**

549 Say here a word or two about how these two searches are so similar they are
550 combined into one search effort with minor differences in their search strategies.

551 **2.5.1 Higgsino Simplified Models**

552 Higgsinos are the superpartners of the Standard Model Higgs doublets, the
553 masses of which are controlled by the μ parameter, which, in supersymmetry, enters
554 directly into the Higgs mass mixing matrix for calculating the squared Higgs mass M_H^2 .

555 [?] Naturalness of the Higgsinos refers to the fact that in order for electroweak symmetry
556 breaking to occur at the correct scale without any unnatural corrections, the parameter
557 μ must be near the weak scale ≈ 100 GeV.. Other supersymmetric particles enter the
558 mass matrix indirectly through quantum loop corrections, but the Higgsinos are the
559 only particle to have a direct effect on the Higgs mass. This make Higgsinos a powerful
560 tool in understanding electroweak symmetry breaking in SUSY.

561 Could search for Higgsinos through direct production of squarks that then
562 decay to Higgsinos, but these particles have little effect on the mass of the Higgs and
563 therefor, may naturally have masses well beyond the reach of the LHC. Also, Higgsino
564 models are very sensitive to the spectrum of light SUSY particles when trying to observe
565 them through direct squark production.

566 Direct Higgsino production allows one to remain fairly agnostic to the spectrum
567 of the SUSY sector, and therefore, retain sensitivity to a large range of EWSB SUSY
568 models. Unfortunately, the direct production of electroweakinos, including Higgsinos,
569 is subject to electroweak cross-sections, limiting the search sensitivity at the LHC.
570 Refer to the Feynman diagram in Figure 2.3. When the mass differences between the
571 electroweakinos are close to mass of the W boson, Standard Model W and Z bosons are

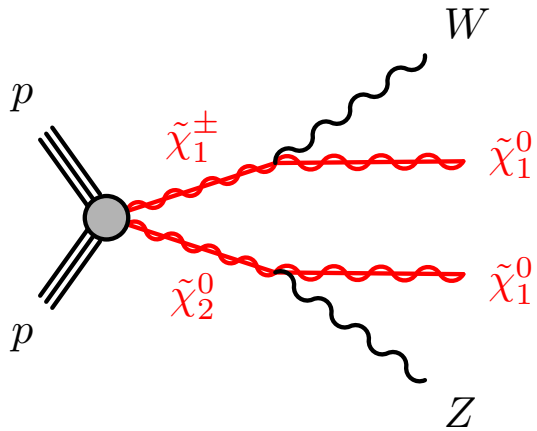


Figure 2.1: Feynman diagram of direct Higgsino production

572 produced on-shell, or produced at their nominal masses, and about 30% of the time will
 573 decay leptonically, subsequently giving birth to detectable leptons. In this case, analyses
 574 have been performed in both ATLAS and CMS to search for all three leptons from the
 575 W and Z , where the Z can be reconstructed from an opposite-sign-same-flavor lepton
 576 pair. The searches also require a substantial amount of missing transverse momentum
 577 from the lightest neutral electroweakinos.

578 When the mass-splittings fall below the W mass, the W and Z bosons are
 579 produced off-shell, they are lighter than their nominal 80–90 GeV mass, and the leptons
 580 from these decays become softer, or less energetic. This type of analysis is limited by
 581 how well these events are recorded, and how efficiently leptons are reconstructed at low
 582 energies. Until recently, no experiment at the LHC has been able to search for these
 583 models with electroweakino mass-splittings below ≈ 60 GeV. **Introduce the 2 lepton**
 584 **search and the Feynman diagram.**

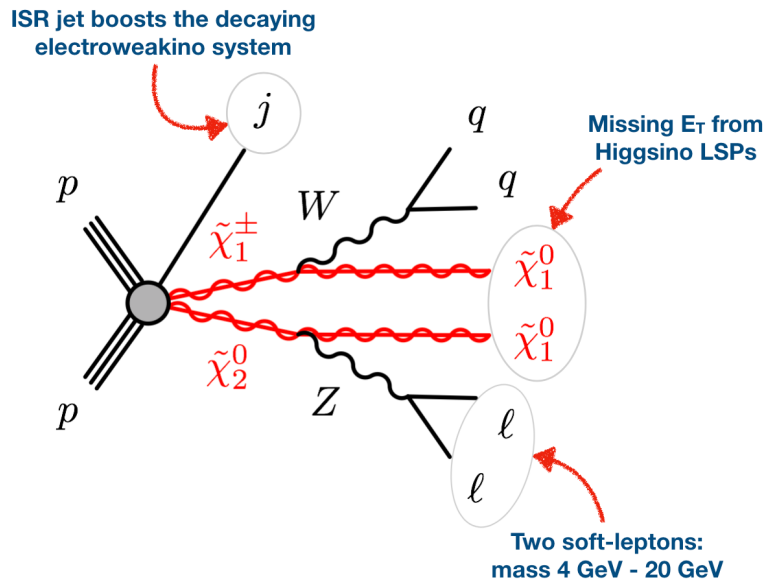


Figure 2.2: Feynman diagram of direct Higgsino production in compressed scenario

585 *Say something before here about using simplified models.* One important kinematic feature in these Higgsino simplified models is the dilepton invariant mass distribution and how it is linked to the mass-splitting between the chargino and the lightest neutralino through the mass of the very off-shell Z .

589 **2.5.2 Slepton Simplified Models**

590 Explain slepton models and direct production of sleptons
 591 Talk about searches for models with large mass-splittings and how there is redundancy with the Higgsino models in why these searches have not been available
 592 for models with small mass-splitting between the sleptons, which assume a fourfold degeneracy, and the lightest neutral electroweakino.

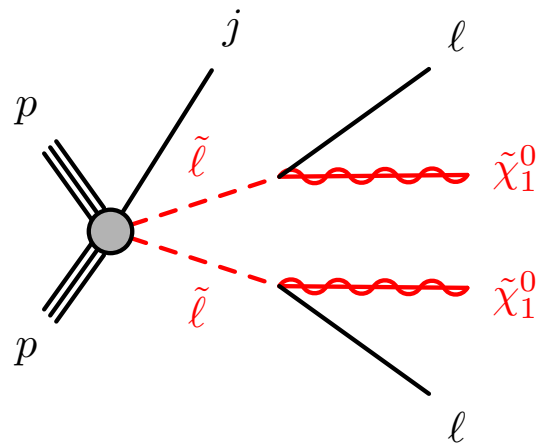


Figure 2.3: Feynman diagram of direct slepton production

595

Talk about the $mT2$ variable and why is s great discriminator for these signals.

596 **Chapter 3**

597 **The LHC and The ATLAS Experiment**

598 This chapter gives an overview of the LHC and the ATLAS detector used for
599 this physics analysis. First, the LHC is introduced in Section 3.1, then a review of the
600 ATLAS detector in Section 3.2. This section is broken into smaller pieces that detail
601 the ATLAS subdetectors and trigger system.

602 **3.1 The Large Hadron Collider Machine**

603 The Large Hadron Collider (LHC) is a circular proton accelerator and collider
604 at CERN, operating in the 26.7 km long tunnel that was originally built for the CERN
605 LEP machine. In the tunnel, there are two separate vacuum beam pipes with counter-
606 rotating proton beams that are accelerated to the TeV energy scale by a gigantic semi-
607 conducting magnet system. To reach LHC energies, the proton beams first move through
608 a stream of smaller accelerator structures that increase the kinetic energy of the beam
609 at each step, until the beam is finally injected into the LHC, which is still, at the

610 completion of this thesis, the largest and most powerful accelerator in the world. There
611 are two transfer tunnels, each about 2.5 km long, that join the LHC to the CERN
612 accelerator complex, now acting as the injector for the LHC. The LHC tunnel is broken
613 into octets with eight straight sides and eight curves. This is not an LHC design, but
614 rather an artifact of LEP. That being said, each octet is considered as a reference point
615 around the ring; for instance, octet 1 is "point 1", octet 2 is "point 2" and so on.
616 The beams collide at four interaction points located approximately 100m underground,
617 and surrounding each interaction point is a physics detector apparatus to collect data
618 from the proton collisions. The four different detector experiments are ALICE, LHC-B,
619 CMS, and ATLAS. Figure 3.1 depicts the tunnel octets and the beam injection and
620 dump points. It also shows the placement of the four detectors; ATLAS is located at
621 point 1.

622 The primary objective of the LHC is find the Higgs boson, which was discovered
623 by both ATLAS and CMS in 2012, and to expose Beyond Standard Model (BSM)
624 physics. To attempt these goals, the accelerator was designed to supply proton collisions
625 with enough center of mass energy to produce a Higgs with mass above 100 GeV and
626 to unlock possible new physics interactions at the 100 GeV – 1 TeV scale. The initial
627 aim was a proton-proton center of mass energy of 14 TeV, but due to instabilities in
628 the magnet system at such high energy, only 13 TeV has successfully been achieved.
629 Many BSM theories predict new particle interactions with weak-scale cross-sections or
630 lower, creating the need enough luminosity to measure these low probability events.
631 The machine luminosity depends only on beam parameters, as expressed in Eq 3.1.

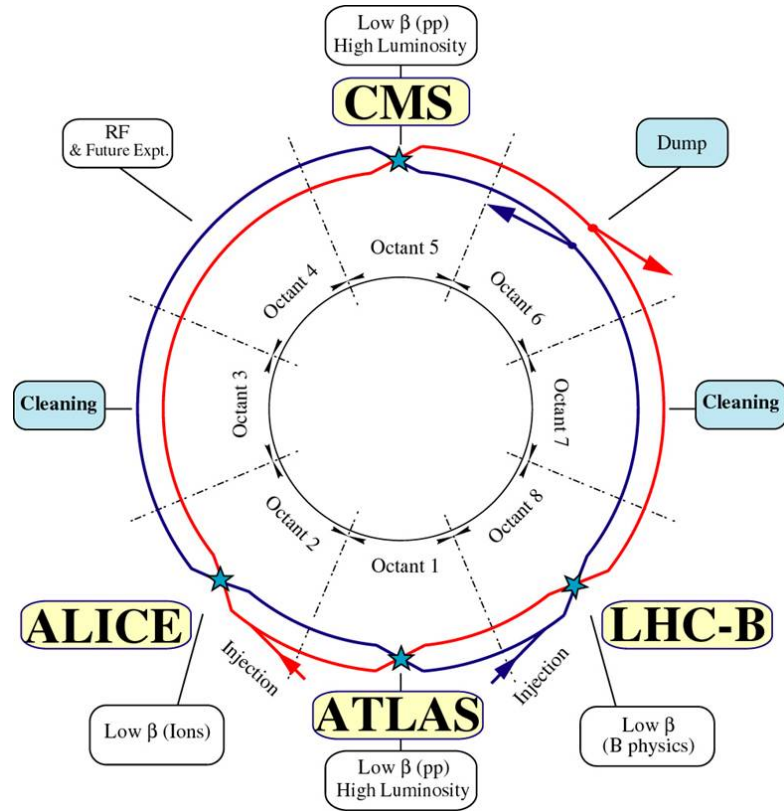


Figure 3.1: Schematic of the LHC layout

$$L = \frac{N_b^2 n_b f_{rev} \gamma_r}{4\pi \epsilon_n \beta^*} F \quad (3.1)$$

632 In the numerator of Eq 3.1, N_b is the number of particles per bunch, n_b is the number
 633 of bunches per beam, f_{rev} is the revolution frequency, and γ_r is the relativistic gamma
 634 factor of the highly relativistic beam particles traveling near the speed of light. In the
 635 denominator of Eq 3.1, ϵ_n is the normalized transverse beam emittance and β^* in the
 636 beta function at the collision point. F is the geometric luminosity reduction factor due
 637 to the beams crossing at an angle at the interaction points rather than directly head-on:

$$F = \left(1 + \left(\frac{\Theta_c \sigma_z}{2\sigma^*}\right)^2\right)^{-1/2} \quad (3.2)$$

638 Θ_c is the full crossing angle at the interaction point, σ_z is the RMS bunch length,
 639 and σ^* is the transverse RMS beam size at the interaction point. ATLAS, one of the
 640 high luminosity experiments at the LHC, achieved a peak luminosity in 2016 above
 641 $L = 10^{34} \text{ cm}^2 \text{s}^{-1}$.

642 The general design for detectors at the LHC is informed by the benchmark
 643 physics goals and the experimental environment and constraints. The high energy and
 644 luminosity demands make radiation-hard sensor elements and read-out electronics a
 645 necessity. Large numbers of interactions per bunch crossing, called pileup, creates the
 646 need for highly granular detectors to resolve the separate events in space. To search
 647 for new physics, a detector needs to be as general as possible, meaning it tries to see
 648 everything. This requires a high acceptance in pseudorapidity with coverage over nearly
 649 the full azimuthal angle of the detector, high track reconstruction efficiency and good

650 resolution on charged-particle momentum measurements. Fairly precise electromagnetic
651 calorimetry is also needed for efficient electron and photon identification. Now that we
652 understand these demands, we turn to a description of the ATLAS detector

653 3.2 The ATLAS Experiment

654 The ATLAS experiment is a general purpose detector apparatus that almost
655 completely covers the entire solid angle around one of the LHC beam collision points.
656 ATLAS recorded its first LHC pp collisions in 2009 at center of mass energy 7 TeV , and
657 has since recorded events at several different center of mass energies, including the most
658 extensive energy reach in the history at 13 TeV . ATLAS achieves central coverage in the
659 symmetric cylindrical barrel, and forward-backward detecting capabilities in the end-
660 caps. The complete detector system is 44m long, 25m in diameter, and weighs 4000 tons.
661 The ATLAS detector, shown in Figure 3.2, is comprised of several sub-detector systems,
662 each calibrated and optimized for a different observational purpose. The sub-detectors,
663 listed in order from the beam pipe outward, are: the inner tracking detector (ID), the
664 electromagnetic calorimeter (eCAL), the hadronic calorimeter (hCAL), and the muon
665 spectrometer (MS). Together, these sub-detectors measure the energy and momentum
666 of a variety of particles and reconstruct the dynamics of each recorded event.

667 ATLAS uses a right-handed coordinate system with the center of the detector
668 as the origin. The z-axis runs through the center of the barrel along the beam pipe, and
669 the y-axis points upward through the barrel from the origin. The x-axis points outward

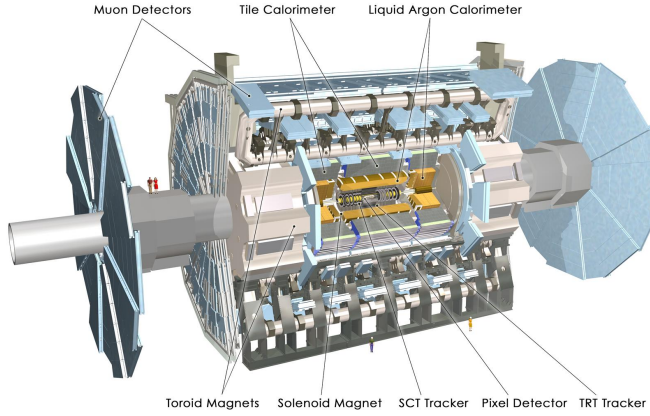


Figure 3.2: Cut-away view of the complete ALTAS Detector

670 from the origin, perpendicular to both the y- and z-axes. Cylindrical coordinates (r, ϕ)
 671 map out the transverse plane, where r is the radius in the plane, and ϕ is the azimuthal
 672 angle around the z-axis. The pseudorapidity η , given by Eq 3.3 is a transformation of
 673 the polar angle that is commonly used in particle detector experiments. At $\theta = \pi/2$,
 674 $\eta = 0$; at $\theta = \pi/18$, $\eta = 2.88$; as θ approaches zero, η approaches infinity.

$$\eta = -\ln[\tan(\theta/2)] \quad (3.3)$$

675 The combination of the detector systems provide charged particle measurements and
 676 efficient lepton and photon measurements out to $|\eta| < 2.4$. Jets and MET are recon-
 677 structed using the full set of information out to $|\eta| < 4.9$.

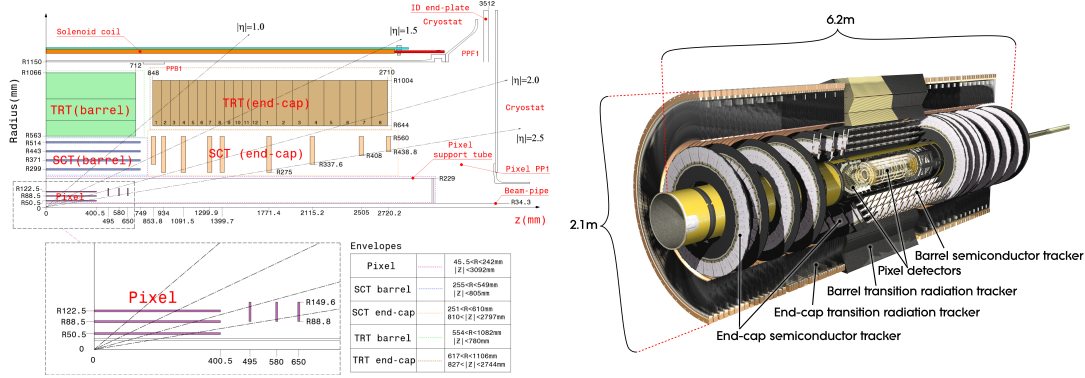


Figure 3.3: Layout of the ALTAS Inner Detector

678 3.2.1 Inner Tracking Detector

679 The ATLAS Inner Detector (ID), show in Figure 3.3, provides position mea-
 680 surements of charged particles passing through the fiducial region $|\eta| < 2.5$ by com-
 681 bining information from three separate tracking systems; the Pixel detector, the Semi-
 682 Conductor Tracker (SCT), and the Transition Radiation Tracker (TRT). The ID is made
 683 of a central cylindrical barrel that covers the region $|\eta| < 1.5$, and two end-caps that
 684 complete the ID range $1.5 < |\eta| < 2.5$. The ID is surrounded by a superconducting
 685 solenoid that encases the entire ID in a 2 Tesla magnetic field. The 2 T magnetic field
 686 bends the charged particles traveling through the tracker and the induced curvature
 687 is driven by the momentum of the particle. Add mathematical description of how the
 688 momentum is calculated from the curvature and the momentum?

689 The Pixel detector is the inner most pixelated tracker and has the highest
 690 granularity sensors in the ID. There are three pixel layers in the central barrel and three
 691 layers in each end cap, providing up to three space-points per track. The Pixel detector

692 has approximately 80.4 million readout channels bonded to pixel sensors segmented in
693 the $R-\phi$ and z directions. The Pixel sensors have dimensions $50\mu m \times 400\mu m$ in $R-\phi \times z$,
694 and provide an intrinsic resolution of $10\mu m$ in $R - \phi$ and $115\mu m$ along z . Besides
695 mitigating the effects of pileup, the high granularity of the Pixel detector also helps
696 discriminate prompt from non-prompt leptons in cases where a heavy mesonic decay,
697 producing a non-prompt lepton, happens after entering the ID. The rich granularity
698 helps resolve secondary vertices formed by the charged decay products.

699 The Semi-Conductor Tracker (SCT) is a silicon micro-strip tracker just outside
700 of the the Pixel detector, with an overall radial extension of $255\text{ mm} < R < 549\text{ mm}$ in
701 the barrel and $251\text{ mm} < R < 610\text{ mm}$ in the end-caps. It has eight paired strip layers
702 that provide four space points per track. In the barrel (end-cap), one set of strips is
703 aligned parallel (perpendicular) the beam axis and is daisy chained to a second set of
704 strips, each misaligned with the its partner by a 40 mrad stereo angle. The strip pitch
705 is $80\text{ }\mu m$. The resulting intrinsic resolution in both the barrel and the end-caps is $17\text{ }\mu m$
706 in $R - \phi$, and in the barrel (end-caps) it is $580\text{ }\mu m$ in z (R). There are approximately
707 6.3 million readout channels.

708 The Transition Radiation Tracker (TRT) is the outer most detector in the
709 ID. It is comprised of straw tubes filled with diluted Xenon gas, some of which ionizes
710 as charged particles pass through. The outer shell of each straw is held at a negative
711 potential while an anode wire running down the center of the tube is held at ground. As
712 some of the gas ionizes during the charged particle passage, an avalanche of ionization
713 electrons form on the wire, amplifying the signal an of order 10^4

714 The TRT provides an average of 36 track position measurements, making it
715 responsible for the large majority of track hits. Between the barrel and the end-caps,
716 as described in Figure 3.3(a), the TRT can track charged particles through the region
717 $|\eta| < 2.0$. All straw tubes in the TRT are 4 mm in diameter but vary in length between
718 the barrels and the end-caps. In the barrel, the straw tubes are 144 cm (37cm) long
719 and positioned parallel to the beam axis; in the end-caps, the tubes are 37 cm long and
720 arranged transverse to the beam axis in the radial direction. There are approximately
721 351,000 readout channels. Say something about how the TRT also helps identify elec-
722 trons over pions. Talk to Mike about the low-energy electron case and why particle ID
723 breaks depreciates.

724 **3.2.2 Calorimeters**

725 Just outside of the ID and solenoid magnet is the ATLAS calorimeter system.
726 The electromagnetic and hadronic calorimeters, extending to $|\eta| < 4.9$, measure the
727 energy of electromagnetic and hadronic objects as it dissipates inside the calorimeter
728 material. These calorimeters are samplers, meaning they only directly measure a frac-
729 tion of the absorbed energy, and from this, infer the shape and strength of the full
730 shower.

731 The eCal measures the energy of electrons and photons by inducing electro-
732 magnetic showering inside the eCal layers through continuous photon conversions and
733 Bremsstrahlung, spreading out among calorimeter cells until all the energy of the inci-
734 dent particle has been absorbed. The eCal is composed of electrodes submerged in liquid

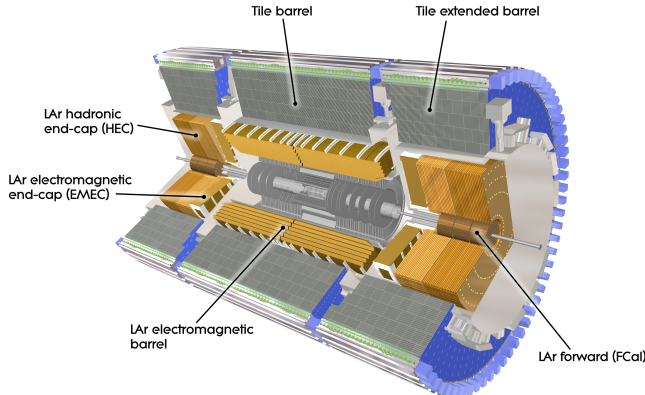


Figure 3.4: Picture of the ALTAS Calorimeters

735 argon (LAr) that induce the electromagnetic shower, layered in an accordion shape with
 736 lead absorber plates in between. It is divided into a central barrel with $|\eta| < 1.475$
 737 and two end-caps enclosing each side of the barrel. The end-cap regions have an inner
 738 wheel corresponding to $1.375 < |\eta| < 2.5$, and an outer wheel for $2.5 < |\eta| < 3.2$.

739 The eCal is split into three layers. The first layer is the most finely segmented in
 740 η to aid the discrimination between true photons and neutral pions that have decayed
 741 to a pair of pions. Both objects are trackless in flight and undetectable until they
 742 interact with the eCAL. Two closely-spaced photons from a boosted neutral pion decay
 743 are difficult to resolve as separate photons without the extremely fine grain of this first
 744 layer. The fine grain also helps improve the resolution of the shower position, shape
 745 and direction. The second layer is more granular and is also the thickest layer where
 746 the majority of the electromagnetic showering occurs, and the third and most granular
 747 layer samples from the tail of the shower. The eCAL is preceded by a pre-sampler at

748 $|\eta| < 1.8$ to correct for upstream energy losses.

749 When hadrons pass through the eCal, they deposit only a small amount of
750 energy as they travel to the hCal, where they will deposit the rest. The barrel of the
751 hCal spans the region $|\eta| < 1.7$ and sits just outside the EM calorimeter, extending
752 radially from 2.28 m to 4.25 m. Shown in Fig 3.4, it is made of iron-scintillator tile and
753 steel absorbers and separated into three sections, the central barrel and two extended
754 barrels. The LAr hadronic end-caps cover the η range $1.7 < |\eta| < 3.2$. Forward
755 LAr detectors measure both electromagnetic and hadronic showers and extend out to
756 $\eta < 4.9$.

757 3.2.3 Muon System

758 The muon spectrometer, a tracking detector dedicated entirely to tracking
759 muons, is the outer most sub-detector in ATLAS. It is designed to track muons in the
760 pseudorapidity region $|\eta| < 2.7$ with a central barrel covering $|\eta| < 1.05$ and two
761 end-caps at $1.05 < |\eta| < 2.7$. A network of three large super-conducting toroidal
762 magnets, each with eight coils, supplies a magnetic to the muon spectrometer with am
763 integral bending power in the barrel of around 2.5 Tm and up to 6Tm in the end caps.
764 Resistive plate chambers in the central region $|\eta| < 1.05$ and end gap chambers in
765 the forward-backward region $1.05 < |\eta| < 2.7$ impart triggering capabilities to the
766 MS as well as position measurements in η and ϕ with a spacial resolution of 5-10mm.
767 Monitored drift tube chambers provide precision tracking out to $|\eta| < 2.7$ where each
768 chamber provides 6-8 hits in η along the muon flight path.

769 **3.2.4 Trigger System**

770 Originally a three-level trigger system in Run-1, the trigger was restructured
771 into a two-level system with only a hardware level-1 (L1) trigger and a software-based
772 high-level (HL) trigger. Each trigger level makes decisions about which events to store
773 and which events to throw away forever. The L1 trigger searches for electrons, muons,
774 photons, jets, hadronically decaying τ -leptons, and missing transverse momentum. In
775 each event, the L1 trigger defines Regions-of-Interest (ROIs), which are detector regions
776 where interesting activity is identified, then stores the geographical (η, ϕ) coordinates,
777 the basic characteristics of the detector response in that region, and the set of criteria
778 that triggered the L1. This information is subsequently passed to the HL trigger to
779 perform a more refined event selection.

780 Next paragraph go into rates and amounts of data..

Part II

781

Method

782

783 **Chapter 4**

784 **Data Collection and Simulated Events**

785 The chapter will describe the nature of the datasets and events selected from
786 the datasets for analysis. LHC data is subjected to an analysis of events in the search
787 for compressed electroweak SUSY. Monte Carlo simulated events generated with a Hig-
788 gsino simplified model were studied to for a kinematic and topological understanding
789 of compressed electroweak signals of this type and inform our search region targeting
790 LHC data. Monte Carlo event generation is also used for Standard Model background
791 modeling in the optimized signal region. All LHC data and simulated events are re-
792 quired to pass event triggers based a E_T^{miss} threshold. In ATLAS data, these triggers
793 are hardware and software based as described in Chapter 3. In simulation, the triggers
794 are emulated at reconstruction level with ATLAS reconstruction software I know this
795 isn't right, but figure out what is Maybe mention the derivation and the framework?

Data Period	Lowest Unprescaled E_T^{miss} Trigger
2015	
All	HLT_xe70_mht_L1E50
2016	
A1-D3	HLT_xe90_mht_L1E50
D4-L11	HLT_xe110_mht_L1E50

Table 4.1: Evolution of lowest unprescaled E_T^{miss} trigger from the start of 2015 to the end of 2016. **add run numbers and integrated lumi for each trigger**

796 4.1 Triggers

797 The MET trigger threshold varies by data taking period, where the lowest
 798 unprescaled inclusive MET trigger is used. (Make table and refer to it)

799 4.1.1 MET Triggers

800 Inclusive met trigger efficiencies

801 4.1.2 Combined Trigger Studies

802 Near the end of period I, starting at run 308084, two new triggers went on the
 803 ATLAS trigger menu.

804 • HLT_mu4_j125_xe90_mht (seeded from L1_MU4_J50_XE40),

805 • HLT_2mu4_j85_xe50_mht (seeded from L1_2MU4_J40_XE20).

806 Lepton plus jet plus met trigger efficiencies.. **Talk about the development and study
 807 of the new triggers implemented n data starting at run 308084, corresponding to an
 808 integrated luminosity of 8.8 fb^{-1} .

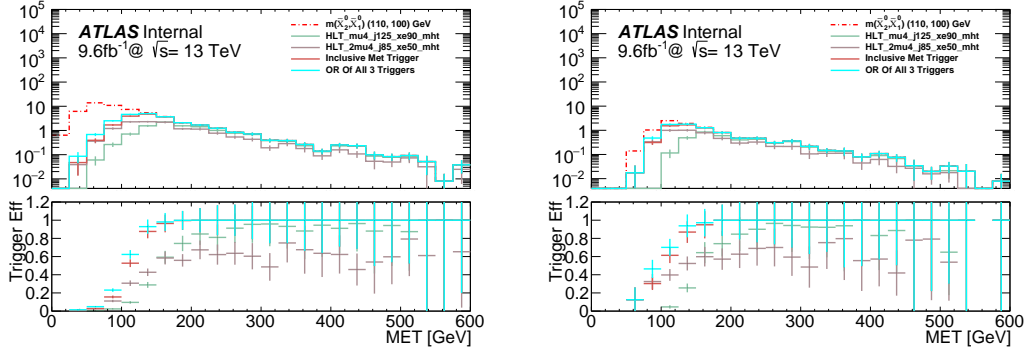


Figure 4.1: Trigger Efficiency as a function of MET after event preselection (left) and in a signal region similar to the analysis signal region (right)

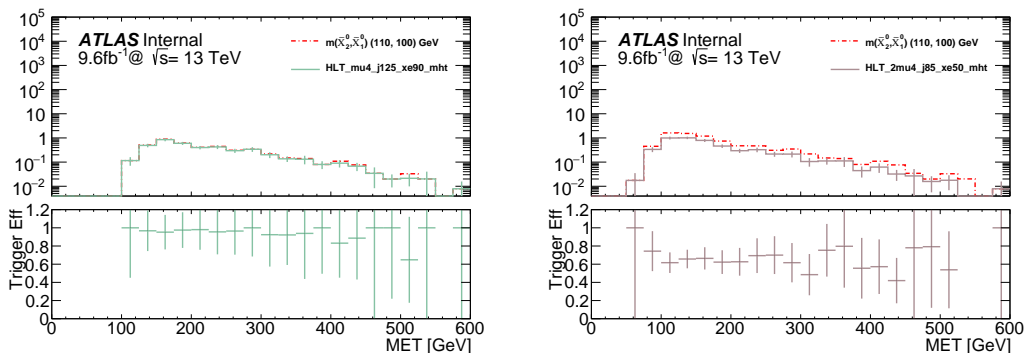


Figure 4.2: Trigger efficiency as a function of MET for the combined single muon trigger (left) and the combined dimuon trigger (right)

809 **4.2 Data**

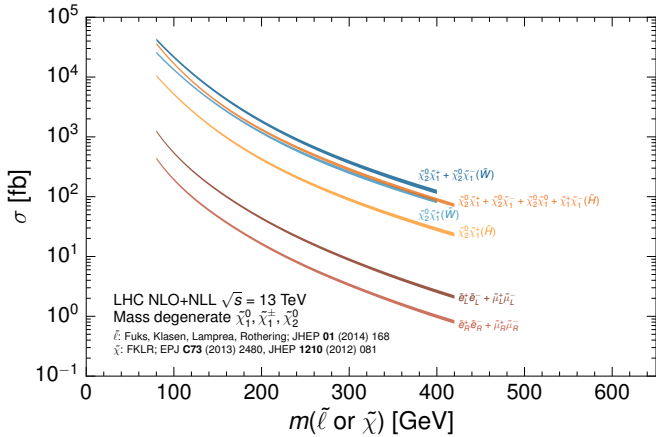
810 In 2015 and 2016, ATLAS recorded a combined 36.1 fb^{-1} total integrated
811 luminosity of LHC pp collision data at $\sqrt{13} \text{ TeV}$ that passed data quality cuts (Can
812 you describe what these are?), empowering numerous new physics searches that were
813 not possible in Run-1. Maybe discern Run-1 and Run-2 at the LHC so this has context?
814 Over 90% of Run-2 data came from 2016. Peak instantaneous luminosity progressed
815 from $5 \times 10^{33} \text{ cm}^{-2} \text{ s}^{-1}$ in 2015, to $13.8 \times 10^{33} \text{ cm}^{-2} \text{ s}^{-1}$ in 2016. How did μ evolve?
816 The number of interactions per event averaged (μ) was 13.5 in 2015 and 25 in 2016,
817 with a peak μ just over 40 near the end of 2016.

818 **4.3 Simulation**

819 ATLAS generated fully simulated Monte Carlo samples that behave like the
820 raw data in the detector. Monte Carlo samples used in this analysis were part of the
821 mc15 production campaign.

822 **4.3.1 Signal samples**

823 Data simulated with Monte Carlo based event generation techniques by the
824 ATLAS simulation infrastructure is used in the analysis for background and signal
825 modeling. Refer to the cross-sections for Higgsino and Slepton processes in Fig. ??

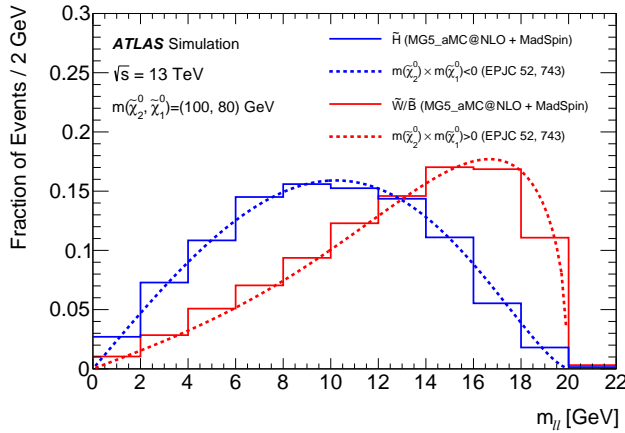


826 **4.3.1.1 Higgsino LSP Samples**

827 Higgsino simplified model samples include four processes: $\tilde{\chi}_2^0 \chi_1^+$, $\tilde{\chi}_2^0 \chi_1^-$, $\tilde{\chi}_2^0 \chi_1^0$,
828 and $\tilde{\chi}_1^+ \chi_1^-$.

- 829 • Explain the mass grid: The $\tilde{\chi}_1^\pm$ masses were fixed to (), while the $\tilde{\chi}_2^0$ and χ_1^0 masses
830 varied between such and such.
- 831 • Talk about the cross-sections of these processes
- 832 • Talk about how the signal is produced from Z^* decays and so the $\tilde{\chi}_1^+ \chi_1^-$ samples
833 don't really play a role in the optimization. The cross-sections are too low and
834 the lepton pairs come from two W -boson decays.
- 835 • Explain that radiative corrections give rise to mass-splittings of pure Higgsino
836 states of order MeV, and some level of wino or bino mixing is needed for larger
837 mass splittings. The models used to generate the signal samples use cross-sections
838 according to electroweak mixing matrices that assume purely Higgsino states for
839 all mass combinations of $\tilde{\chi}_2^0, \chi_1^0, \tilde{\chi}_1^+$, and χ_1^- .

- Branching ratios for $\tilde{\chi}_2^0 \rightarrow Z^* \tilde{\chi}_1^0$ and $\tilde{\chi}_1^\pm \rightarrow W^* \tilde{\chi}_1^0$ are fixed at 100%
- $Z^* \rightarrow \ell^+ \ell^-$ modeled with SUSY-HIT v1.5b, which correctly treats the finite b-hadron and τ -lepton masses.
- The branching ratio $Z^* \rightarrow \ell^+ \ell^-$ depends on the invariant mass of the Z^* , which is driven by the mass-splitting between $\tilde{\chi}_2^0$ and $\tilde{\chi}_1^0$. For example, the $Z^* \rightarrow \ell^+ \ell^-$ branching ratio for a 60 GeV mass-splitting is lower than for a mass-splitting of 2 GeV by 46% in $Z^* \rightarrow e^+ e^-$ and by 40% for $Z^* \rightarrow \mu^+ \mu^-$. This happens as the Z^* mass falls below the threshold needed to produce a pair of heavy quarks or τ leptons.
- Branching ratio for $W^* \rightarrow \bar{\nu}_\ell \ell$ also increases as the mass-splitting becomes sufficiently low to suppress decay widths to heavy quarks and *tau* leptons. (11% for large Δm changes to 20% for a Δm of 3 GeV.
- Events are generated at leading order with up to two extra partons in the matrix element using MG5_aMC@NLO v2.4.2 event generator and the NNPDF23LO PDF set.
- Electroweakinos decayed using MadSpin with a two-lepton events filter. This means only events were stored in the signal samples if there were at least two final state leptons, even if one or more of the leptons came from a leptonic τ decay.
- Resulting events interfaced with Pythia v8.186 using the A14 set of tuned parameters to model the parton shower, hadronization, and underlying event.



- 860 • ME-CS matching done with CKKWL-scheme, with the merging scale set to 15
 861 GeV. OH BOY, I have to explain all this in plain english!
- 862 • Add wino rescaling here? It does use the same samples but the cross-section is
 863 rescaled.
- 864 • Must talk about how the relative sign of the χ_1 and χ_2 mass parameters affects
 865 the model.

866 4.3.1.2 Compressed Slepton Samples

867 Slepton simplified models exploit the direct pair productions of the selectron
 868 $\tilde{e}_{L,R}$ and smuon $\tilde{\mu}_{L,R}$, where the L and R subscripts denote the left and right chirality
 869 of the partner electron or muon. The fur sleptons are assumed to be mass degenerate I
 870 know I have a reference for this. Sleptons decay to their Standard Model lepton partner
 871 a χ_1^0 100% of the time. Events were generated at tree level with MG5_aMC@NLO v2.2.3
 872 with the NNPDF23LO PDF set with up to two additional partons in the mixing matrix.

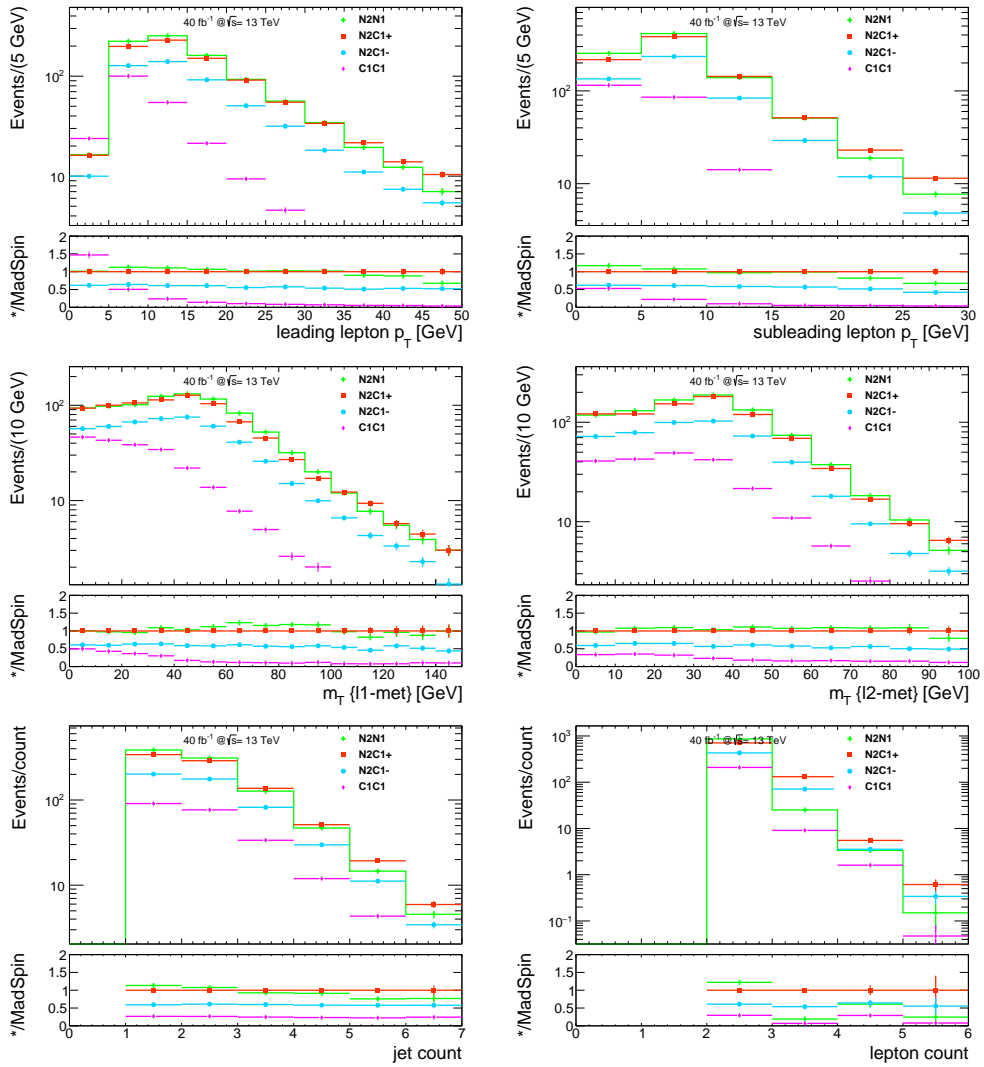


Figure 4.3: Kinematic distributions of signal samples

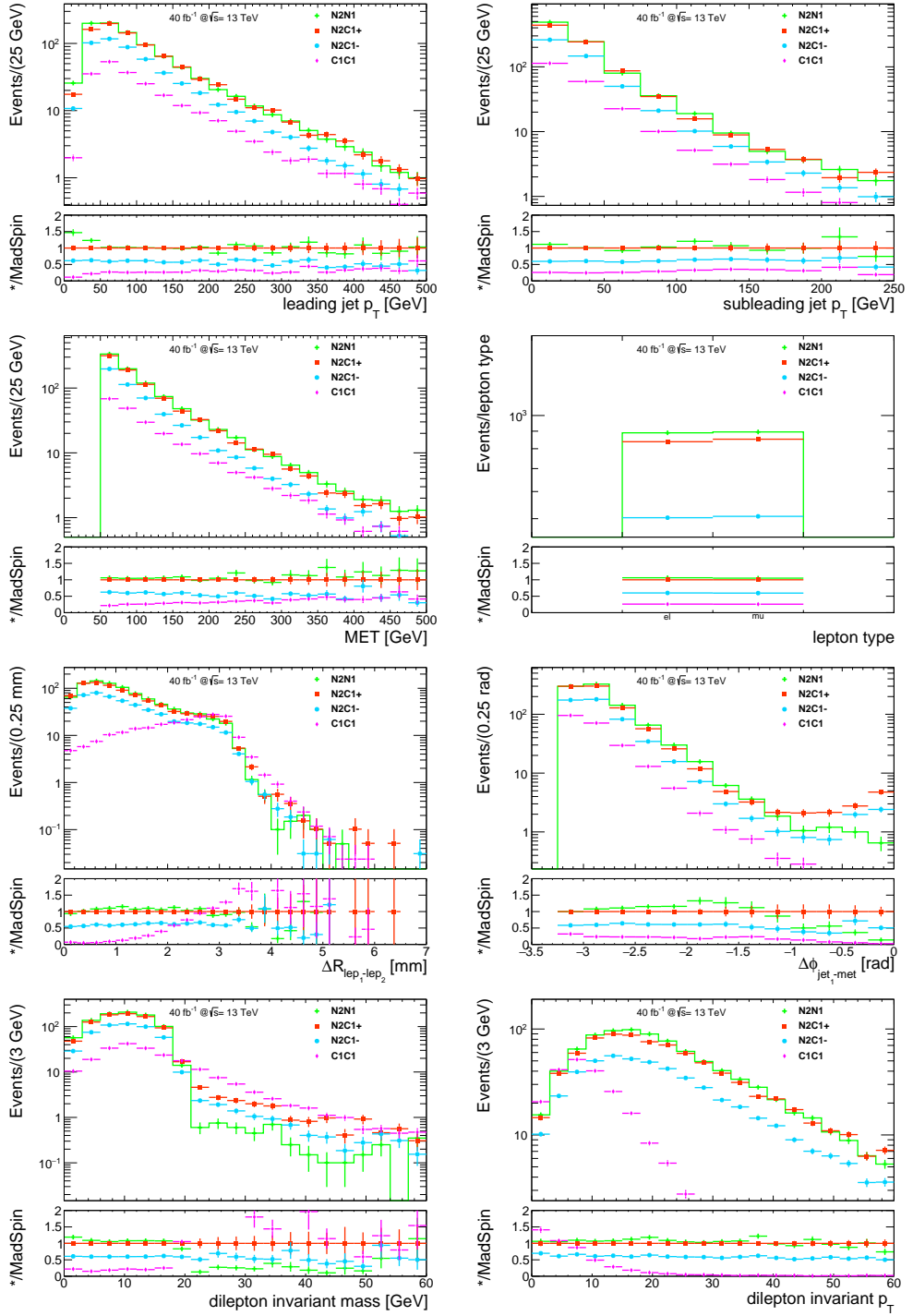


Figure 4.4: Kinematic distributions of signal samples

873 The MadGraph generation was interfaced with PYTHIA v8.186. ME-PS ([what does](#)
874 [this mean?](#) matching done with the CKKW-L prescription. Merging scale was set to
875 one quarter the slepton mass.

876 **4.3.2 Background Simulation**

877 Standard Model background processes were generated with multiple generators
878 [can you give a reason for this.](#) $Z^{(*)}/\gamma^*$ + jets, diboson, and triboson samples were made
879 using the SHERPA version 2.1.1, 2.2.1, and 2.2.2. Matrix elements were calculated for
880 up to two additional partons at NLO and four additional partons and LO, depending
881 on the process [Say specifically which for which processes.](#) This is done with COMIX
882 and OpenLoops [I have never heard of either of these,](#) and merged with the SHERPA
883 parton shower according to the ME-PS NLO prescription. The $Z^{(*)}/\gamma^*$ + jets samples
884 exploit invariant masses down to 0.5 GeV for $Z^{(*)}/\gamma^* \rightarrow e^+e^-/\mu^+\mu^-$, and down to 3.8
885 GeV for $Z^{(*)}/\gamma^* \rightarrow \tau^+\tau^-$. Dilepton invariant mass in diboson samples covers down to
886 0.5 GeV. Singletop and $t\bar{t}$ samples generated at NLO in the matrix element calculations
887 with POWHEG-BOX v1 and v2 interfaced with PYTHIA 6.428 with the PERUGIA
888 2012 tune. Higgs+ V , $t + V$, $t\bar{t} + V/h/\gamma^*$ and $t\bar{t} +$ diboson production simulated with
889 POWHEG-BOX v2 interfaced with PYTHIA 6.428 and 8.184 and the ATLAS A14
890 tune. These are all generated with NLO matrix elements, except the $t + Z$, $t\bar{t} + WW$,
891 three-top and four-top samples, which were calculated to LO. [make table](#)

892 Introduce the extensions of the background samples, then possibly show plots
893 [in the sections they correspond to](#)

- 894 ● Detector simulation done with GEANT4. GEANT4 models the ATLAS detector
895 geometry, material interactions, and magnetic field potentials.
- 896 ● Pileup is modeled how is it modeled
- 897 ● Monte Carlo processed by sub-detector specific digitization algorithms, which
898 translate the particle signatures in the detector into raw byte-stream data of the
899 form that comes from the ATLAS detector. Finally, fully simulated RDOs are
900 reconstructed with release ?? of the ATLAS Athena reconstruction software, just
901 like when processing real data.
- 902 ● Do I want to make a schematic that illustrates the process of producing ATLAS
903 MC simulation?

904 **4.3.2.1 V+Jets**

905 Model of leptonically decaying W or Z boson done with SHERPA with NNPDF30NNLO
906 PDF set. The matrix element is calculated with up to four additional partons in the
907 shower. Merging the parton shower is done with the ME+PS NLO prescription. The
908 samples are sliced in maxHTPTV and quark flavor content I don't know what this
909 means. Kinematics of the sample are as follows. The dilepton invariant mass of the
910 on shell Z+jets samples is required to be above 50 GeV, and the Z^* +jets samples are
911 restricted to dilepton invariant mass between 10 GeV and 40 GeV with the leading
912 and subleading leptons having p_T above 5 GeV. The Z+jets samples were extended
913 down to very off-shell Z production for dilepton invariant mass below 10 GeV, but no

914 less than twice the mass of the leading lepton in the system. The samples are inclusive
915 in quark flavor and only available for $\text{maxHTPTV} > 280$ GeV slice.

916 **4.3.2.2 Multiboson**

917 Multiboson refers to two and three vector boson production modes. SHERPA
918 is used diboson and fully leptonic triboson processes. The NNPDF30NNLO PDF set
919 was used for most samples, but for the few were this was not an option CT10 PDF set
920 was used. The initial samples are made of events with same flavor and oppositely signed
921 leptons, where the invariant mass of the dilepton system is above 4 GeV and the leading
922 and subleading leptons have masses above 5 GeV. The samples were later extended
923 to lower lepton masses, where the leading two leptons have masses above 2 GeV and
924 their invariant mass must be below 10 GeV and can be as low as twice the mass of
925 the leading lepton. W and Z production in association with an energetic photon is also
926 modeled with SHERPA and in the same kinematic space, but samples were generated
927 exclusively with the CT10 PDF set.

928 **4.3.2.3 Top Quark**

929 Single top production (t- and s- channel), tW , and $t\bar{t}$ events were generated
930 with POWHEG and interfaced with PYTHIA 6 for parton showering. The have var-
931 ious lepton filters..., for the tZ process, which is filtered to have at least one lepton,
932 MADGRAPH5 calculated the matrix elements while PYTHIA 6 still handles the parton
933 showering. Rare events with three and four top quarks or $t\bar{t}$ in association with a Z ,

934 W , or WW bosons have matrix elements calculated with MADGRAPH5 and showered
935 with PYTHIA8 according to PDF set NNPDF30NNLO.

936 **4.3.2.4 Higgs**

937 Single Higgs production via gluon-gluon fusion (ggF) and vector boson fusion
938 (VBF) processes decaying via fully leptonic WW or directly into two leptons are modeled
939 using POWHEG, interfaced with PYTHIA 8 for parton showering and hadronization using
940 the NLOCTEQ6L1 PDF set. Processes involving a single Higgs in association with W
941 or Z boson are modeled just using PYTHIA 8 and the NNPDF23LO PDF set.

942 **4.4 Derivation**

943 Describe details of the SUSY16 derivation used to select events from data

944 **Chapter 5**

945 **Physics Object Reconstruction and**

946 **Identification**

947 Refer to what we learned about the ATLAS detector and what really is read out
948 is detector response through readout electrons and stored in some form (*What form is*
949 *raw detector output stored?*). To actually do physics analysis with ATLAS data, physics
950 objects and their observable characteristics must first be reconstructed and identified
951 from that data that represents their interactions with the detector volume. The term
952 reconstruction describes the process of interpreting the signal output from the detec-
953 tor and transferring the information to measurements associated with actual physics
954 objects. ATLAS was specifically designed to optimize particle energy and momentum
955 measurements as well as particle identification. There are teams in the ATLAS Col-
956 laboration called Combined Performance groups with the concurrent goal of optimizing
957 and assessing the performance of the reconstruction and identification algorithms for

958 different types of particles. The Combined Performance groups then make recommen-
959 dations to the analysis groups for which object definitions to use and the efficiencies to
960 expect.

961 Reliable tracking, clustering, and vertexing are the building blocks for efficient
962 object reconstruction. The assembly of tracks, clusters and vertices will be described
963 first, an explanation of the identification are reconstruction of directly observable and
964 indirectly observable in the ATLAS detector: electrons, muons, jets, photons, missing
965 energy and momentum measurements. Lastly, I will describe the techniques of overlap
966 removal, isolation correction of closely-spaced lepton, and lepton truth matching in
967 Monte Carlo.

968 5.1 The Building Blocks

969 Track reconstruction provided the important information needed for primary
970 and secondary vertex reconstruction, charged particle reconstruction, jet flavor tagging,
971 and photon conversions; therefore, track reconstruction algorithms must be swift, con-
972 cise, perform with high efficiency, low fake rates and with proper resolution on tracking
973 parameters. In 2015, at the start of Run-2, the LHC extended the center of mass energy
974 in proton-proton collisions to 13 TeV, and over the duration of Run-2, ramped-up the
975 instantaneous luminosity pushing the average interactions per bunch crossing (μ) to
976 above 40 by the end of Run-2. This extension of center of mass energy and instanta-
977 neous luminosity enhances the outlook of discovery while simultaneously slowing down

978 track reconstruction and degrading reconstruction efficiency. Events with jet showers
979 in the TeV range and τ leptons and B-hadrons that traverse multiple ID layers before
980 decaying, occur at rates high enough to be considered in optimizing track and cluster
981 reconstruction in Run 2. In the core of boosted hadronic jets and τ lepton decays, par-
982 ticles in flight do not spread out much as they traverse the inner tracking layers, making
983 separate energy deposits in the discrete sensors hard to resolve and near-by tracks hard
984 to distinguish from each other. If tracking efficiency is low in events with high track
985 density, mismeasurements are expected in identifying long-lived b-hadron and hadron
986 τ decays and in calibrating the energy and mass of jets. These mismeasurements will
987 also cause induced \vec{E}_{miss}^T , which is an important quantity for this search and many
988 other beyond standard model searches.* Another challenge to track reconstruction dur-
989 ing Run-2 is the CPU time increase as μ , the average interactions per bunch crossing,
990 increases. As μ goes up, the pattern recognition algorithms suffer a non-linear increase
991 of the combinatorics in track-hit association.

992 Event by event charged track reconstruction in the pixel and SCT detectors
993 starts with clustering groups of pixels and strips in the same sensor that respond to
994 an energy deposition above a set threshold and share a common edge or corner. These
995 clusters form three-dimensional space-points that measure where a particle intersects
996 the active material in the ID. In the pixel detector, each particle corresponds to one
997 space-point, while in the SCT, clusters must be combined from both sides of a strip
998 layer to obtain a three-dimensional position measurement. Charge in the pixel sensors
999 is often collected in more than one adjoining pixels *Maybe connect here hit resolution*

1000 to cluster size and use plots from the IBL paper.. remembering to explain how impact
1001 parameter resolution is driven by the resolution of the hit closest to the primary vertex

1002 Steps in track reconstruction:

1003 • Preprocessing

1004 1. Pixel and SCT clustering

1005 2. drift-circle creation in TRT

1006 3. Clusters transformed in 3D space-points

1007 • Track Finding

1008 1. Triplets of pixel and SCT space-point combined into seeds

1009 2. Seeds with an additional compatible cluster are sent to a Kalman filter (??)

1010 • Ambiguity Solving

1011 1. Tracks fit using a global chi-squared function

1012 2. Tracks are scored based upon fit quality, number of shared clusters, and holes

1013 3. Tracks below quality threshold are removed

1014 • TRT Extension

1015 1. Tracks passing the ambiguity solver and extended into the TRT and refit

1016 2. Tracks with no matching TRT extension are also kept

1017 What is the primary vertex?. Primary vertices are identified using inner detector tracks

1018 that satisfy a set of requirements. For a track to be considered in the construction of a

Tracks	Clusters	Vertices
stuff	stuff	Stuff
stuff	stuff	more stuff

Table 5.1: Summary of blah blah

1019 primary vertex, it must have $p_T > 400 \text{ GeV}$, $|\eta| < 2.5$, between 9 ($|\eta| \leq 1.65$) and 11
 1020 ($|\eta| > 1.65$) silicon hits, at least 1 hit in the IBL or B-Layer, a maximum of one shared
 1021 pixel hit or two shared SCT hits, no holes in the pixel layers, and no more than one
 1022 hole in the SCT layers. Any primary vertex must have at least two associated tracks
 1023 for reconstruction. The track criteria is summarized in Table 5.1.

1024 5.2 Particle Identification and Reconstruction

1025 Reconstructed and identified particles in ATLAS are leptons(e, μ, τ), photons,
 1026 jets, which can further be identified as b-jets, and missing transverse momentum \vec{E}_{miss}^T .
 1027 This analysis does not use τ reconstruction [Talk with Mike about this...](#). There are
 1028 two categories; *baseline* objects, which is the most inclusive definition of an object
 1029 and are typically used for preliminary event selection and background modeling, and
 1030 *signal* objects, a more exclusive object definition that is a subset of *baseline* and used
 1031 exclusively when defining signal events.

1032 Baseline electrons are triggered from energy deposits in the electromagnetic
 1033 calorimeter and reconstructed with algorithms using the electromagnetic calorimeter
 1034 clusters that are matched to inner detector tracks. Baseline electrons must pass p_T
 1035 threshold of 4.5 GeV and be in central detector region $|\eta| < 2.47$. A longitudinal

1036 impact parameter requirement of $|z_0 \sin\theta| < 0.5 \text{ mm}$ is also applied. *Have I defined*
1037 *impact parameter yet?* Electrons are distinguished from other particles using identifica-
1038 tion criteria that rely on the shower shape in the electromagnetic calorimeter, tracking
1039 quantities, and the health of the track to EM calorimeter cluster matching. Identifica-
1040 tion criteria varies from loose to tight and evolves with increasing strictness in criteria
1041 cuts that can be based either on independent requirements or on the single requirement
1042 set on the output of the likelihood function based on all the discriminating quantities
1043 listed above. This analysis uses likelihood based identification criteria only. *Explain*
1044 *more about identification criteria we use.* Baseline electrons are required to satisfy
1045 *VeryLooseLLH* identification while signal electrons must pass *Tight* identification plus
1046 *GradientLoose* isolation criteria. *Define the isolation criteria* Signal electrons also re-
1047 quire a transverse impact parameter $|d_0/\sigma(d_0)| < 5$. Furthermore, electrons with author
1048 16 are vetoed. *Explain what author 16 means*

1049 Muon information primarily comes from charged tracks in the inner detector
1050 and tracks in the muon spectrometer. The calorimeters essentially don't contribute any
1051 useful information about the muons that pass through since energy measurements in the
1052 Ecal or Hcal rely on a particle's complete energy deposition in the calorimeter layers.
1053 Baseline muons are reconstructed with algorithms that combine tracks from the inner
1054 detector and muon spectrometer to form muon candidates. They must pass p_T threshold
1055 of 4 GeV and be in fiducial region $|\eta| < 2.5$. Baseline muons are also expected to
1056 satisfy *Medium* identification standards (DEFINE THIS) and have a transverse impact
1057 parameter $|z_0 \sin\theta| < 0.5 \text{ mm}$. Signal muons must also satisfy *FixedCutTightTrackOnly*

1058 isolation criteria and a transverse impact parameter requirement of $|d_0/\sigma(d_0)| < 3$.

1059 Baseline jets are reconstructed using locally-calibrated three-dimensional topo-
1060 logical clusters built from calorimeter cells. Topo-clustering starts by determining
1061 calorimeter cells with energy significance 4σ about the quadrature sum of electronic
1062 and pileup noise. Neighboring jets with energy significance 2σ about noise are itera-
1063 tively added, forming seed cluster, then a ring of direct neighbor cells are added to the
1064 final topo-clusters. Jets are constructed using anti- K_t algorithm with radius parameter
1065 $R = 0.4$ in this case. Baseline jets must pass p_T threshold of 20 GeV and be in fiducial
1066 region $|\eta| < 4.5$. Also, jets within $|\eta| < 2.5$ originating from b-hadrons are identified
1067 with the $MV2c10$ algorithm (define this!) with an 85% working point. Signal jets are
1068 further restricted to fiducial region $|\eta| < 2.8$.

1069 TODO: Add paragraph about photon ID

1070 Well calibrated energy and momentum measurements of the directly observable
1071 objects is important for construction of the particles that traverse the detector without
1072 interacting. These "missing" particles carry away energy and momentum which is re-
1073 covered with energy and momentum conservation in the plane transverse to the beam
1074 pipe. The vector quantity called "missing transverse momentum" (\vec{E}_{miss}^T) and the
1075 scalar magnitude representing the "missing transverse energy" (E_{miss}^T) Missing Trans-
1076 verse momentum (MET) is the negative vector sum of the transverse momentum of all
1077 the identified physics objects (electrons, muons, jets, photons) plus an additional soft
1078 term. The soft term is constructed from all the tracks not associated with any physics
1079 object, but are associated with the primary vertex. Therefore, the met is adjusted for

Selection Criteria	Electrons	Muons	Jets
Baseline			
Reco Algorithm	<i>author 16 veto</i>		
Kinematic	$p_T > 4.5 \text{ GeV}$, $ \eta < 2.47$	$p_T > 4 \text{ GeV}$, $ \eta < 2.5$	$p_T > 20 \text{ GeV}$, $ \eta < 4.5$
Impact Parameter	$ z_0 \sin\theta < 0.5 \text{ mm}$ — <i>VeryLooseLLH</i>	$ z_0 \sin\theta < 0.5 \text{ mm}$ — <i>Medium</i>	
Identification			
Isolation	—	—	
Clustering			Anti- K_t R = 0.4 EMTopo
Jet Vertex Tagging			—
b -tagging			—
Signal			
Reco Algorithm	<i>author 16 veto</i>		
Kinematic	$p_T > 4.5 \text{ GeV}$, $ \eta < 2.47$	$p_T > 4 \text{ GeV}$, $ \eta < 2.5$	$p_T > 30 \text{ GeV}$, $ \eta < 2.8$
Impact Parameter	$ z_0 \sin\theta < 0.5 \text{ mm}$, $ d_0/\sigma(d_0) < 5$ <i>Tight</i>	$ z_0 \sin\theta < 0.5 \text{ mm}$, $ d_0/\sigma(d_0) < 3$ <i>Medium</i>	
Identification			
Isolation	<i>GradientLoose</i>	<i>FixedCutTightTrackOnly</i>	
Clustering			Anti- K_t R = 0.4 EMTopo
Jet Vertex Tagging			<i>JVT Medium</i>
b -tagging			$p_T > 20, \eta < 2.5$
			MV2c10 FixedCutBeff 85%

Table 5.2: Summary of object definitions

1080 the best possible calibration of the jets and other identified physics objects and still
1081 pileup independent in the soft term.

1082 5.3 Treatment of Reconstructed Objects

1083 Once objects are identified special algorithms must still be performed before
1084 these objects can confidently used for analysis. Here I describe the object removal, the
1085 isolation correction we performed on closely-spaced leptons, and the truth matching
1086 done with Monte Carlo samples.

1087 Overlap removal is performed to prevent double counting of physics objects.

1088 First, jet-electron overlap removal is performed. If $\Delta_{R(jet,electron)}$ is less than 0.2 and
1089 the the jet is not tagged as a b-jet, the jet is removed and the electron is kept. If the
1090 jet is identified as a b-jet, then the jet is kept and the electron object is removed since
1091 the electron is most likely from the semi-leptonic decay of a B-hadron. If $\Delta_{R(jet,electron)}$
1092 is less than 0.4, we remove the electron and keep the jet. Similarly, if the $\Delta_{R(jet,muon)}$
1093 is less than 0.4, we remove the muon and keep the jet unless the jet has less than three
1094 tracks; in which case, the muon will be kept and the jet is discarded. Lastly, we perform
1095 overlap removal on photons and other objects. It is common that electron and muon
1096 objects will also be included in the photon container since they pass the Ecal shower
1097 requirements, so typically, overlapping photons and leptons will result in the photon
1098 object being removed from the photon container. If $\Delta_{R(photon,electron)}$ is less than 0.4 we
1099 remove the photon and keep the electron. If $\Delta_{R(photon,muon)}$ is less than 0.4, we remove

1100 the photon and keep the muon. If $\Delta_{R(\text{photon},\text{jet})}$ is less than 0.4, we keep the photon
1101 and remove the jet. (TODO:Explain more about why the overlap removal is done in
1102 this way.

1103 Soft leptons in a boosted system can have small angular separation, especially
1104 is products of a low-mass Z^* decay. These closely-spaced leptons can lie within each
1105 others isolation cones, leading to a loss of efficiency for very small mass-splittings. *Refer
1106 to Figures 5.1 and 5.2 for additional motivation and explanation This loss is corrected
1107 for using a dedicated tool that checks baseline leptons that fail the isolation criteria
1108 for other nearby leptons that are within it's isolation cone. Tracks associated with
1109 the nearby lepton are removed from the track isolation sum. If the nearby lepton is
1110 an electron, the topocluster E_T is removed from the calorimeter isolation sum. The
1111 corrected isolation variables are then reanalyzed using the original isolation working
1112 point. Figure 5.3 shows the effect of this correction on low invariant mass dilepton pairs
1113 in both data and Monte Carlo samples.

1114 While detector effects that result in the misidentification of physics objects are
1115 not well modeled in simulation, misidentification still occurs during reconstruction. Re-
1116 ducible fake lepton backgrounds are estimated with a data-driven method and therefore
1117 are already accounted for. Background estimated done in Monte Carlo use only truth
1118 matched leptons to prevent overlap in the MC and data-driven estimates.

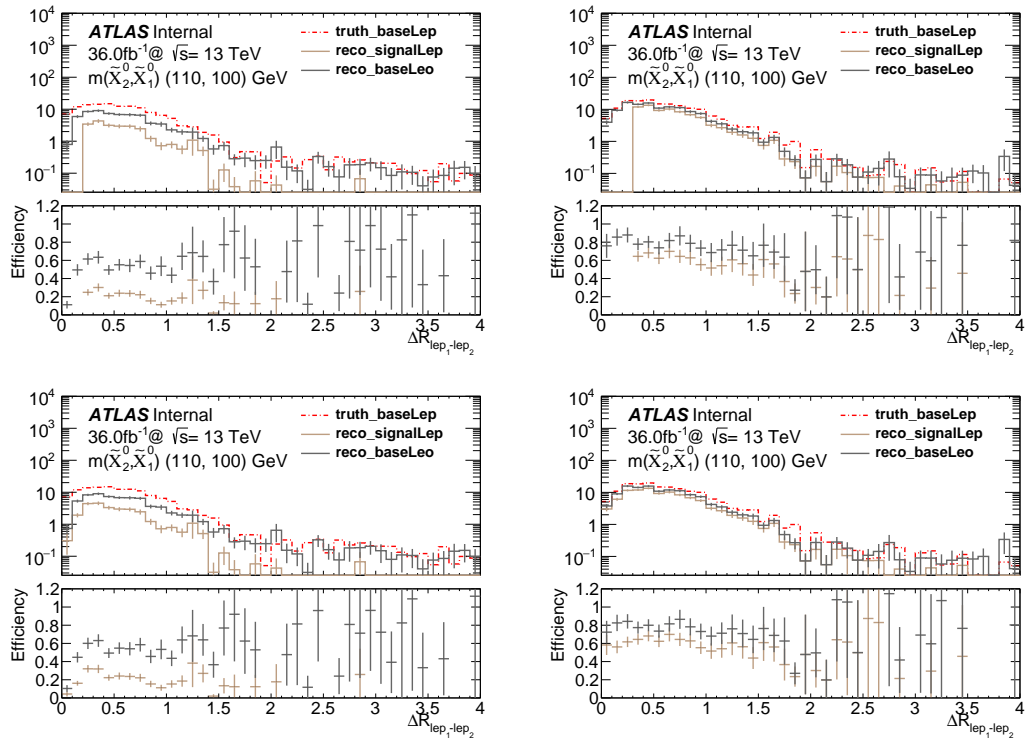


Figure 5.1: Dilepton ΔR distribution before LepIsoCorrection (top) and after LepIsoCorrection (bottom) for the ee -channel (left) and $\mu\mu$ -channel (right).

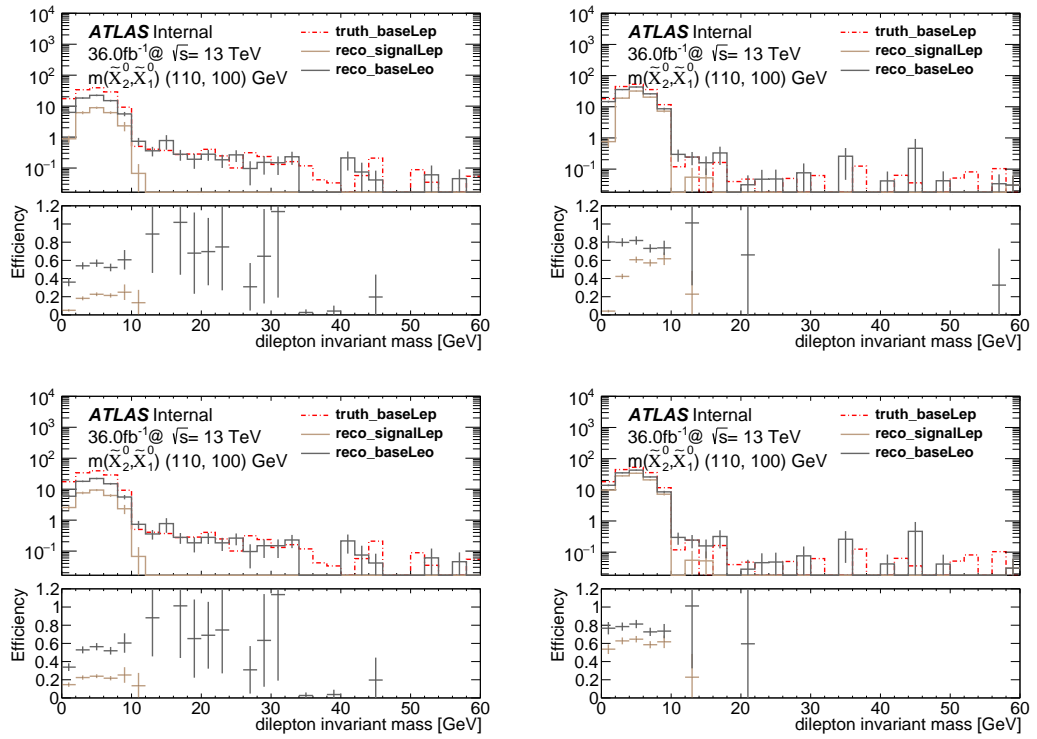


Figure 5.2: Dilepton invariant mass distribution before LepIsoCorrection (top) and after LepIsoCorrection (bottom) for the ee -channel (left) and $\mu\mu$ -channel (right).

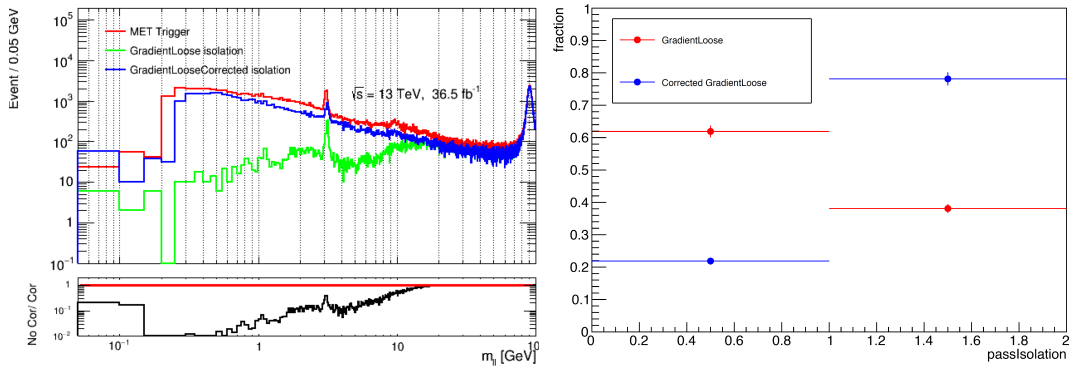


Figure 5.3: (left) Impact of the `NearbyLepIsoCorrection` tool on the efficiency of low-mass dilepton pairs in data. The data are shown in a region with $\Delta\phi(E_T^{\text{miss}}, p_t^{j1}) < 1.5$ to avoid the signal region. Events are triggered with the inclusive- E_T^{miss} trigger. The red trend shows events with two baseline leptons without applying any isolation; the green shows the impact of applying `GradientLoose` isolation; the blue shows the result of the `NearbyLepIsoCorrection` applied to the `GradientLoose` sample. (right) Impact of the correction on a Higgsino LSP signal sample with $\Delta m(\chi, \chi) = 3 \text{ GeV}$.

1119 **Chapter 6**

1120 **Signal Region Optimization**

1121 This analysis relies on external predictions of signal and background processes
1122 in the data to help interpret the observations. It is imperative to search for new physics
1123 where its presence is not excessively drowned out by SM backgrounds. To achieve this,
1124 a signal enriched region in phase space called a *signal region* (SR) is defined through a
1125 series of selection cuts on kinematic variables targeting a region in phase space where
1126 there is a significant excess in the signal events over the predicted background events.
1127 While signal regions are enriched in the process of interest, backgrounds are still present,
1128 and to estimate the background contamination in the SR, a semi-data-driven approach
1129 is employed. This requires defining new regions enriched with certain backgrounds, for
1130 instance top or $Z \rightarrow \tau\tau$, that are free of signal contamination. This type of region
1131 enriched with background events is called a *control region* (CR). The CRs used in this
1132 analysis are described in Chapter 7.2

1133 There are two separate signal regions for each the Higgsino and the slepton

1134 analyses. There are common cuts where the signal regions are being optimized in
1135 parallel, and then there are set of cuts that are specific to each analysis, and most
1136 importantly, they exploit a different kinematic signature of the system. Events in the
1137 signal regions are required to contain two signal leptons. The lepton with the highest
1138 p_T , the leading lepton, is required to have $p_T > 5$ GeV and the lepton with the next
1139 highest p_T , the subleading lepton, is required to have $p_T > 4.5$ GeV. Explain why
1140 this choice is made. Collinear leptons from photon conversions are filtered out with a
1141 restriction on the minimum $\Delta R_{\ell\ell}$ between the leptons of 0.05, and an invariant mass
1142 cut of $m_{\ell\ell} > 1$ GeV. Summarize the sections to come.

1143 6.1 Discriminating Variables

1144 Here I will define all the discriminating variables, and in the next section I will
1145 go into detail how they are applied to the signal regions and what benefits or limitations
1146 there are. There are discriminating variables that exploit the lepton information (Same
1147 flavor lepton pair with opposite charge, $\Delta R_{\ell\ell}$, $m_{\ell\ell}$), and there are those that exploit the
1148 topology of only the jets and the E_T^{miss} ($\Delta\phi_{j_1-\text{met}}$, $\min\Delta\phi_{\text{jets-met}}$, $p_T(j_i)$, Number of
1149 b -tagged jets $N_{b-\text{jets}}$), and there are those that exploit both ($m_{T2}^{m_X}, m_T^{\ell_1}$, $E_T^{\text{miss}}/H_T^{\text{leptons}}$,
1150 $m_{\tau\tau}$).

1151 Make clear summarizing the non-leptonic variables first. $|\Delta\phi(j_1, p_T^{\text{miss}})|$ mea-
1152 sures the angular separation between the leading jet and missing transverse momentum.
1153 Missing transverse momentum from jet mismeasurements tends to align the quantities

1154 and leads to small $\Delta\phi$. This variable should have a minimum requirement that reduces
 1155 this induced E_T^{miss} , which is mostly occurs in QCD and $Z+\text{jets}$ events. Similarly, the
 1156 $\min|\Delta\phi(\text{jets}, p_T^{\text{miss}})|$ is a variable that considers the minimum angular separation be-
 1157 tween E_T^{miss} and the nearest reconstructed jet. $p_T(j_1)$ is the momentum of the leading
 1158 jet in an event. Because of the soft leptons, the E_T^{miss} is correlated to this variable. If
 1159 the threshold on the $p_T(j_1)$ is too low, this will allow other subleading jet to contribute
 1160 to the measured hadronic recoil of the system. $N(b-\text{jets})$, number of b-tagged jets,
 1161 is a discriminating variable because the $t\bar{t}$ background is significantly enhanced in b-
 1162 tagged jets, while the Higgsino signal is not. Also, the slepton signal does not include
 1163 heavy flavor quarks in the decay chains. Therefore, rejecting jets tagged as coming from
 1164 b-quarks reduces the $t\bar{t}$ backgrounds.

1165 Now make clear I am going over leptonic variables. Same flavor lepton pair
 1166 with opposite charge requirement prefers the dominant leptonic decay mode of the
 1167 Higgsino via off-shell Z^* . Also, light flavor sleptons always decays to two oppositely
 1168 charges leptons of the same flavor. This selection in signal regions targets the decays of
 1169 this analysis and leaves the control and validation regions to exploit the different flavor
 1170 or same signed lepton pairs. The distance between the dilepton pair, $\Delta R_{\ell\ell}$ is defined
 1171 as:

$$\Delta R_{\ell\ell} = \sqrt{(\eta_{\ell_1} - \eta_{\ell_2})^2 + (\phi_{\ell_1} - \phi_{\ell_2})^2} \quad (6.1)$$

1172 The transverse mass of the leading lepton and the E_T^{miss} $m_T(p_T^{\ell_1})$ is defined as:

$$m_T(p_T^{\ell_1}, p_T^{\text{miss}}) = \sqrt{m_{\ell_1}^2 + 2(E_T^{\ell_1} E_T^{\text{miss}} - p_T^{\ell_1} p_T^{\text{miss}})} \quad (6.2)$$

1173 For electroweakino signals, the leading lepton and the p_T^{miss} are more likely to be closer
 1174 together than in background events. Maybe mention in optimization studies that the
 1175 $m_T(p_T^{\ell_1}$ can also reconstruct ($W \rightarrow \ell\nu$) processes, which leads to an $m_T(p_T^{\ell_1} < 70$ GeV
 1176 cut imposed. The dilepton mass $m_{\ell\ell}$ can both suppress backgrounds as well as ex-
 1177 ploit special features of Higgsino model. Continue on about the kinematic endpoint..
 1178 Similarly, slepton signals a kinematic endpoint defined by the 'transverse' mass $m_{T2}^{m_\chi}$,
 1179 which is a function of the measures momentum of the leading two leptons p_{ℓ_1}, p_{ℓ_2} , the
 1180 measured p_T , and the hypothesized invisible particle mass m_χ . explain how the $m_{T2}^{m_\chi}$ is
 1181 actually restricted in signal samples.. and more on all of this in section such and such.
 1182 The 'transverse' mass is defined as the extremization of q_T , the sum of immeasurable
 1183 missing transverse momentum vectors $p_T^{\chi,i}$ of each of the initially produced invisible
 1184 particles. The calculation of q_T is shown in Eq 6.3, and $m_{T2}^{m_\chi}$ is shown in Eq 6.4.

$$q_T = p_T^{\chi,1} + p_T^{\chi,2} \quad (6.3)$$

1185

$$m_{T2}^{m_\chi}(p_{\ell_1}, p_{\ell_2}, p_T^{miss}, m_\chi) = \min(\max[m_T(p_T^{\ell_1}, \chi), m_T(p_T^{\ell_2}, p_T^{miss} - q_T, \chi)]) \quad (6.4)$$

1186 m_T is described in Eq 6.2 except for... For the pair of semi-invisible particles in the
 1187 slepton signal is this the slepton pair that decay to leptons and neutralinos?, $m_{T2}^{m_\chi}$ is
 1188 always less than the parent slepton mass $m_{\tilde{\ell}}$ when the hypothesized m_χ mass is set to the
 1189 neutralino mass in the underlying process. This defines the lower kinematic endpoint
 1190 in $m_{T2}^{m_\chi}$ for slepton signals. Requiring $m_{T2}^{m_\chi} < m_{\tilde{\ell}}$, various mass scenarios can be probed
 1191 in the slepton-neutrino mass plane. Standard Model backgrounds not display this kind
 1192 of feature since the invisible particles are massless neutrinos, therefor there is not such

1193 enhancement in background when making this requirement. In fact, in the compressed
 1194 region of the slepton-neutrino mass plane, events populate a narrower region in m_{T2} ,
 1195 giving this variable more discriminating power. **Should expand on this, either here or**
 1196 **in next sections.**

1197 $E_T^{\text{miss}}/H_T^{\text{leptons}}$ A variable that discriminates between events with soft and hard lep-
 1198 tonic activity is ratio of E_T^{miss} over H_T^{leptons} , where H_T^{leptons} is defined as:

$$H_T^{\text{leptons}} = \sum p_T^{\ell_i} \quad (6.5)$$

1199 For given values of E_T^{miss} **Which values?**, Standard Model diboson and $t\bar{t}$ background
 1200 processes produce hard leptons, likewise diminishing the values of $E_T^{\text{miss}}/H_T^{\text{leptons}}$. In
 1201 compressed electroweakino and slepton events, the E_T^{miss} is mostly from the boost of
 1202 the hadronic recoil. The recoiling jet affects the heavier invisible particle much more
 1203 than it effects the lighter leptons; therefore, these signal events prefer larger values of
 1204 $E_T^{\text{miss}}/H_T^{\text{leptons}}$. **Motivate more completely in the next section.**

1205 Lastly, the di-tau invariant mass, $m_{\tau\tau}(p_{\ell_1}, p_{\ell_2}, \mathbf{p}_T^{\text{miss}})$ is used by this analysis
 1206 to veto the $Z \rightarrow \tau\tau$ background. The di-tau invariant mass is a function of the measure
 1207 lepton momenta, $p_{\ell_{1,2}}$ and the missing transverse momentum, $\mathbf{p}_T^{\text{miss}}$, as defined in Eq 6.6.

$$m_{\tau\tau}(p_{\ell_1}, p_{\ell_2}, \mathbf{p}_T^{\text{miss}}) = \begin{cases} \sqrt{m_{\tau\tau}^2} & m_{\tau\tau}^2 \geq 0, \\ -\sqrt{|m_{\tau\tau}^2|} & m_{\tau\tau}^2 < 0. \end{cases} \quad (6.6)$$

1208 The purpose of this variable is to reconstruct the di-tau invariant mass of the fully
 1209 leptonic $Z \rightarrow \tau\tau$ process from the measurable quantities in the event, the 4-momenta of

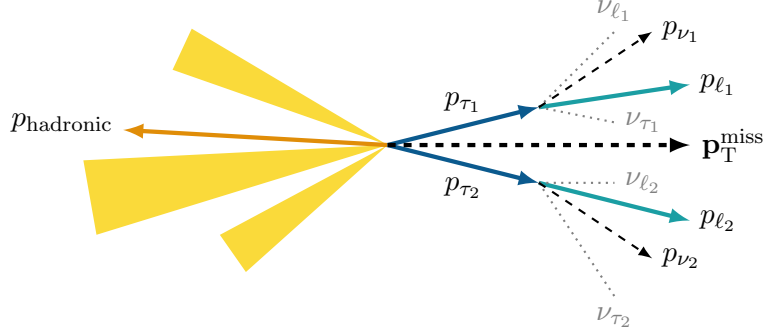


Figure 6.1: Schematic illustrating the fully leptonic ($Z \rightarrow \tau\tau$) + jets system motivating the construction of $m_{\tau\tau}$.

1210 the two leptons and the missing transverse momentum. In Eq 6.6, p_{ℓ_1} and p_{ℓ_2} are the
 1211 measured lepton 4-momenta, and \mathbf{p}_T^{miss} is the measured missing transverse momentum.
 1212 A ($Z \rightarrow \tau\tau$) + jets event within the signal region relies on the Z boson recoiling off
 1213 the jet activity, boosting the decaying di-tau system oppositely along the jet axis. This
 1214 kick from the jets causes the leptons and neutrinos to remain close to a single axis, so
 1215 the 4-momentum of the invisible neutrino system p_{ν_i} , for the i_{th} τ in the event, can be
 1216 well approximated by a simple rescaling of the lepton 4-momentum. **GEEZ there is so**
 1217 **much to explain here!**

1218 6.2 Optimization Studies

1219 Now that the discriminating variables have been introduced, this will discuss
 1220 the process of choosing the best signal region. **This section is very important, so work**
 1221 **hard to get the material in here!**. Both signal regions satisfy a E_T^{miss} threshold 200 GeV
 1222 E_T^{miss} to be efficient in the E_T^{miss} trigger. The optimal cut on E_T^{miss} to achieve best

Variable	Requirement
E_T^{miss}	> 200 GeV
Leading jet $p_T(j_1)$	> 100 GeV
$ \Delta\phi(j_1, E_T^{\text{miss}}) $	> 2.0
$\min \Delta\phi(\text{all jets}, E_T^{\text{miss}}) $	> 0.4
$N_{\text{b-jet}}^{20}$, 85% WP	Exactly zero
N_{leptons}	Exactly two signal leptons
Lepton charge and flavor	$e^\pm e^\mp$ or $\mu^\pm \mu^\mp$
Leading electron (muon) $p_T^{\ell_1}$	> 5(5) GeV
Subleading electron (muon) $p_T^{\ell_2}$	> 4.5(4) GeV
$m_{\tau\tau}$	Veto [0, 160] GeV
$m_{\ell\ell}$	> 1, < 60 GeV, veto [3, 3.2] GeV
$\Delta R_{\ell\ell}$	> 0.05

1223 signal over background discrimination might be lower (maybe say here what the E_T^{miss}
 1224 cut affets most and how to qualify or quantify this statement), but with increasing
 1225 luminosity and average μ , the lowest unprescaled E_T^{miss} trigger thresholds only went
 1226 up, not down, as dating taking continued through 2016. The E_T^{miss} requirement sculpts
 1227 the topology of the signal to prefer events where the direction of the E_T^{miss} and the
 1228 direction of the leading jet are opposite each other in the transverse plane. Due to
 1229 small mass-splittings leading to such soft decay products, the NLSP daughters of the
 1230 electroweakinos or sleptons will typically only get significant enough E_T^{miss} to pass the
 1231 E_T^{miss} signal region cut when they are oppositely aligned in the transverse plane with
 1232 the hadronic initial state radiation.

1233 The slepton and Higgsino analyses have different $\Delta R_{\ell\ell}$ requirements. Refer to
 1234 the plots that shows the comparison of the Higgsino $\chi_2^0 \chi_1^+$ and the slepton signals in
 1235 $\Delta R_{\ell\ell}$ for 10 GeV and 20 GeV mass-splittings.

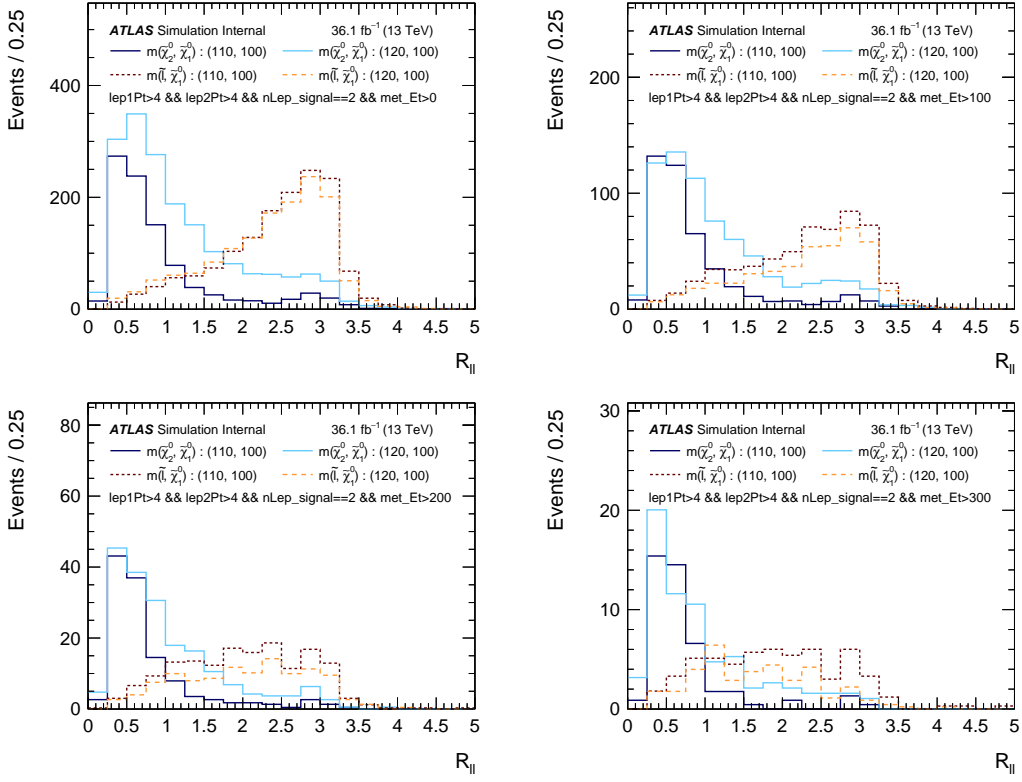


Figure 6.2: Comparison of Higgsino N2C1p (solid) and slepton (dashed) signals in the $R_{\ell\ell}$ variable for 10 GeV (dark) and 20 GeV (light) mass splittings. The E_T^{miss} here acts as a proxy for the boost of the system. Only a 2 signal lepton selection is applied.

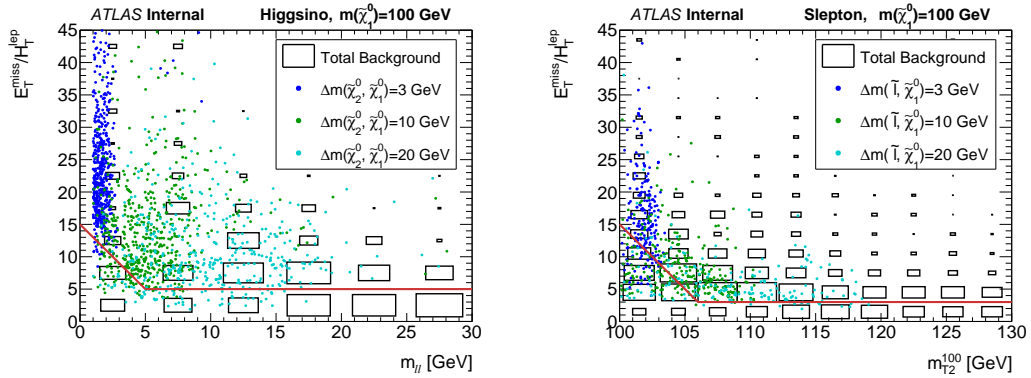


Figure 6.3: Distributions of $E_T^{\text{miss}}/H_T^{\text{leptons}}$ for the Higgsino (left) and Slepton (right) selections, after applying all signal region cuts except those on the $E_T^{\text{miss}}/H_T^{\text{leptons}}$, m_{ll} , and m_{T2} . The black dashed line indicates the cut applied in the signal region; events in the region below the black line are rejected.

Variable	Selections optimised for sleptons					
$E_T^{\text{miss}}/H_T^{\text{leptons}}$	> Max (3.0, 15 – 2 · [m_{T2}^{100} / GeV – 100])					
SRee-, SRmm-	eMT2a	eMT2b	eMT2c	eMT2d	eMT2e	eMT2f
m_{T2}^{100} [GeV]	[100, 102]	[102, 105]	[105, 110]	[110, 120]	[120, 130]	≥ 130
SRSF-	iMT2a	iMT2b	iMT2c	iMT2d	iMT2e	iMT2f
m_{T2}^{100} [GeV]	< 102	< 105	< 110	< 120	< 130	≥ 100

1236 6.3 Slepton Signal Regions

1237 This signal region based on MT2 cuts. Make different tables that make more
 1238 sense on the surface.

1239 6.4 Higgsino Signal Regions

1240 This signal region based on Mll cuts

Variable	Selections optimised for Higgsinos							
$E_T^{\text{miss}}/H_T^{\text{leptons}}$	> Max (5.0, $15 - 2 \cdot m_{\ell\ell}/\text{GeV}$)							
$\Delta R_{\ell\ell}$	< 2.0							
$m_T^{\ell_1}$	< 70 GeV							
SRee-, SRmm-	eMLLa	eMLLb	eMLLc	eMLLd	eMLLe	eMLLf	eMLLg	
$m_{\ell\ell} [\text{GeV}]$	[1, 3]	[3.2, 5]	[5, 10]	[10, 20]	[20, 30]	[30, 40]	[40, 60]	
SRSF-	iMLLa	iMLLb	iMLLc	iMLLd	iMLLe	iMLLf	iMLLg	
$m_{\ell\ell} [\text{GeV}]$	< 3	< 5	< 10	< 20	< 30	< 40	< 60	

1241 6.5 Conclusion

1242 Here say some final summarizing remarks and reference these final cutflow

1243 plots. Say something about non-normalized cutflow with significance plot showing how

1244 the significance for signal improves as more cuts are added.

1245 Show signal region plots?

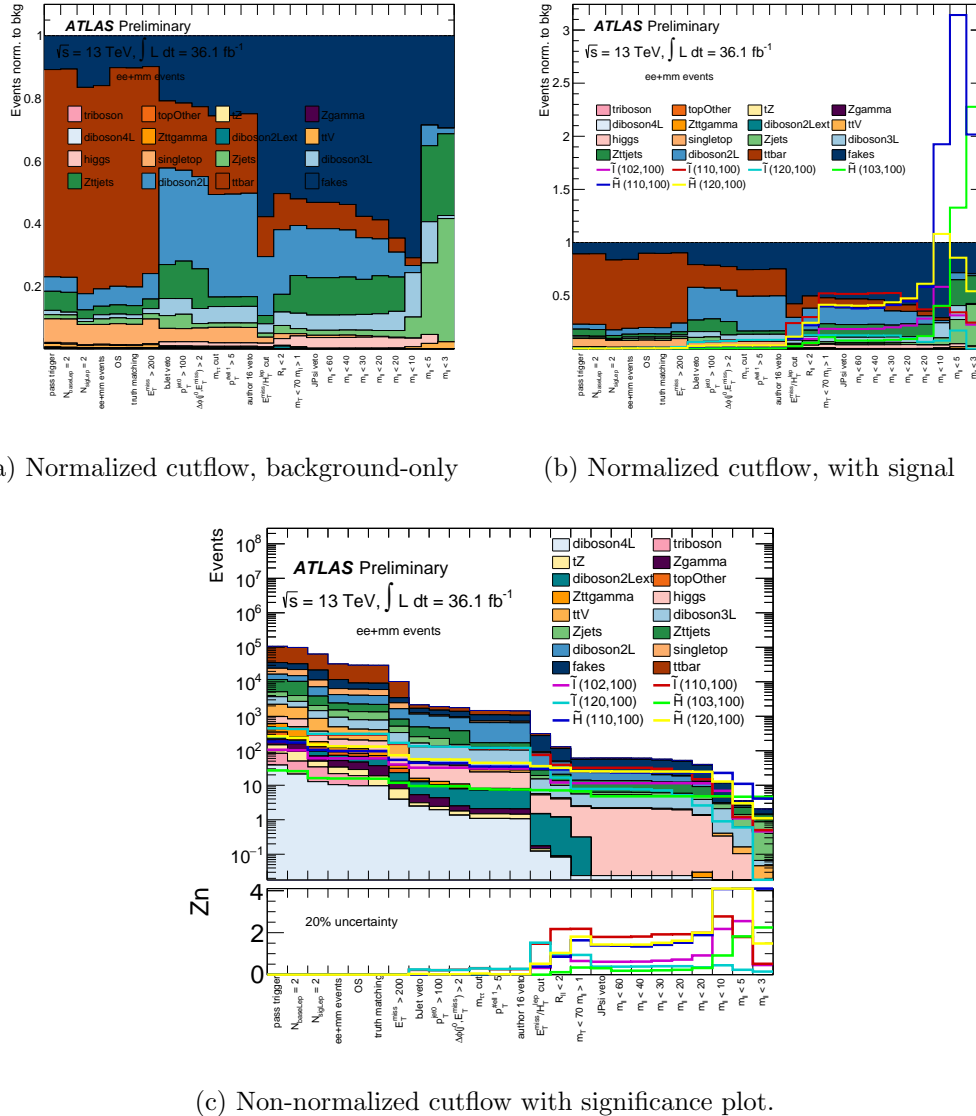


Figure 6.4: Normalized Cutflow for background-only, signal-inclusive, and non-normalized cut-flow with significance plots.

₁₂₄₆ **Chapter 7**

₁₂₄₇ **Background Estimation**

₁₂₄₈ Here just introduce the flow of the chapter and that the dominant background
₁₂₄₉ from detector induced lepton mismeasurements is discussed in a dedicated chapter. The
₁₂₅₀ background estimation strategy, with a description of the control and validation regions
₁₂₅₁ is discussed in Section 7.1. Next, in Section 7.2 estimation of the irreducible ($t\bar{t}$, $Z \rightarrow \tau\tau$,
₁₂₅₂ $VV \rightarrow \ell\nu\ell\nu$) backgrounds is explained. Lastly, in Section 7.3, the backgrounds from
₁₂₅₃ Drell-Yan processes with instrumental E_T^{miss} is described. The fake and non-prompt
₁₂₅₄ contribution is discussed is the next chapter.

₁₂₅₅ **7.1 Summary of estimation strategy**

₁₂₅₆ The majority, if not all, of the LHC collisions produces Standard Model pro-
₁₂₅₇ cesses, some of which look the same as Higgsino or slepton signal and sneak into the
₁₂₅₈ signal regions. Table 7.1 succinctly summarizes, in order of greatest contribution to
₁₂₅₉ least, the processes that contribute to the backgrounds, the type of background, and

1260 the method for estimating it.

1261 The dominant irreducible backgrounds come from $t\bar{t}$, tW , diboson, and $Z+jets$,
1262 where the Z -boson specifically decays to two τ leptons. A top quark decays to a b-quark
1263 and a W -boson nearly 100% of the time. In the event that a b-jet fails the b-tagging
1264 algorithm, each $t\bar{t}$ event can essentially be seen as a diboson event with additional jets
1265 and some special topological features. If both the W -bosons decay leptonically, you get
1266 two real leptons and E_T^{miss} from the neutrinos. Similarly, insufficiently b-tagged tW
1267 processes with leptonically decaying W -bosons also supply two real leptons, plus jets,
1268 and E_T^{miss} from neutrinos. Even when one or both the W -bosons decay hadronically, the
1269 tW and $t\bar{t}$ processes can still produce background events . This means that one or two
1270 of the 'signal' leptons arise from jets faking leptons in the detector.. These contributions
1271 are accounted for in the data-driven fake estimate described in the next chapter.

1272 Diboson events are WW , ZZ , and WZ . Fully leptonic WW production is the
1273 most prominent diboson background in the two lepton plus E_T^{miss} signal region. The
1274 fully leptonic WW decays lead to two real leptons that likely have opposite charge, but
1275 are necessarily of the same flavor. The real E_T^{miss} in the event comes from the neutrinos,
1276 and an additional hard jet must be present in the event. Fully leptonic WZ events can
1277 also find their way into the signal region since there is certainly an oppositely signed
1278 same flavor lepton pair from the Z, and real E_T^{miss} from the neutrino in the W decay,
1279 but the third lepton must fail identification for this be selected as a signal event. Semi-
1280 leptonic ZZ and WZ processes can pass signal selection if one Z decays into a proper
1281 lepton pair and the quarks from the other vector boson induce enough E_T^{miss} to pass

1282 the E_T^{miss} trigger. In the fully hadronic cases, there are four jets, two of which must
1283 be misidentified as leptons, leaving the other to induce a significant amount of E_T^{miss} .

1284 These contributions are negligible.

1285 In $Z(\rightarrow \tau\tau)$ +jets events, each leptonically decaying τ lepton produces one
1286 charged lepton and two neutrinos. On the occasion that these leptons form an OSSF
1287 pair, this process well mimics signal events. The top and $Z(\rightarrow \tau\tau)$ +jets backgrounds
1288 are estimated with a semi-data-driven approach where the estimate is done in dedi-
1289 cated control regions designed to be enriched in the particular process. The diboson
1290 backgrounds are evaluated with a combination of Monte Carlo and a validation region
1291 exploiting E_T^{miss}/H_T .

1292 Control and validation regions are designed to be kinematically similar to each
1293 other and, most importantly, to the signal regions, but statistically orthogonal so to not
1294 share events. Control regions are expected to have low signal contamination... **make**
1295 **table?**

1296 The Drell-Yan process contributes to SM backgrounds by E_T^{miss} induced by the
1297 mis-measurement of jet energy.. the rate is low and estimated using only Monte Carlo
1298 techniques.

1299 Rare processes.. what are they?

1300 Say something to segue into the next chapter all about the primary background
1301 for the analysis.

Background Process	Origin in Signal Region	Estimation Strategy
Fakes ($W+jets$, $VV(1\ell)$, $t\bar{t}(1\ell)$)	Reducible, jet fakes 2 nd ℓ	Fake factor, same sign VR
$t\bar{t}$, $tW(2\ell)$	Irreducible, b-jet fails ID	CR using b-tagging
$Z \rightarrow (ee, \mu\mu) + jets$	Instrumental E_T^{miss}	Monte Carlo (MC)
VV	Irreducible ($\ell\ell\ell\ell$), missed 3 rd ℓ	MC, VR using E_T^{miss}/H_T
$Z \rightarrow (\tau\tau) + jets$	Irreducible ($\tau\tau \rightarrow \ell\nu\ell\nu$)	CR using $m_{\tau\tau}$
Low mass Drell-Yan	Instrumental E_T^{miss}	MC, data-driven cross check
Other rare	Irreducible leptonic decays	MC

Table 7.1: Background estimation summary

1302 7.2 Irreducible Backgrounds

1303 This section describes the control regions constructed $t\bar{t}$ and $Z(\rightarrow \tau\tau) + jets$
 1304 backgrounds.

1305 7.2.1 Top Control Region (CR-top)

1306 One of the most unique aspect of the top quark signature is the presence
 1307 of a b-jet. To enrich a dilepton sample in top quarks, at least one b-tagged jet is
 1308 required in each event. The control region is centered around this requirement. The
 1309 dilepton invariant mass is restricted to $m_{\ell\ell} < 60$ GeV to stay kinematically consistent
 1310 with the dilepton signal region. **Say something about E_T^{miss}/H_T** A dilepton pair is
 1311 required for CR-top, since the top and W decay widths to electrons versus muons is
 1312 identical, different flavor lepton pairs are statistically the same and are accepted in
 1313 CR-top selection. **..the last sentence is just horrible.** Figures 7.1 and 7.2 show the
 1314 distributions of some of the variables used to define the Higgsino and slepton signal
 1315 regions. **Say more about these plots.**

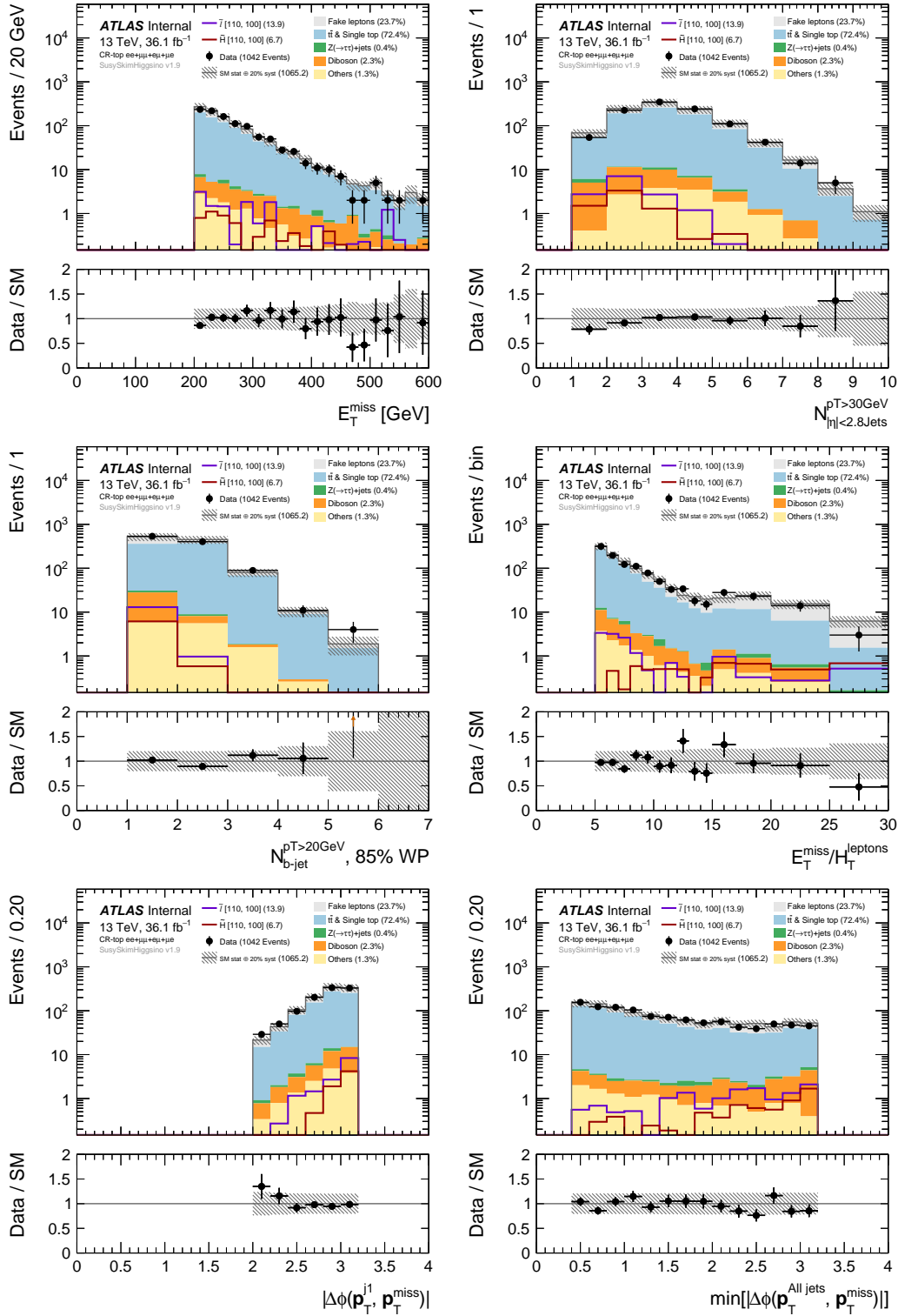


Figure 7.1: CR-top $ee + \mu\mu + e\mu + \mu e$ channel, pre-fit distributions.

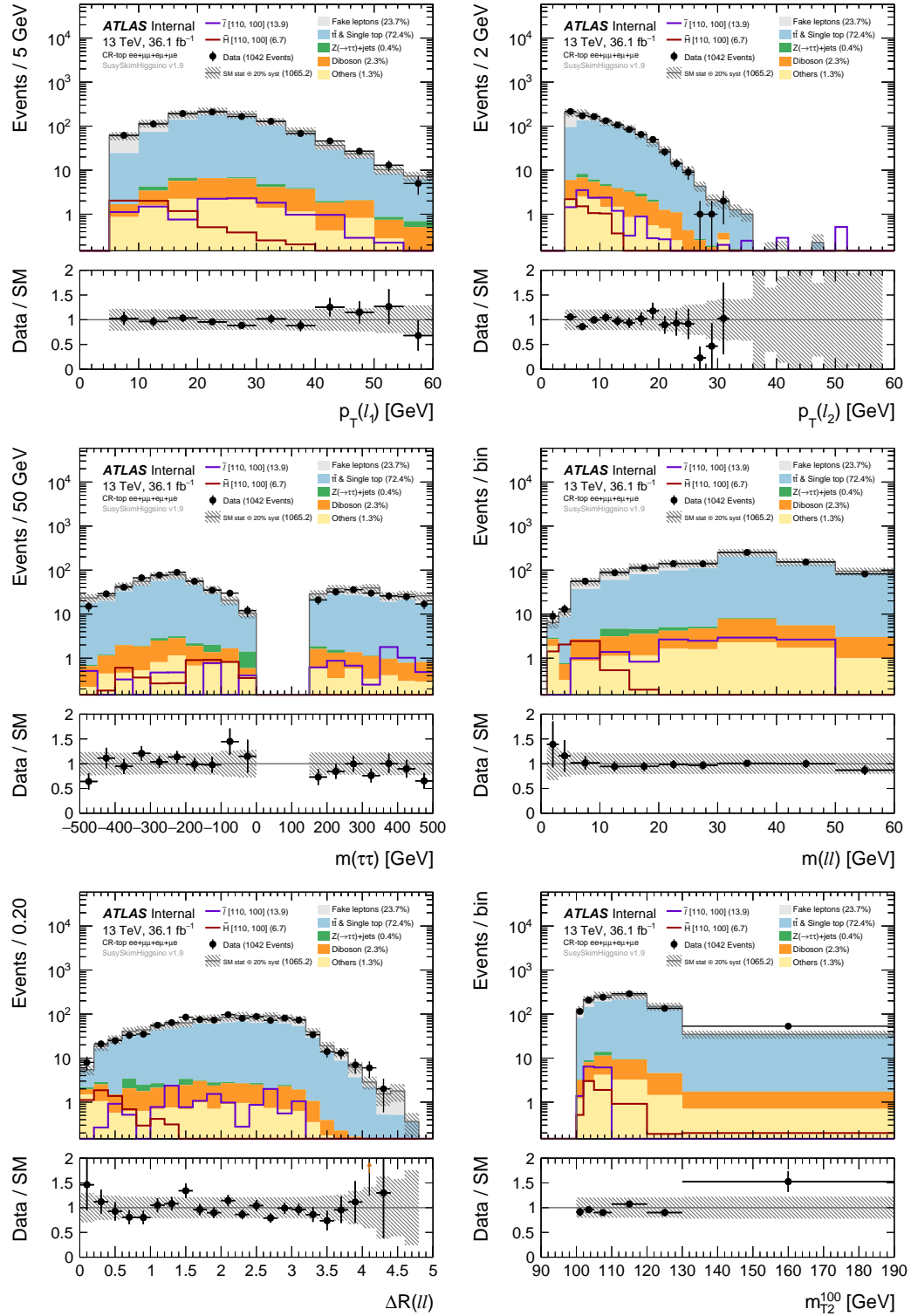


Figure 7.2: CR-top $ee + \mu\mu + e\mu + \mu e$ channel, pre-fit distributions.

1316 **7.2.2 Dita Control Region (CR-tau)**

1317 Getting a handle of the invariant mass of a dita system is the clearest ap-
1318 proach to constructing a dilepton sample enriched in $Z \rightarrow \tau\tau$ events. The $m_{\tau\tau}$ variable,
1319 described in section ??, is shown to do a good job blah blah. Events in CR-tau are
1320 required to have an $m_{\tau\tau}$ between 60 GeV and 120 GeV as a way to envelope the Z mass.
1321 There are also upper and lower bounds on E_T^{miss}/H_T . Say something about allowing
1322 different flavor lepton pairs because of the lepton flavor universality.. Figures 7.3 and 7.4
1323 show distributions of the same variables used to define the Higgsino and slepton signal
1324 regions as show above to CR-top. **Say more about these plots**

1325 **7.2.3 Diboson Validation Region (VR-VV)**

1326 B-jet veto and $E_T^{\text{miss}}/H_T < 3.0$ requirement. Remember, signal samples should
1327 populate high H_T , which mitigates signal contamination. Figures ?? and?? show these
1328 distributions..

1329 Refer to plots

1330 Say something about the value of the $m_{\ell^+\ell^-}$ cut imposed

1331 **7.2.4 Different flavor validation regions**

1332 The purpose of these VRs is to check the eventual extrapolation of the fitted
1333 Monte Carlo prediction of the irreducible backgrounds that are symmetric in $ee + \mu\mu$
1334 and $e\mu + \mu e$. Figures such and such **still need to add this last set of figures.**

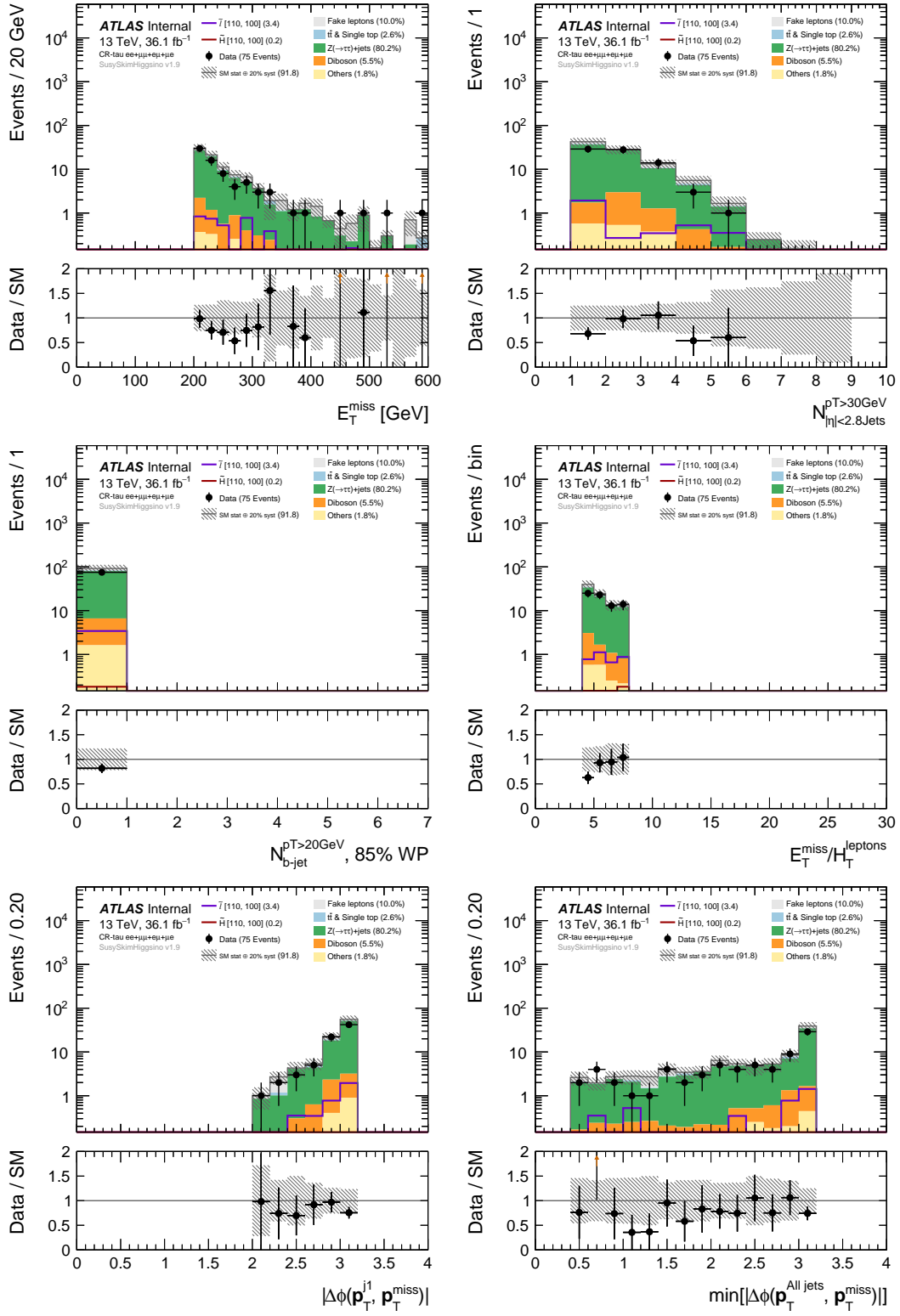


Figure 7.3: CR-tau $ee + \mu\mu + e\mu 70\mu$ channel, pre-fit distributions.

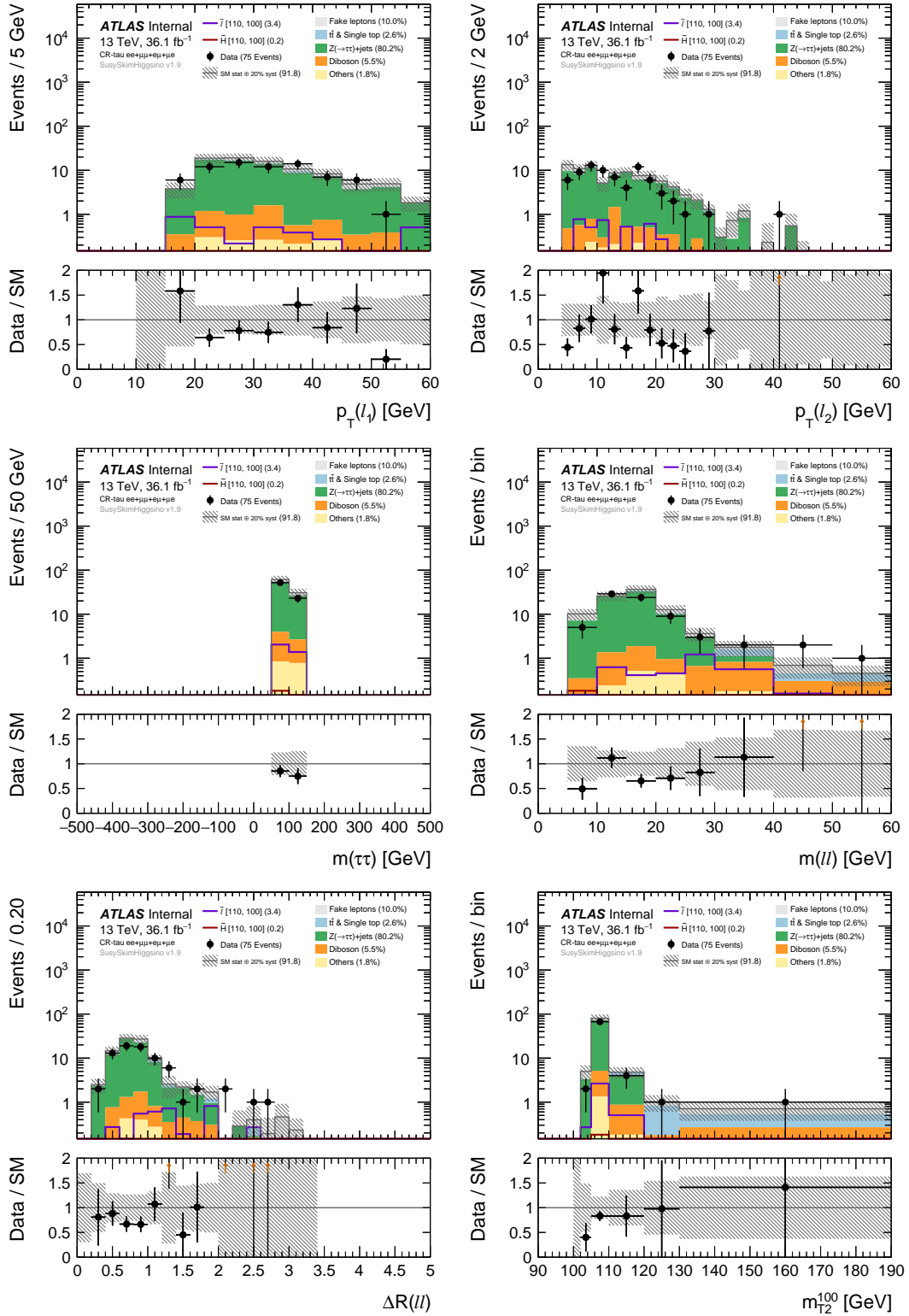


Figure 7.4: CR-tau ee + $\mu\mu$ + $e\mu 71 \mu$ channel, pre-fit distributions.

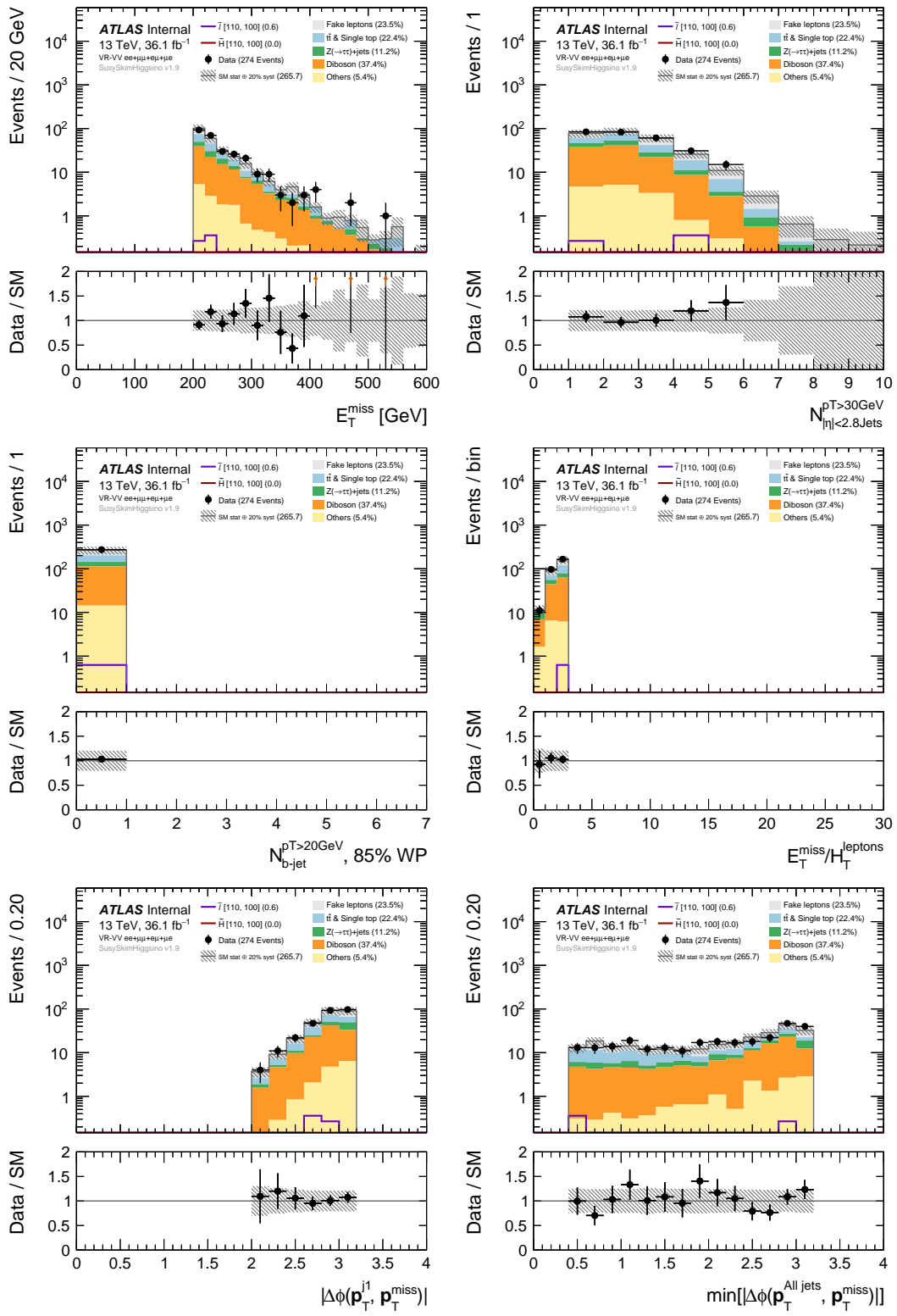


Figure 7.5: VR-VV $ee + \mu\mu + e\mu\tau\bar{\nu}\mu\tau$ channel, pre-fit distributions.

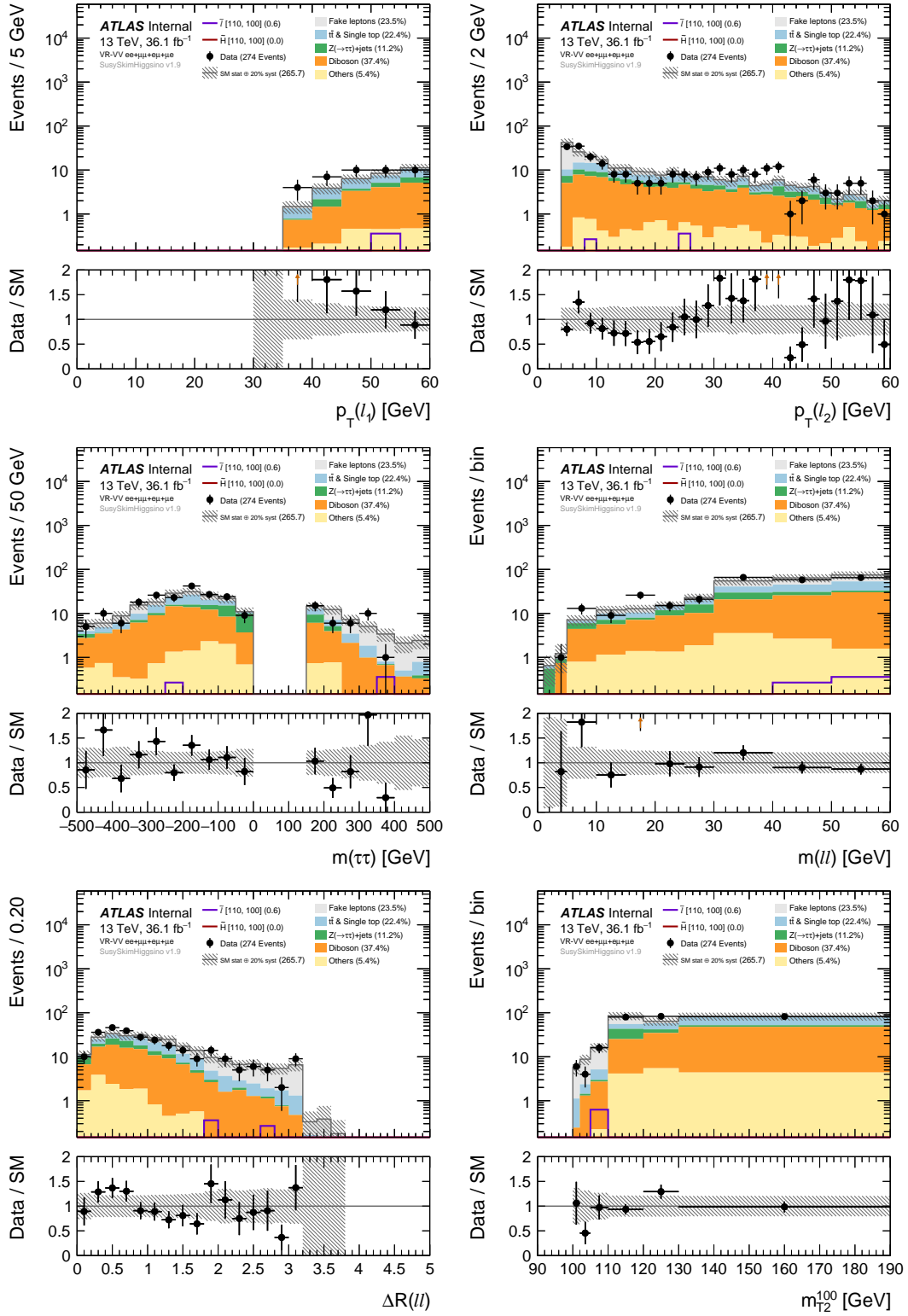


Figure 7.6: VR-VV $ee + \mu\mu + e\mu 78\mu$ channel, pre-fit distributions.

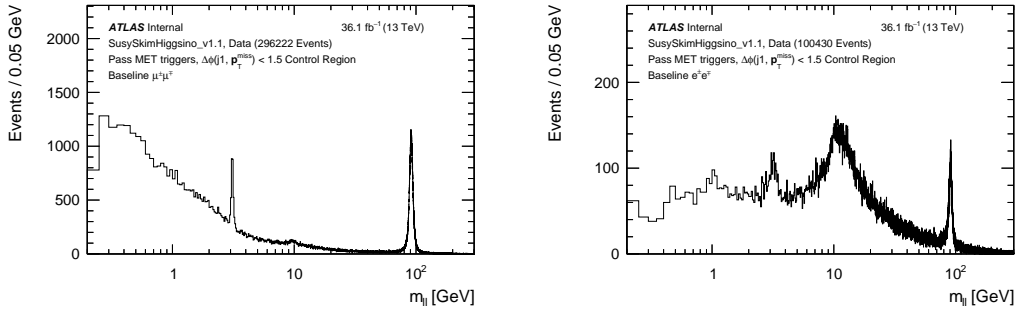


Figure 7.7: Data events passing inclusive E_T^{miss} triggers with opposite sign baseline leptons in the dilepton invariant mass $m_{\ell\ell}$ spectrum. The $\Delta\phi(j_1, \mathbf{p}_T^{\text{miss}})$ variable is inverted to ensure this is orthogonal to the signal region.

1335 7.3 Drell-Yan Background

1336 Off-shell $z \rightarrow ll$ events. Explain how these events get into the signal region.

1337 Because of the E_T^{miss} trigger, contribution small but not negligible.

1338 Refer to DY figures

1339 Two strategies are employed to reduce this background, what are they?

1340 After reducing this as much as possible, Monte Carlo estimates the remaining

1341 piece.

₁₃₄₂ **Chapter 8**

₁₃₄₃ **Fake Factor Method**

₁₃₄₄ There are two main types of backgrounds, irreducible and reducible. Irre-
₁₃₄₅ ducible backgrounds are Standard Model processes that produce the same particle final
₁₃₄₆ state as our BSM final state. In this case, Monte Carlo simulation is robust enough
₁₃₄₇ to model these background processes so their rates can be estimated in the data. Re-
₁₃₄₈ ducible backgrounds arise from Standard Model processes that should not produce the
₁₃₄₉ same final state as the signal; and yet, because of mismeasurements inside the detector,
₁₃₅₀ these events can still pass signal selection cuts. For low pt dilepton signals, the re-
₁₃₅₁ ducible fake background dominates and primarily comes from $W+\text{jets}$ events where one
₁₃₅₂ jets is misidentified as a lepton. Monte Carlo simulation does not model the detector
₁₃₅₃ shortcomings that lead to these mismeasurements very well, so the best estimate of this
₁₃₅₄ background must come from data. The "fake factor" method is a data driven approach
₁₃₅₅ to modeling backgrounds from particle misidentification in the detector by estimating
₁₃₅₆ the lepton fake rate with a set of data kinematically enriched in events producing fake

1357 leptons. The background estimate is validated in an orthogonal control region before it
1358 is estimated in the signal region.

1359 The rest of this chapter goes as follows: In Section 8.1, I will introduce fake
1360 leptons backgrounds more in detail, then in Section 8.2 I will give a general overview
1361 of the method used to estimate the fake lepton background for this analysis. The fake
1362 factor method applied to low p_T di-lepton events is explained for electrons and muons
1363 separately in Section 8.3 and the results are summarized in Section 8.4.

1364 8.1 Introduction

- 1365 • lepton identification and misidentification
 - 1366 • Compare production cross-sections of signal and W+jets processes
 - 1367 • Sources of electron and muon misidentification
 - 1368 • How to model backgrounds from misidentification (can't use MC, must choose
1369 data driven method)
 - 1370 • Concept of fake factor method
 - 1371 • Primary fake background is W+jets (multi-jet is minuscule... how do I qualify
1372 this?)
 - 1373 • Rest of chapter describes FF method in the context of my analysis
- 1374 Efficient lepton identification techniques make leptons powerful discriminators in AT-
1375 LAS physics searches with large background rejection and heavily suppressed QCD

1376 multi-jets. Jet suppression is very high in the range of lepton $p_T > 20GeV$ but degrades
1377 at lower lepton p_T . Misidentified electrons can be true but non-prompt electrons from
1378 photon conversions and heavy-flavor decays, where there is a real electron in the event
1379 that does not originate at the primary vertex like true, prompt electrons or they can be
1380 charged hadrons where the hadronic jet activity in the detector fakes an electron.

1381 **Make plot comparing production cross-sections, at least for W+jets and
1382 Higgsino/Slepton, and maybe even include other reducible background production cross-
1383 sections.

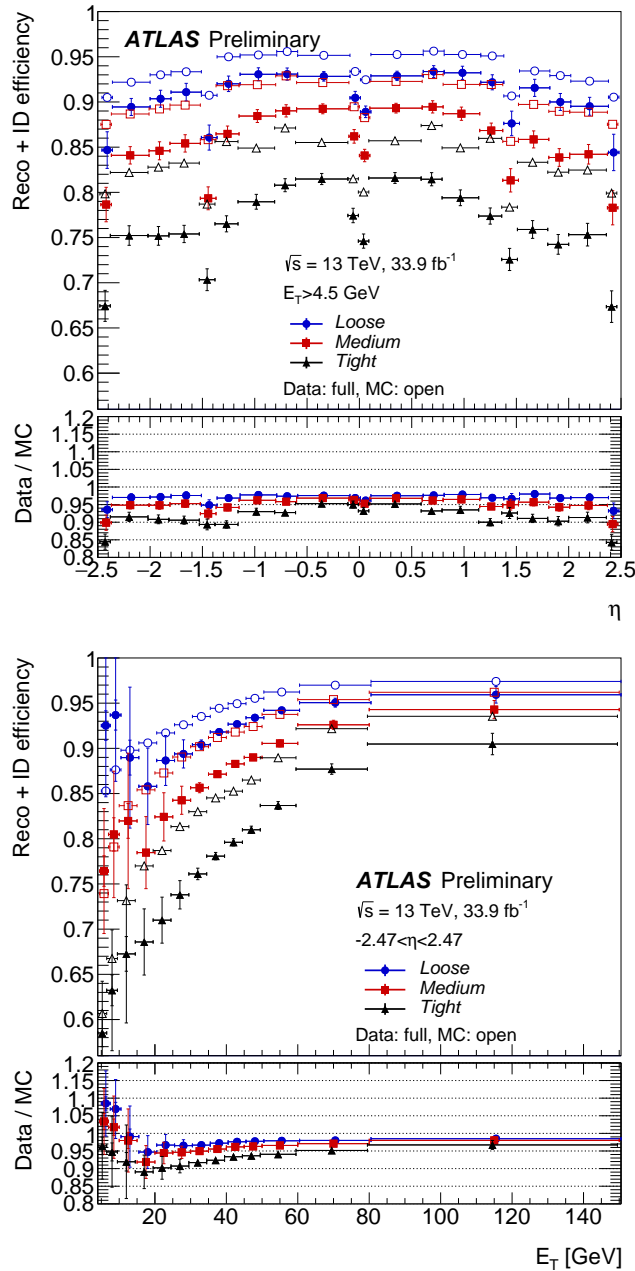


Figure 8.1: Electron identification efficiency

¹³⁸⁴ 8.2 Description of Fake Factor Method

- ¹³⁸⁵ • General description of fake factor method (measurement in control region then extrapolated to signal region)

- 1387 • We know what the signal region is already (described in Chapter ..)
- 1388 • Control region, meant to select events with misidentified leptons, is defined by
- 1389 signal region cuts but with one lepton chosen to satisfy a selection criteria that is
- 1390 more likely to include more misidentified particles than that used in the analysis
- 1391 signal region. A control region designed to capture W+jets events where a jet
- 1392 is misidentified as a lepton would be the same as the signal region requiring two
- 1393 leptons, but only one lepton is defined as an analysis lepton, while the other has
- 1394 at least one orthogonal selection criteria cut that makes it easier to include jets in
- 1395 the container of lepton identified in this particular way.
- 1396 • Electrons and muons are treated separately
- 1397 • Fake factor is the ratio of leptons passing analysis lepton identification criteria to
- 1398 the leptons passing anti-identification criteria, measured in a region of kinematic
- 1399 phase space contrived to be enriched in fake leptons. This will be considered as
- 1400 the fake factor measurement region in this thesis
- 1401 • Fake background contribution estimated by scaling the number of selected events
- 1402 in the control region by the fake factor.
- 1403 • Separate samples are used to measure the fake factor and count the number of
- 1404 events in the control region
- 1405 • control region and anti-ID lepton definition have contamination from sources that
- 1406 are not from the background of interest

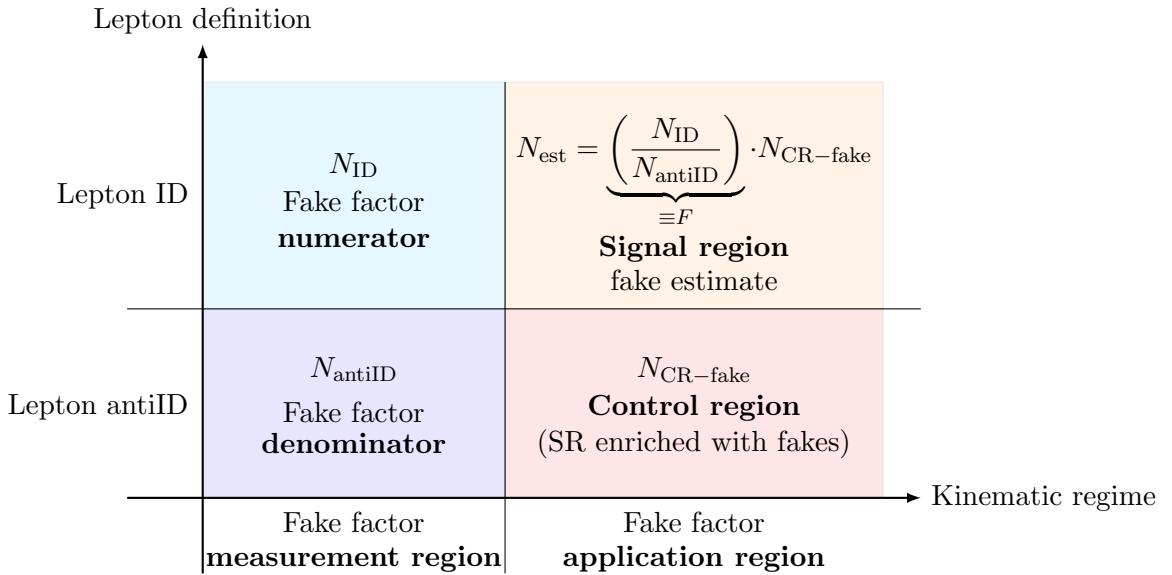


Figure 8.2: Schematic illustrating the fake factor method to estimate the fake lepton contribution in the signal region.

1407 Explain signal and control regions as well as fake factor measurement and
 1408 application regions.

1409 The fake factors are computed from events with $m_T < 40$ GeV, using the
 1410 distributions in Fig. 8.22, as:

$$F(p_T) = \frac{\text{Numerator}_{\text{data}} - \text{Numerator}_{\text{MC}}}{\text{Denominator}_{\text{data}} - \text{Denominator}_{\text{MC}}} \quad (8.1)$$

1411 8.3 Fake Factor Method Applied to Low- p_T Di-lepton Events

- 1412 • Describe data samples used for FF measurement
- 1413 • Describe data samples used for fake background estimate

Trigger	Prescaled Luminosity [pb ⁻¹]	
	2015	2016
HLT_e5_lhvloose	0.1	0.1
HLT_e10_lhvloose_L1EM7	0.5	0.8
HLT_e15_lhvloose_L1EM13VH	5.5	9
HLT_e20_lhvloose	10	17
HLT_mu4	0.5	0.5
HLT_mu10	2.3	2.5
HLT_mu14	25	14
HLT_mu18	26	48

Table 8.1: Pre-scaled single-lepton triggers from 2015 and 2016 used to compute the lepton fake factors. The pre-scaled luminosities shown are taken from `LumiCalc`.

- 1414 • Describe the single lepton triggers and how the pre-scales are unfolded to normalize
 1415 the entire 2015+2016 dataset to 10pb^{-1}

1416 8.3.1 Fake Lepton Composition

1417 Monte Carlo studies of fake and non-prompt lepton composition is done sepa-
 1418 rately for events with opposite sign lepton pairs and events with same-sign lepton pairs.
 1419 In the MC samples, there is a variable `MCTruthClassifier` that determines lepton cate-
 1420 gories based on their source. Real prompt leptons fall into two categories: *isolated* and
 1421 *lep* $\rightarrow \gamma \rightarrow \text{lep}$, which refers to truth matched leptons that arise from a Bremsstrahlung
 1422 to photon conversion process. Fake and non-prompt leptons occupy the remaining cat-
 1423 egories: *non-isolated*, which are mostly from heavy flavor decays, *photons*, which are
 1424 either photons faking leptons or actualy leptons from photon conversions, *hadron*, which
 1425 are from light flavor decays, and *unknown*, *unknown electron*, or *unknown muon*, which
 1426 are primarily from pile-up.

1427 (**Describe Figure 8.4 and Figure 8.3**). Sources of fake leptons in the di-muon and
1428 di-electron signal regions mostly come from heavy flavor decays, and fake leptons in the
1429 di-muon and di-electron control regions are primarily from light flavor decays. One im-
1430 portant result from this study is the similarity of fake lepton contribution between the
1431 opposite sign lepton pair and same sign lepton pair events. This gives confidence that
1432 the same-sign validation region can be successfully used to validate our fake background
1433 predictions in the data without accidentally unblinding our signal region and biasing
1434 the results.

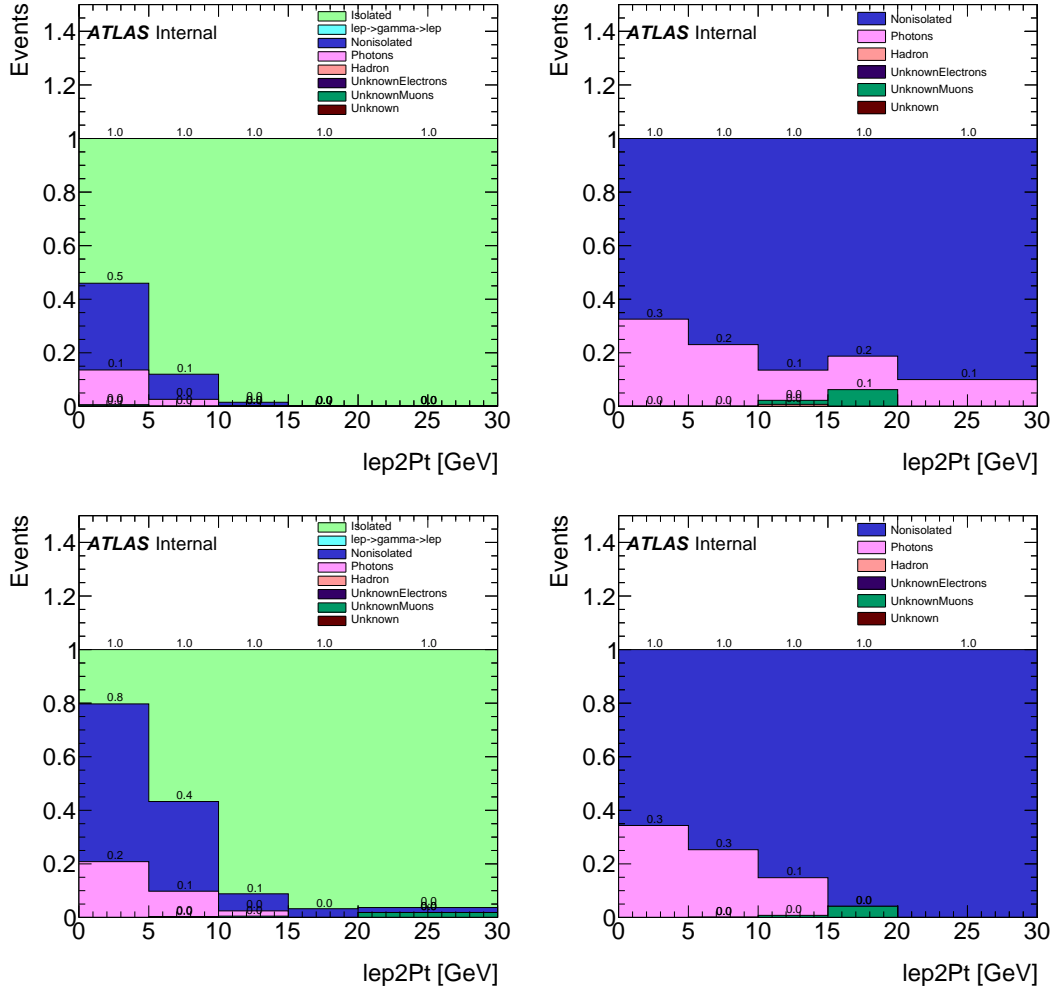


Figure 8.3: Fake lepton composition as a function of leading and subleading lepton p_T , with and without prompt (“Isolated” plus “ $\text{lep} \rightarrow \text{gamma} \rightarrow \text{lep}$ ”) leptons, for opposite sign muon pairs in the signal region.

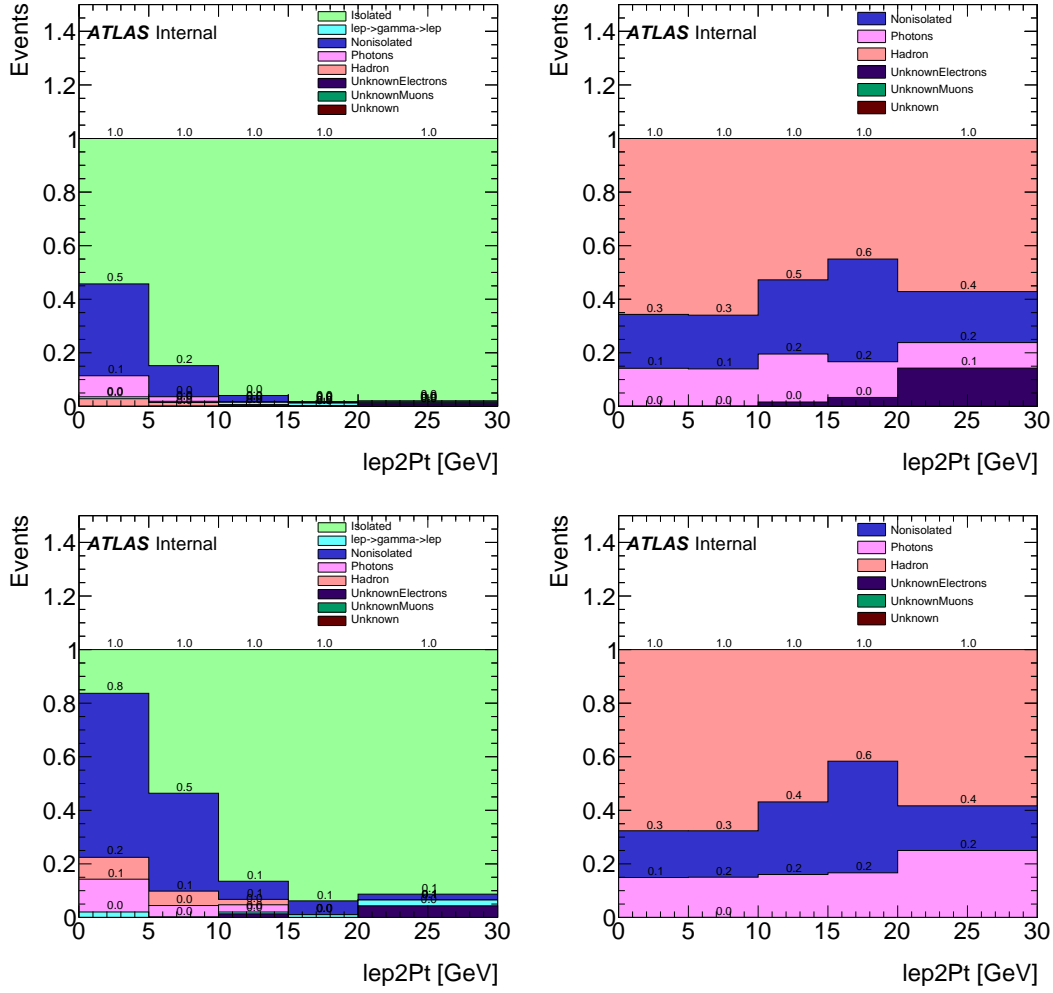


Figure 8.4: Fake lepton composition in opposite sign signal and control region as a function of leading and subleading lepton p_T , with and without prompt (“Isolated” plus “ $\text{lept} \rightarrow \text{gamma} \rightarrow \text{lept}$ ”) leptons, for opposite sign electron pairs in the signal region.

1435 **8.3.2 Anti-identified Lepton Definitions**

- 1436 • Anti-ID definition chosen to enhance fake and non-prompt leptons while suppress-
1437 ing real prompt leptons.
- 1438 • Enhancement is obtained by easing or inverting identification cuts used to suppress
1439 lepton misidentification
- 1440 • Tighter anti-ID cuts reduces systematic uncertainties on the fake background pre-
1441 diction.
- 1442 • Tighter anti-ID cuts increases the statistical uncertainty on the fake background
1443 prediction.

1444 **8.3.2.1 Anti-ID Muons**

1445 ID muons used for the fake factor calculation are the same as signal muons de-
1446 fined in Chapter ??, which are baseline muons that must pass `FixedCutTightTrackOnly`
1447 isolation and $|d_0/\sigma(d_0)| < 3.0$. Anti-ID muons are also baseline muons, but instead of
1448 requiring they pass the isolation and d_0 significance requirements of the ID muons, they
1449 instead must fail the `FixedCutTightTrackOnly` isolation or $|d_0/\sigma(d_0)| < 3.0$ criteria¹.
1450 Both the ID and anti-ID muons are required to pass the $|z_0 \sin \theta| < 0.5$ mm require-
1451 ment to reduce the impact of pileup. One notable difference with respect to the signal
1452 muon requirements is that the muon-jet overlap removal is relaxed when performing

¹Failing both the isolation and the d_0 significance cut still satisfies the anti-ID definition.

1453 the fake factor measurement². A summary of the ID and anti-ID muon definitions are
 1454 summarized in Table 8.2

1455 The decomposition of anti-ID muons in all events according to which set of ID
 1456 criteria failed is shown in Fig 8.5. The m_T distribution is plotted over the entire m_T
 1457 range, while the E_T^{miss} , p_T and η distributions are all shown for $m_T < 40$ GeV. Note
 1458 that these distributions are separated into categories: one for events with exactly zero
 1459 b -jets, and another for events with one or more b -jets. **Here explain more about**
 1460 **the 2 categories mentioned**

Signal Muon Definition	Anti-ID Muon Definition
$p_T > 4$ GeV $ \eta < 2.5$ $ z_0 \sin \theta < 0.5$ mm Pass <i>Medium Identification</i> $ d_0/\sigma(d_0) < 3$ Pass <i>FixedCutTightTrackOnly Isolation</i>	$ d_0/\sigma(d_0) > 3$ or Fail <i>FixedCutTightTrackOnly Isolation</i>)

Table 8.2: Summary of muon definitions.

²This enhances the statistics used for deriving the fake factors, and is motivated by the observation that the muon-jet overlap removal is primarily designed to reduce the number of heavy flavor decays which are inadvertently being classified as signal muons.

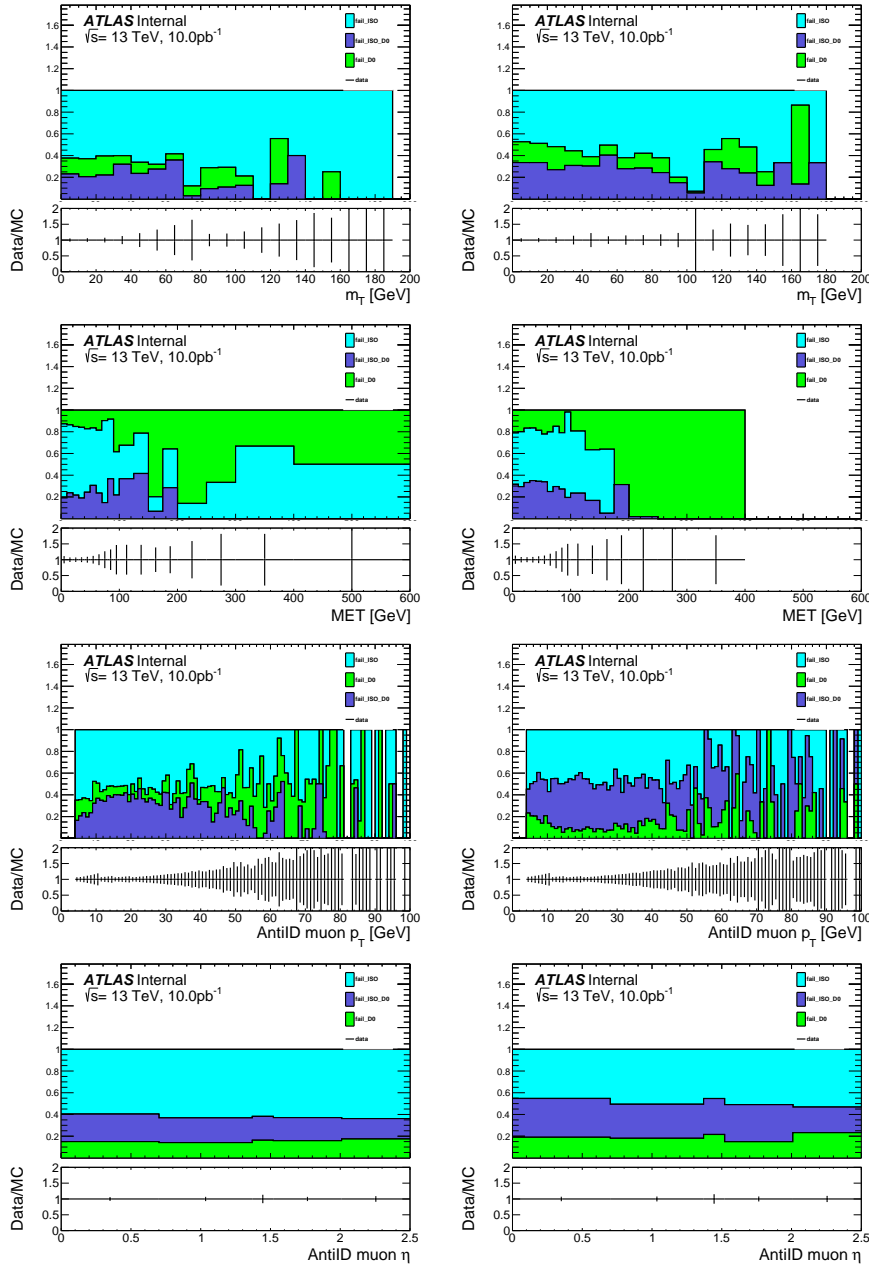


Figure 8.5: Anti-ID muon composition in events with exactly zero b -jets(left) and one or more b -jets(right) as a function of m_T , E_T^{miss} , muon p_T , and muon η . All but the m_T distribution corresponds to events with $m_T < 40 \text{ GeV}$.

1461 **8.3.2.2 Anti-ID Electrons**

1462 ID electrons are the same as signal electrons defined in Section ??, which
 1463 are baseline electrons that also pass `TightLLH` PID, `GradientLoose` isolation, and
 1464 $|d_0/\sigma(d_0)| < 5.0$. Anti-ID electrons are also baseline electrons that pass `LooseAndBLayerLLH`
 1465 PID but fail one of the signal selection criteria, i.e. they are required to fail at least one
 1466 of the `TightLLH`, `GradientLoose`, or $|d_0/\sigma(d_0)| < 5.0$ requirements. Studies motivat-
 1467 ing the definition of the anti-ID electrons were performed and are documented in this
 1468 section. All ID and anti-ID electrons are required to pass the $|z_0 \sin \theta| < 0.5$ mm re-
 1469 quirement to reduce the impact of pileup. The composition of anti-ID electrons in the
 1470 fake factor signal samples according to which set of ID criteria failed is shown in Fig 8.6.
 1471 The m_T distribution of this decomposition is plotted over the entire m_T spectrum, while
 1472 the E_T^{miss} , p_T and η distributions are all shown for $m_T < 40$ GeV.

Signal Electron Definition	Anti-ID Electron Definition
$p_T > 4.5$ GeV	
$ \eta < 2.47$	
$ z_0 \sin \theta < 0.5$ mm	
Electron <i>author</i> != 16	
Pass <i>Tight</i> Identification	Pass <i>LooseAbdBLayer</i> Identification (Fail <i>Tight</i> Identification or Fail <i>GradientLoose</i> Isolation or $ d_0/\sigma(d_0) > 5$)
Pass <i>GradientLoose</i> Isolation	

Table 8.3: Summary of electron definitions.

- 1473 • Dedicated study was done to find anti-ID electron definition that well models the
 1474 source of fake electron background. (Struggling with where to place this in this

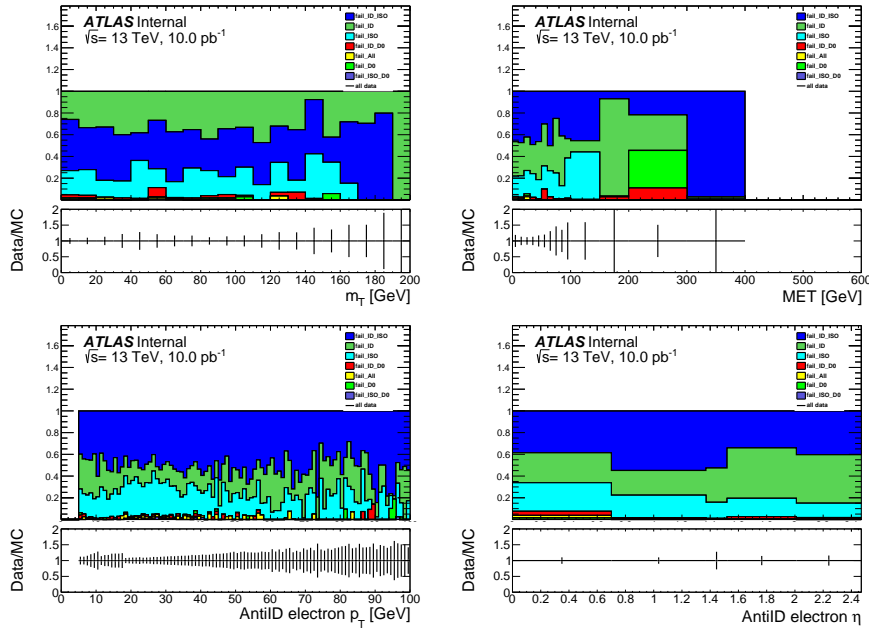


Figure 8.6: Fake electron composition as a function of m_T , E_T^{miss} , electron p_T , electron η . All distributions corresponds to events with $m_T < 40 \text{ GeV}$, excluding the m_T distribution.

1475

section.. before or after introducing the anti-ID definitions used)

1476

- Goal is to reduce the systematic uncertainty of the fake electron estimate

1477

- Tighter electron identification enhances fraction of heavy flavor decays

1478

- Requiring tracks to have a hit in the b-layer reduces fraction of fakes from conversions

1480

- Loose or Medium isolation requirement narrows source of fakes towards heavy and light hadronic decays

1482

- Requiring a large d_0/σ_{d_0} can increase the fraction of heavy flavor decays and conversions

1483

- 1484 ● Deciding which anti-ID definitions best models electron fake backgrounds is a
- 1485 balancing act.
- 1486 ● **Need help thinking through how in depth to go with this part.**

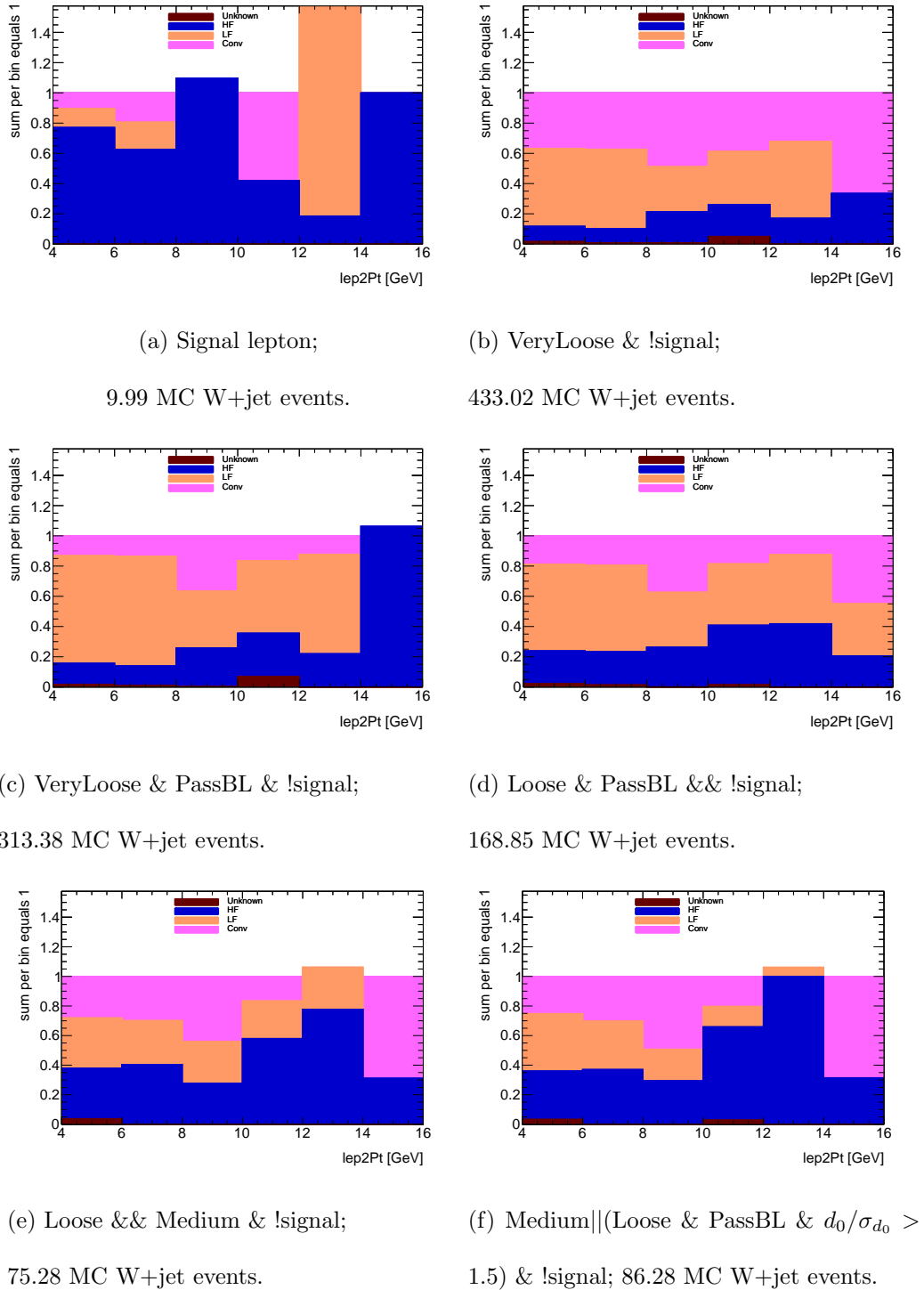


Figure 8.7: Fake lepton composition as a function of the subleading lepton p_T .

1487 **8.3.3 Fake Factor Measurement**

1488 **8.3.3.1 Muon Fake Factors**

1489 Both data and MC contributions to the numerator and denominator samples
1490 in the single-muon trigger sample are normalized to 10 pb^{-1} , to remove the effects
1491 of the prescales in the data. The MC is then re-scaled to the data in events with
1492 $E_T^{\text{miss}} > 200 \text{ GeV}$, a kinematic region expected to be pure in prompt leptons. For events
1493 with exactly 0 b -jets, the MC re-scaling factor for numerator muons is 1.01 ± 0.13 , for
1494 denominator muons it is 1.20 ± 0.29 . For events with one or more b -jets, the MC re-
1495 scaling factor for numerator muons is 1.24 ± 0.20 , for denominator muons it is 7.34 ± 5.00 .
1496 If instead, the MC is re-scaled to match the data for events with $m_T > 100 \text{ GeV}$, a region
1497 that should also be pure in prompt leptons, the re-scaling factors for events with exactly
1498 0 b -jets are 2.37 ± 0.10 for numerator muons and 11.68 ± 2.28 for denominator muons;
1499 events with one or more b -jets have re-scale factors 1.60 ± 0.06 for numerator muons and
1500 10.41 ± 6.34 for denominator muons. The re-scaling factors vary significantly between
1501 the two methods but the fake factors themselves exhibit small changes between the two
1502 methods and can be used as a systematic uncertainty.

1503 Distributions of E_T^{miss} and m_T for numerator and denominator muons for events
1504 with exactly zero b -jets are shown in Fig. 8.8, and for events with one or more b -jets in
1505 Fig. 8.9. Muon p_T distributions for events with exactly zero b -jet are shown in Fig. 8.10,
1506 and for events with one or more b -jets in Fig. 8.11.

1507 The fake factors are computed using events with $m_T < 40 \text{ GeV}$, using the

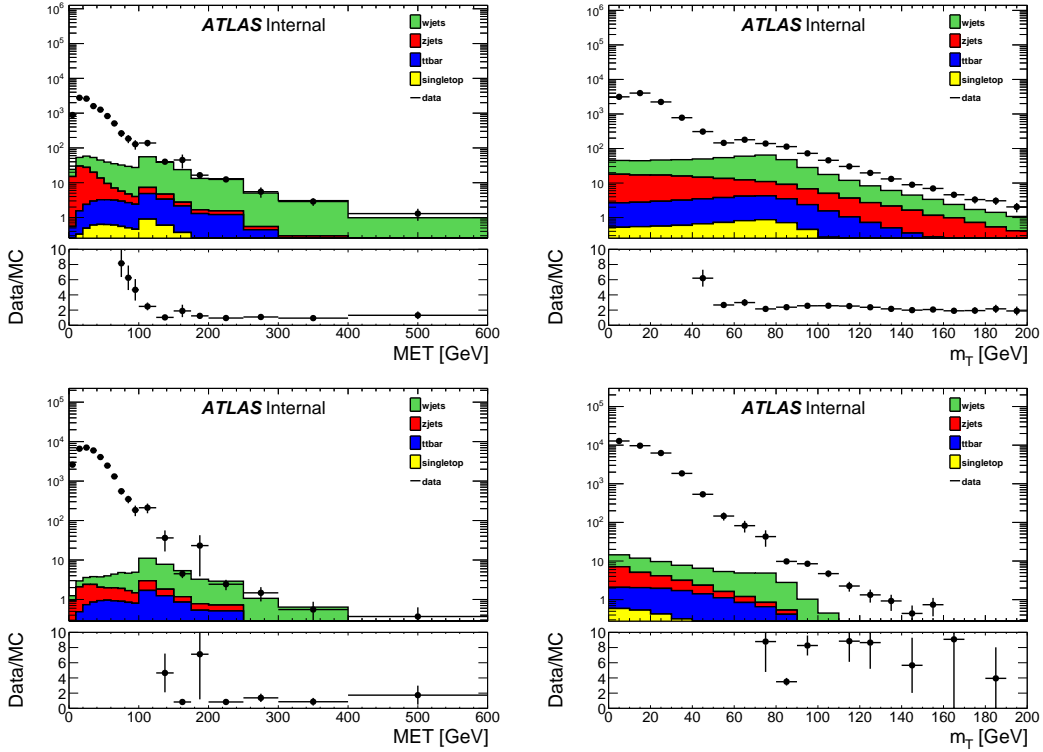


Figure 8.8: The E_T^{miss} (left) and m_T (right) distributions for numerator (top) and denominator (bottom) muons in the prescaled single-lepton-trigger sample for events with exactly zero b -jets. MC has been scaled to the data in the $E_T^{\text{miss}} > 200$ GeV region.

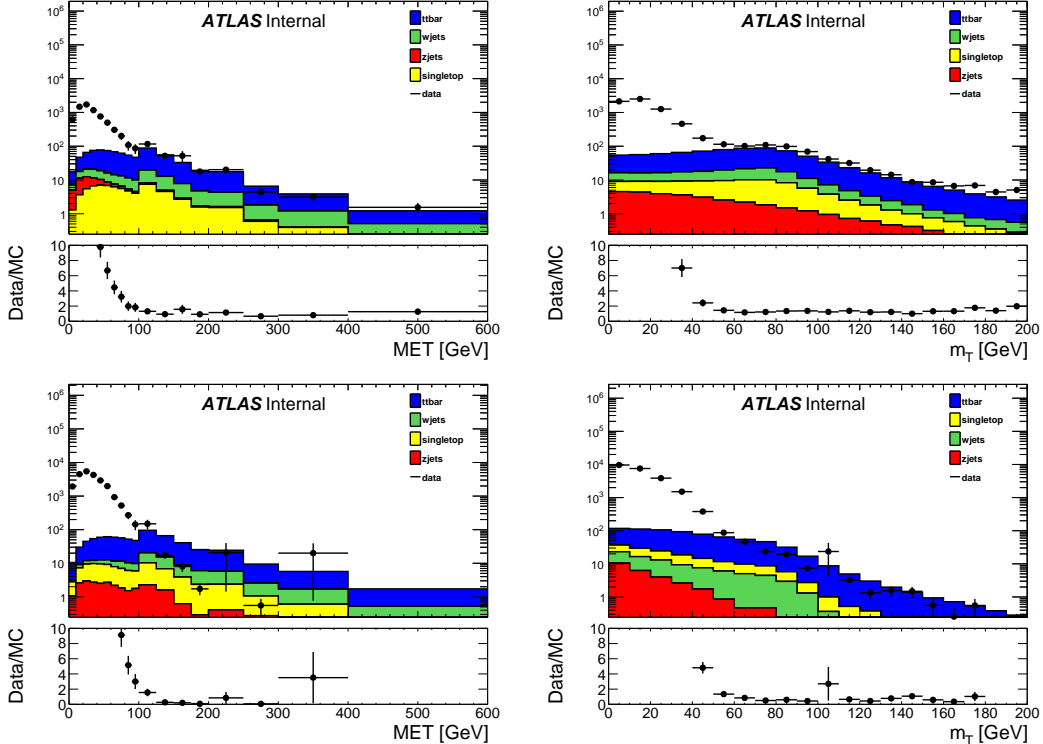


Figure 8.9: The E_T^{miss} (left) and m_T (right) distributions for numerator (top) and denominator (bottom) muons in the prescaled single-lepton-trigger sample for events with one or more b -jets. MC has been scaled to the data in the $E_T^{\text{miss}} > 200$ GeV region.

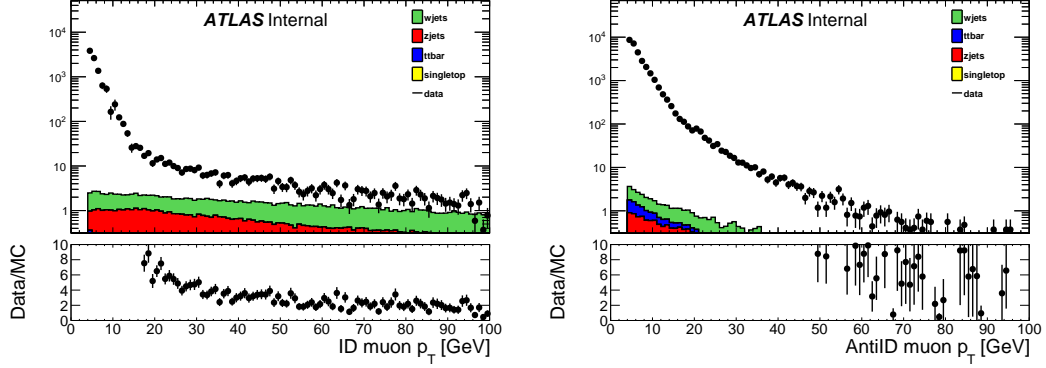


Figure 8.10: Muon p_T for numerator (left) and denominator (right) objects in the prescaled single-muon trigger sample for events with $m_T < 40 \text{ GeV}$. MC has been scaled to the data in the $m_T > 100 \text{ GeV}$ region. Distributions from [?].

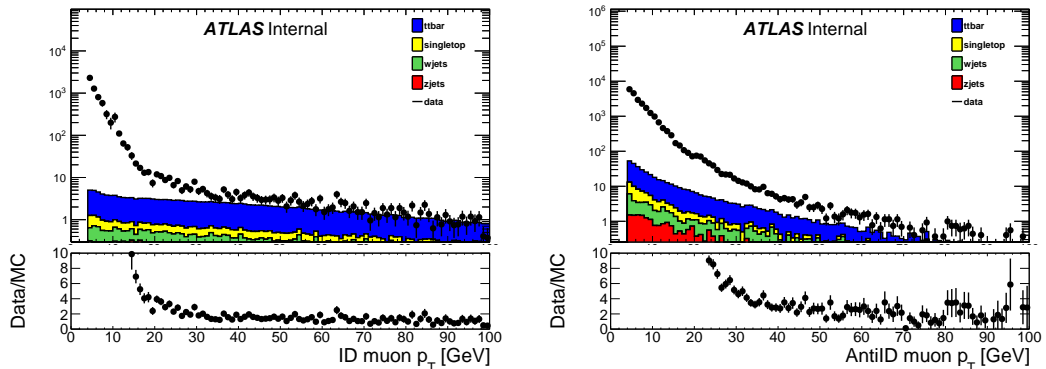


Figure 8.11: Muon p_T for numerator (left) and denominator (right) objects in the prescaled single-muon trigger sample for events with $m_T < 40 \text{ GeV}$. MC has been scaled to the data in the $m_T > 100 \text{ GeV}$ region. Distributions from [?].

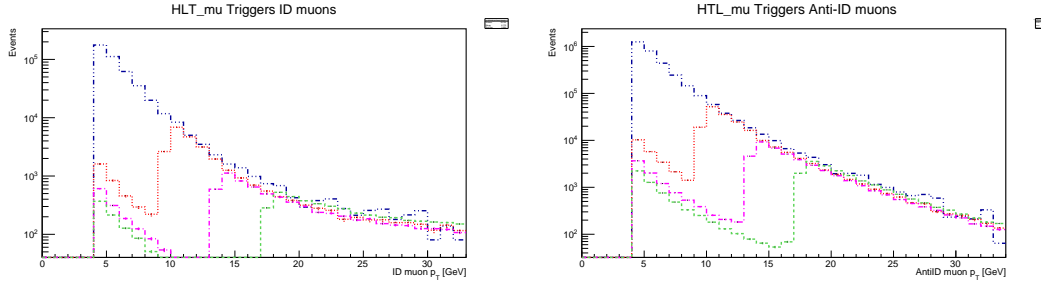


Figure 8.12: The numerator muon (left) and denominator denominator (right) p_T distributions for prescaled single-muon triggers, normalized to 1 pb^{-1} . Blue curve: HLT_mu4, red curve: HLT_mu10, purple curve: HLT_mu14, green curve: HLT_mu18.

1508 distribution in Figs. 8.10 and 8.11, as

$$F(p_T) = \frac{\text{Numerator}_{\text{data}} - \text{Numerator}_{\text{MC}}}{\text{Denominator}_{\text{data}} - \text{Denominator}_{\text{MC}}} \quad (8.2)$$

1509 where the fake factor F is computed in discrete p_T bins with different single-muon
 1510 triggers applied. The specific trigger applied to each range in lepton p_T was chosen
 1511 to reduce the effect of the trigger turn on and maintain good statistics. Muon p_T
 1512 distributions for the prescaled triggers shown in Fig. 8.12 are arbitrarily normalized to
 1513 1 pb^{-1} . HLT_mu4 trigger is required for muon p_T $4 - 11 \text{ GeV}$, HLT_mu10 is required for
 1514 muon p_T $11 - 15 \text{ GeV}$, HLT_mu14 is required for muon p_T $15 - 20 \text{ GeV}$, and HLT_mu18
 1515 is required for muon $p_T > 20 \text{ GeV}$. A table of these triggers and corresponding p_T range
 1516 is shown in Table 8.4

1517 Muon fake factors depend strongly on muon p_T , but also display a systematic
 1518 dependence on the leading jet p_T . Unlike the electron fake factors, there is also a separate
 1519 dependence on b -jet multiplicity. Fig. 8.13 shows the muon fake factors as functions of
 1520 muon p_T , leading jet p_T , and b -jet multiplicity before any hard jet requirement. Similar

el trigger	p_T range [GeV]
HLT_mu4	4–11
HLT_mu10	11–15
HLT_mu14	18–20
HLT_mu18	> 20

Table 8.4: Single-muon triggers used for fake factor computation and their corresponding p_T range.

1521 to the electron fake factor calculation, the fake factor measurement region requires a
 1522 hard jet of p_T greater than 100 GeV , but unlike the electron fake factors, the muon fake
 1523 factors are also separated into two b -jet multiplicity bins: exactly zero b -jets, and one or
 1524 more b -jets. The bin with exactly zero b -jets is used to estimate the fake contribution
 1525 in the signal region, and the bin with one or more b -jets is used to estimate the fake
 1526 contribution in the $t\bar{t}$ control region.

1527 The final fake factors are shown in Fig. 8.14 as a functions of muon p_T for each
 1528 of the b -jet multiplicity bins. In addition to the final fake factors binned in p_T , fake
 1529 factors binned in other variables are also inspected to check for significant trends:

- 1530 • Fake factors as a function of muon η are shown in Fig. 8.15,
- 1531 • Fake factors as a function of $\Delta\phi_{jet1-met}$ are shown in Fig. 8.16,
- 1532 • Fake factors as a function of jet multiplicity are shown in Fig. 8.17,
- 1533 • Fake factors as a function of average interactions per bunch crossing are shown in
 Fig. 8.18,
- 1534 • Fake factors as a function of the number of primary vertices are shown in Fig. 8.19.

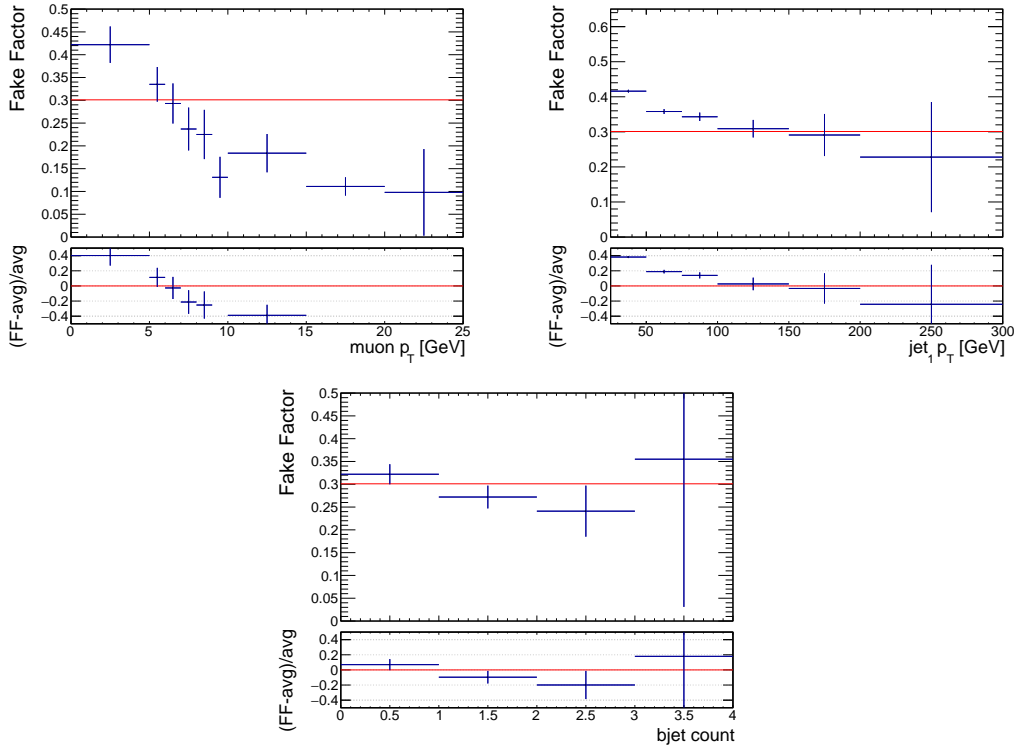


Figure 8.13: Muon fake factors *before* requiring a hard jet of $p_T > 100$ GeV, computed from single-muon prescaled triggers as a function of muon p_T (top-left), as a function of leading jet p_T (top-right), and as a function of b -jet multiplicity (bottom). A red line denotes the average muon fake factor over all muon p_T .

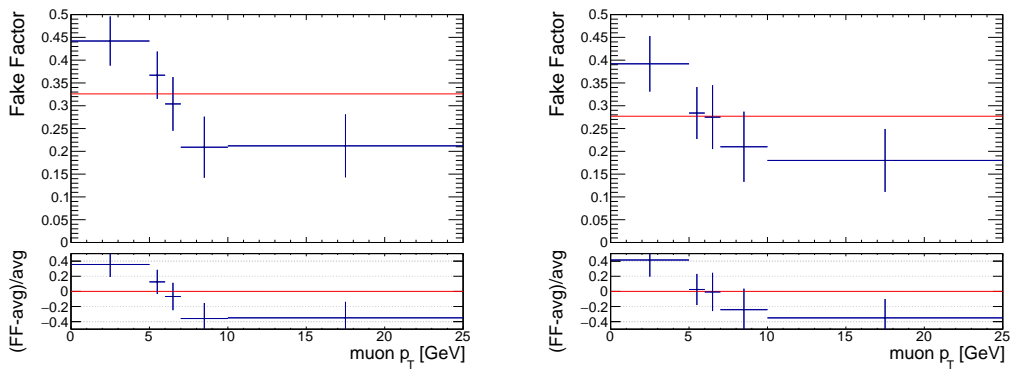


Figure 8.14: Muon fake factors computed from single-muon prescaled triggers as a function of muon p_T in events with exactly zero b -jets (left) and one or more b -jets (right). A red line denotes the average muon fake factor over all muon p_T .

1536 The relative uncertainties on the muons fake factors versus muon p_T for the separate
 1537 b -jet multiplicity bins are show in Fig. 8.20.

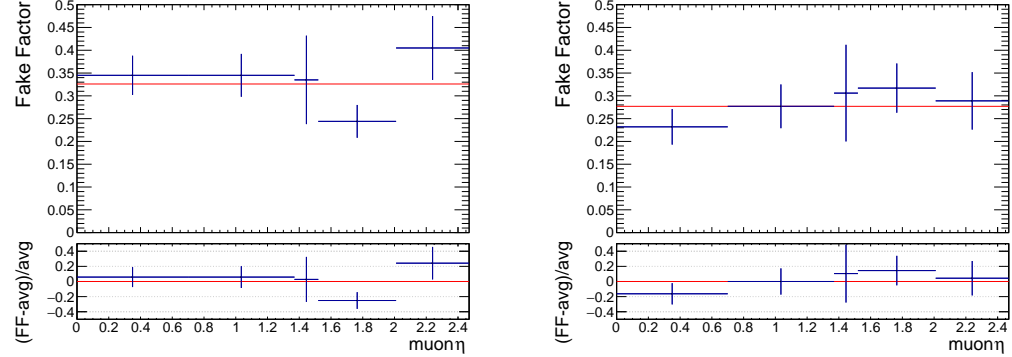


Figure 8.15: Muon fake factors computed from single-muon prescaled triggers as a function of muon η in events with exactly zero b -jets (left) and one or more b -jets (right). A red line denotes the average muon fake factor over all muon p_T .

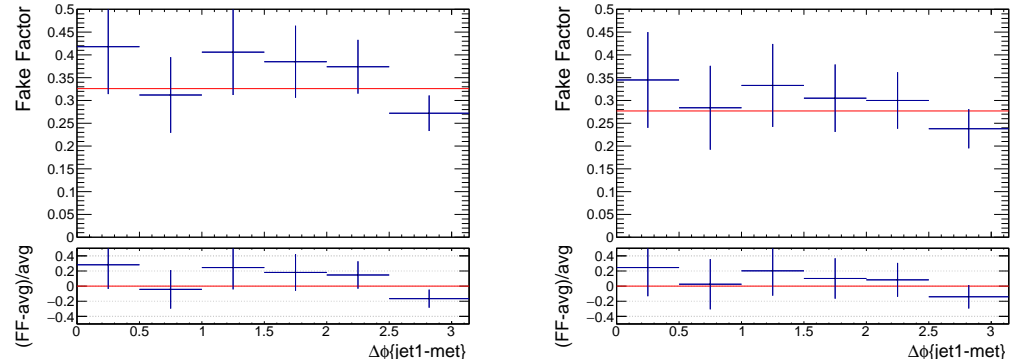


Figure 8.16: Muon fake factors computed from single-muon prescaled triggers as a function of $\Delta\phi_{jet-E_T^{\text{miss}}}$ in events with exactly zero b -jets (left) and one or more b -jets (right). A red line denotes the average muon fake factor over all muon p_T

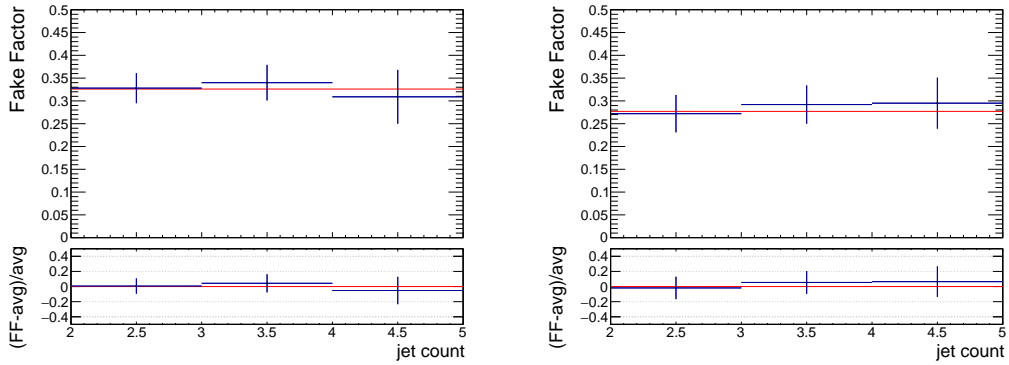


Figure 8.17: Muon fake factors computed from single-muon prescaled triggers as a function of the jet multiplicity in events with exactly zero b -jets (left) and one or more b -jets (right). A red line denotes the average muon fake factor over all muon p_T

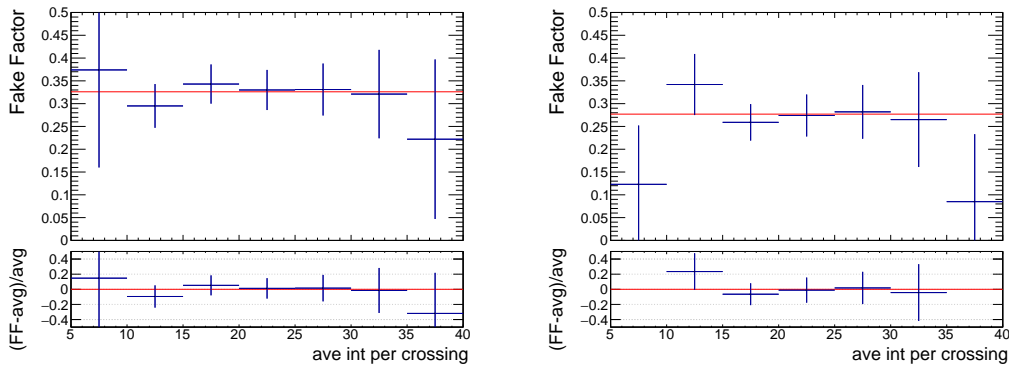


Figure 8.18: Muon fake factors computed from single-muon prescaled triggers as a function of the average number of interactions per bunch crossing in events with exactly zero b -jets (left) and one or more b -jets (right). A red line denotes the average muon fake factor over all muon p_T

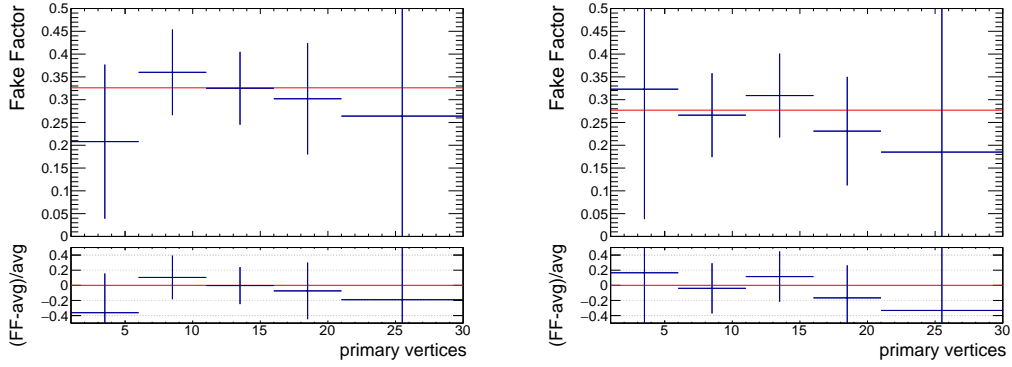


Figure 8.19: Muon fake factors computed from single-muon prescaled triggers as a function of the number of primary vertices in events with exactly zero b -jets (left) and one or more b -jets (right). A red line denotes the average muon fake factor over all muon p_T

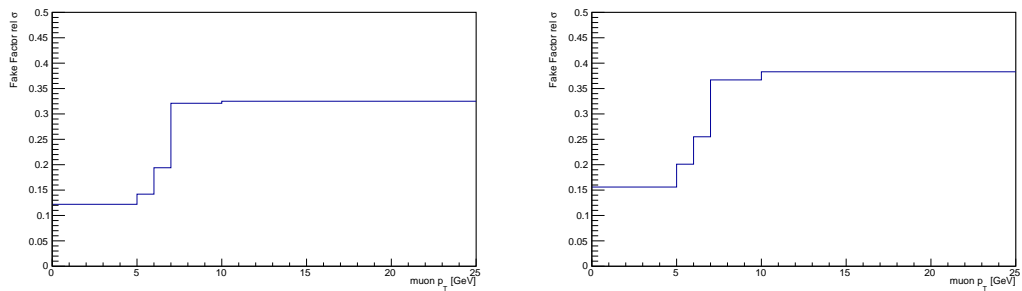


Figure 8.20: Relative uncertainties on muon fake factors versus muon p_T in zero b -jets bin (left) and one or more b -jets bin (right).

1538 **8.3.3.2 Electron Fake Factors**

1539 Electron fake factors show the largest dependance on electron p_T , but also
1540 display a dependence on the leading jet p_T , which is evident in Fig. 8.24 that shows
1541 electron fake factors as a function of electron p_T and leading jet p_T separately. Given
1542 this trend, and the fact that all signal regions used in this analysis require a hard jet
1543 with p_T greater than 100 GeV, we design the fake factor measurement region to also
1544 require a hard jet of p_T greater than 100 GeV. Fake factors as a function of other
1545 kinematic variables are also studied as a cross-check and for understanding systematic
1546 uncertainties.

1547 Final fake factors computed as a function of electron p_T are shown in Fig. 8.25a.
1548 In addition, fake factors as functions of other variables are also inspected to check for
1549 significant trends:

- 1550 • the dependence of the fake factors on $|\eta|$ is shown in Fig. 8.25b,
1551 • fake factors as a function of leading jet p_T and $\Delta\phi_{jet-E_T^{\text{miss}}}$ are shown in Fig. 8.26,
1552 • fake factors as a function of jet multiplicity and b -jet multiplicity are shown in

el trigger	p_T range [GeV]
HLT_e5_lvhloose	5–11
HLT_e10_lvhloose_L1EM7	11–18
HLT_e15_lvhloose_L1EM13VH	18–23
HLT_e20_lvhloose	> 23

Table 8.5: Single-Electron triggers used for fake factor computation and their corresponding p_T range.

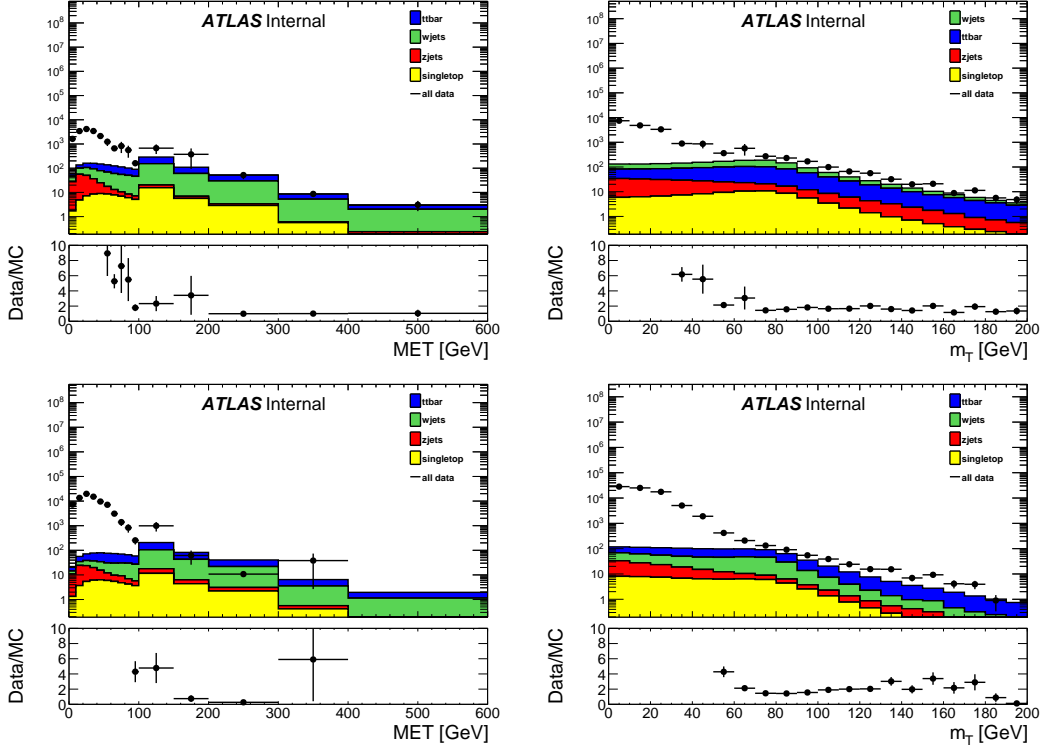


Figure 8.21: The E_T^{miss} (left) and m_T (right) distributions for numerator (top) and denominator (bottom) electrons in the pre-scaled single-lepton-trigger sample. MC has been scaled to the data in the $E_T^{\text{miss}} > 200$ GeV region.

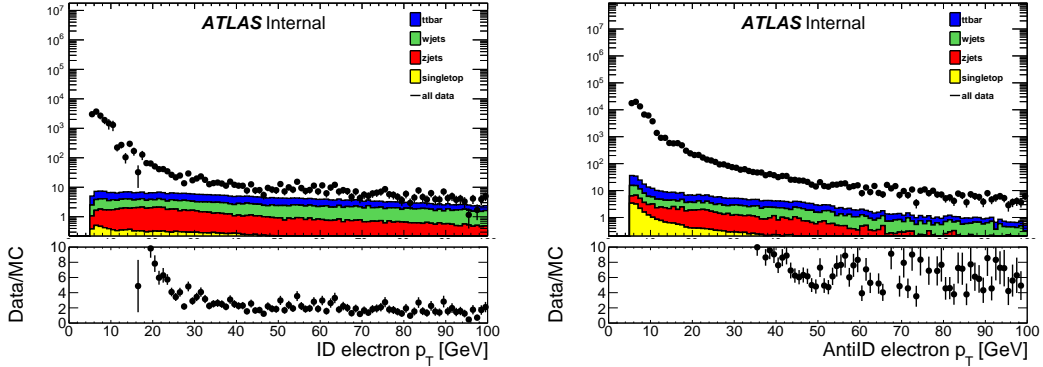


Figure 8.22: Electron p_T for numerator (left) and denominator (right) objects in the pre-scaled single-lepton-trigger sample for events with $m_T < 40\text{ GeV}$. MC has been scaled to the data in the $E_T^{\text{miss}} > 200\text{ GeV}$ region.

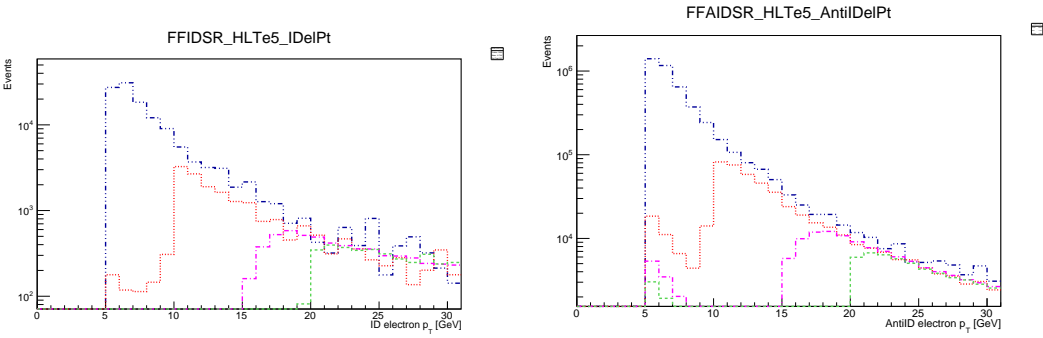


Figure 8.23: The numerator electron (left) and denominator electron (right) p_T distributions for pre-scaled single-lepton-trigger, normalized to 1 pb^{-1} . Blue curve: HLT_e5_lvhloose, red curve: HLT_e10_lvhloose_L1EM7, purple curve: HLT_e15_lvhloose_L1EM13, green curve: HLT_e20_lvhloose.

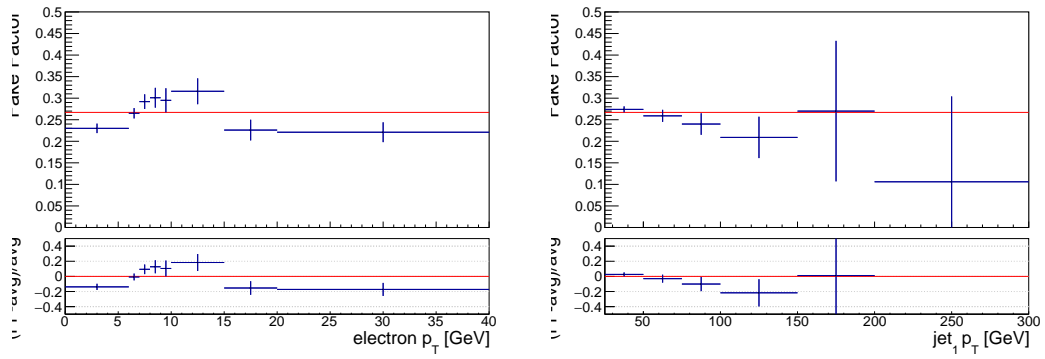


Figure 8.24: Electron fake factors *before* requiring a hard jet of $p_T > 100$ GeV, computed from single-electron prescaled triggers as a function of electron p_T (left) and leading jet p_T (right). Fake factors for electron p_T 4.5 – 5 GeV are taken to be the same as electron p_T 5 – 6 GeV. A red line denotes the average electron fake factor over all electron p_T of 0.267.

1553

Fig. 8.27,

1554

- fake factors as a function of pile up variables, such as average interaction per bunch crossing and number of primary vertices, are also shown in Fig. 8.28.

1555

The relative uncertainties on the final electron fake factors versus electron p_T are shown in Fig. 8.29.

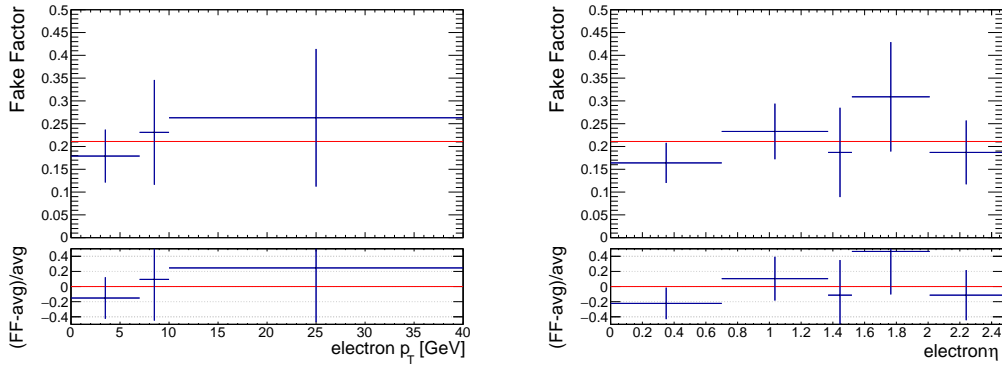


Figure 8.25: Electron fake factors computed from single-electron prescaled triggers as a function of electron p_T (left) and electron η (right) in the kinematic region with leading jet $p_T > 100\text{GeV}$.
Fake factors for electron p_T 4.5 – 5 GeV are taken to be the same as electron p_T 5 – 6 GeV.
A red line denotes the average electron fake factor over all electron p_T of 0.211.

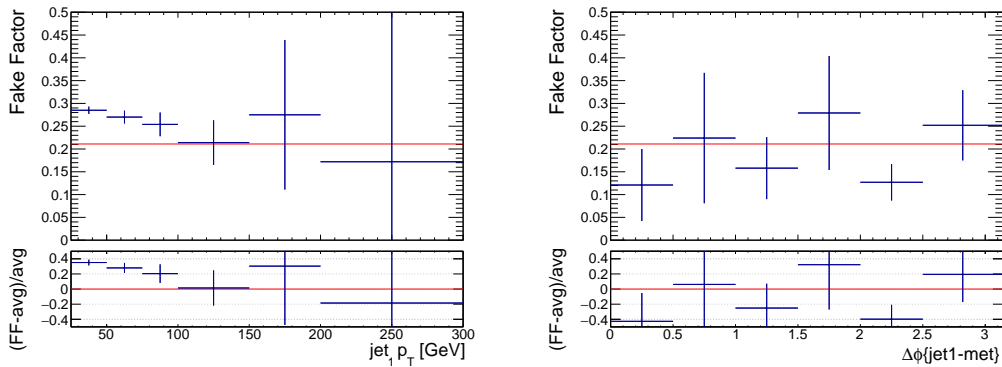


Figure 8.26: Electron fake factors computed from single-electron prescaled triggers as a function of leading jet p_T (left) and $\Delta\phi_{jet-E_T^{\text{miss}}}$ (right). A red line denotes the average electron fake factor over all electron p_T of 0.211.

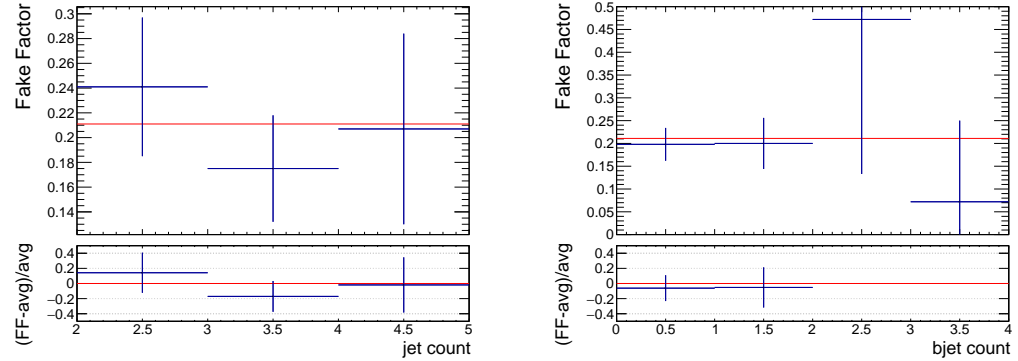


Figure 8.27: Electron fake factors computed from single-electron prescaled triggers as a function of the jet multiplicity (left) and the b -jet multiplicity (right). A red line denotes the average electron fake factor over all electron p_T of 0.211.

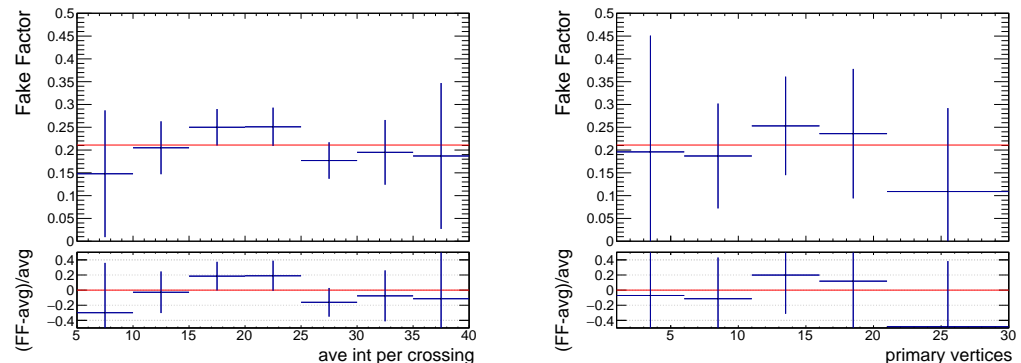


Figure 8.28: Electron fake factors computed from single-electron prescaled triggers as a function of the average interaction per bunch crossing (left) and the number of primary vertices (right). A red line denotes the average electron fake factor over all electron p_T of 0.211.

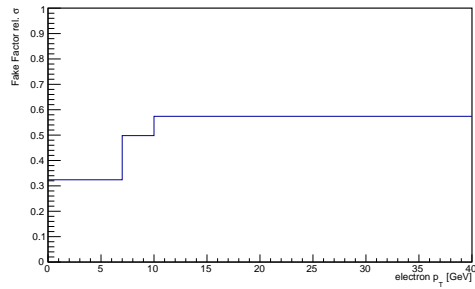


Figure 8.29: Relative uncertainties on electron fake factors binned electron p_T .

1558 **8.4 Conclusion**

1559 This chapter went over a lot of material and I think somehow I have to reiterate
1560 the important points here..

Part III

1561

Analysis and Results

1562

1563 **Chapter 9**

1564 **Systematic Uncertainties**

1565 Systematic uncertainties can be split into two categories: experimental and
1566 theoretical. Sources of experimental uncertainties are particle reconstruction model-
1567 ing in detector simulation, luminosity and pileup measurements, and systematic effects
1568 from data-driven estimates. Theoretical uncertainties emerge from modeling of Stan-
1569 dard Model background processes. Simulation of these processes relies on cross-section
1570 measurements, parton distribution functions employment, and renormalization and fac-
1571 torization scale assumptions. These systematic uncertainties propagate to the final
1572 expected yields of signal to background, and limit the resolution of your predictions.

1573 **Describe how the chapter will flow.**

1574 **9.1 Experimental Uncertainties**

1575 This chapter, the CP group uncertainties will first be overviewed, and next
1576 fake factor uncertainties.

1577 **9.1.1 CP Group Uncertainties**

1578 The list is: Pile-up re-weighting, jets, electrons and muons, missing transverse

1579 energy, luminosity

1580 Multiple pile-up interactions need to be modeled well in Monte Carlo so that

1581 the simulated detector response and particle reconstruction conditions match the actual

1582 data. The distribution of the average number of interactions per bunch crossing applied

1583 to Monte Carlo events, the μ profile is based on relevant assumptions and does not

1584 always agree with the μ profile observed in data. To resolve these disagreements, the

1585 μ profile for Monte Carlo is reweighted to better match the profile in data. This is

1586 typically called pile-up reweighting. Studies of the data/MC agreement for the number

1587 of primary vertices versus μ suggest an additional rescaling of the μ distribution in

1588 data of 1/1.16. A systematic uncertainty for the pile-up reweighting scheme is assigned

1589 by varying the scaling factor assigned to data between 1.00 and 1.21 and assessing the

1590 change in event yields. An uncertainty on the luminosity measurement is also examined.

1591 For the 2015+2016 combined datasets, this is observed as 3.2%.

1592 Uncertainties on the jet energy scale and jet energy resolution are measured.

1593 Five parameters were varied up and down for the energy uncertainty estimate, and

1594 one parameter was varied for the uncertainty on the resolution. Also must assign an

1595 uncertainty to account for the differences in the jet-vertex tagging and b-jet tagging

1596 efficiencies between Monte Carlo and data. Uncertainties on the electron energy and

1597 momentum scale and resolution must also be considered, as well as the uncertainties on

1598 the electron and muon scale factors applied to Monte Carlo events to ensure the simu-
1599 lated reconstruction, identification, isolation and track-to-vertex association efficiencies
1600 match the data. Furthermore, uncertainties on the missing transverse arise from the
1601 propagation of error in the transverse momentum measurements of hard physics ob-
1602 jects. Additional uncertainties on the E_T^{miss} propagate from the scale and resolution of
1603 the track-based soft term, described in Chapter 5.2.

1604 Dominant systematic is from the jet energy scale and resolution. **Give a quan-**
1605 **titative summary if you can.**

1606 9.1.2 Fake Factor Uncertainties

1607 Fake and non-prompt lepton backgrounds are estimated with a data-driven
1608 fake factor method, as described in Chapter 8, and uncertainties arise from several
1609 sources. The list is: statistical uncertainties on the applied fake factors, prompt sub-
1610 traction, kinematic dependencies, non-closure in the same-sign validation region.

1611 Statistical uncertainties on the fake factors themselves are due to the limited
1612 size of the samples used to derive the fake factors. These samples use pre-scaled single
1613 lepton triggers to select events in data, which are further scrutinized based on the iden-
1614 tification, isolation, and impact parameter of the reconstructed leptons and determined
1615 to be either an "ID" or "anti-ID" lepton event. It is possible that there are overlapping
1616 events in these two categories, but it is a rare occurrence since less than 10% of the events
1617 have more than one lepton, and both the "ID" and the "anti-ID" lepton would need to
1618 fall in the same p_T range accepted depending in which trigger was fired. **Refer to the**

1619 plots that show the extent of the statistical error on the fake factors and try to give
1620 some quantitative summary.

1621 Fake factors are measured then applied in regions of data that are enriched
1622 in events with fakes, and depleted in events with true, prompt leptons, but there are
1623 still contribution from prompt leptons in these regions. In the fake factor measurement
1624 region, the prompt contribution is subtracted from the distributions in which the fake
1625 factors are measured using Standard Model Monte Carlo events that have been rescaled
1626 to match anti-ID lepton events in data in the high E_T^{miss} region. To calculate the
1627 systematic uncertainty on this method of prompt subtraction, the change in the binned
1628 fake factors is studied as three key parameters are varied. The E_T^{miss} region, where the
1629 scale factor for the prompt subtraction is computed, is varied up and down 20 GeV
1630 from the nominal $E_T^{\text{miss}} > 200$ GeV selection, the region where the fake factors are
1631 measured is varied up and down by 10 GeV from the nominal $m_T < 40$ GeV selection,
1632 and the scale factor that is applied to the subtracted Monte Carlo is varied up and
1633 down by 20%. Uncertainty contributions in the prompt subtraction is assed further
1634 by recomputing the scale factor and prompt subtraction using the hight m_T region,
1635 $m_T > 100$ GeV ([check this, just guessing here](#)), of anti-ID lepton events. All together,
1636 the resulting uncertainties on both electron and muon scale factors are less than 10%,
1637 but for one exception of the muon p_T bin above 10 GeV, where the uncertainty is 19%.
1638 The overall contribution from prompt subtraction is minuscule compared to the other
1639 sources.

1640 The fake factors are measured as a function of electron p_T for the electrons,

and as a function of muon p_T and N_{b-jet} for the muons. This choice was motivated by the strong kinematic dependencies of the fake factors on these variables, but other, smaller kinematic dependencies are present. These dependencies are not large enough to consider binning the fake factors in every variable, so they are accounted for as a systematic. Refer to the plots all the fake factors in all the different variables. We consider the largest statistically meaningful variation of the fake factors binned in the alternative relevant variables and subtract it from the average fake for the electron and muon samples separately, and the resulting uncertainty is 25% for both, driven by the variation in lepton η .

9.2 Theoretical Uncertainties

Theoretical uncertainties are different for signal and background simulation and arise from the uncertainties on the underlying parameters in the Monte Carlo generation.

9.2.1 Uncertainty on Simulated Signal Events

The initial state radiation in signal processes require next-to-leading order calculations that give rise to systematic uncertainty. This is ISR, the is also FSR and UE (underlying event). ISR/FSR/EU are all around 20%. PDF uncertainties on signal acceptances are also estimated to be around 10%. Uncertainties on signal cross-section are around 5%.

1660 **9.2.2 Uncertainty on Simulated Background Events**

1661 Diboson, $Z(\rightarrow \tau\tau)$ +jets, and $t\bar{t}$ are dominant backgrounds, and uncertainties
1662 on these predictions are estimated using the LHE3 weights [what are these?](#) available
1663 in the derivations. There are three main sources of uncertainty: choice of QCD renor-
1664 malization and factorization scales, μ_R and μ_F , choice of strong coupling constant, α_s ,
1665 and choice of PDF set. μ_R and μ_F are varied up and down by a factor of 2, α_s is
1666 varied within its uncertainty ([which is?](#)), variations within acceptance with the respect
1667 to MMHT2014, CT14, NNPDF PDF sets is symmetrized, and the envelope is taken to
1668 be the uncertainty. The impact is evaluated directly on the predicted yield from each
1669 of the dominant background processes in the signal, control, validation regions, or bins
1670 within where they contribute the most (SR-MLL, SR-MT2, CR-top $t\bar{t}$ only, CR-tau,
1671 VRDF-MLL, VRDF-MT2, VR-VV. For each region/bin, the final uncertainty is equal
1672 to the quadrature addition of all the individual contributions.

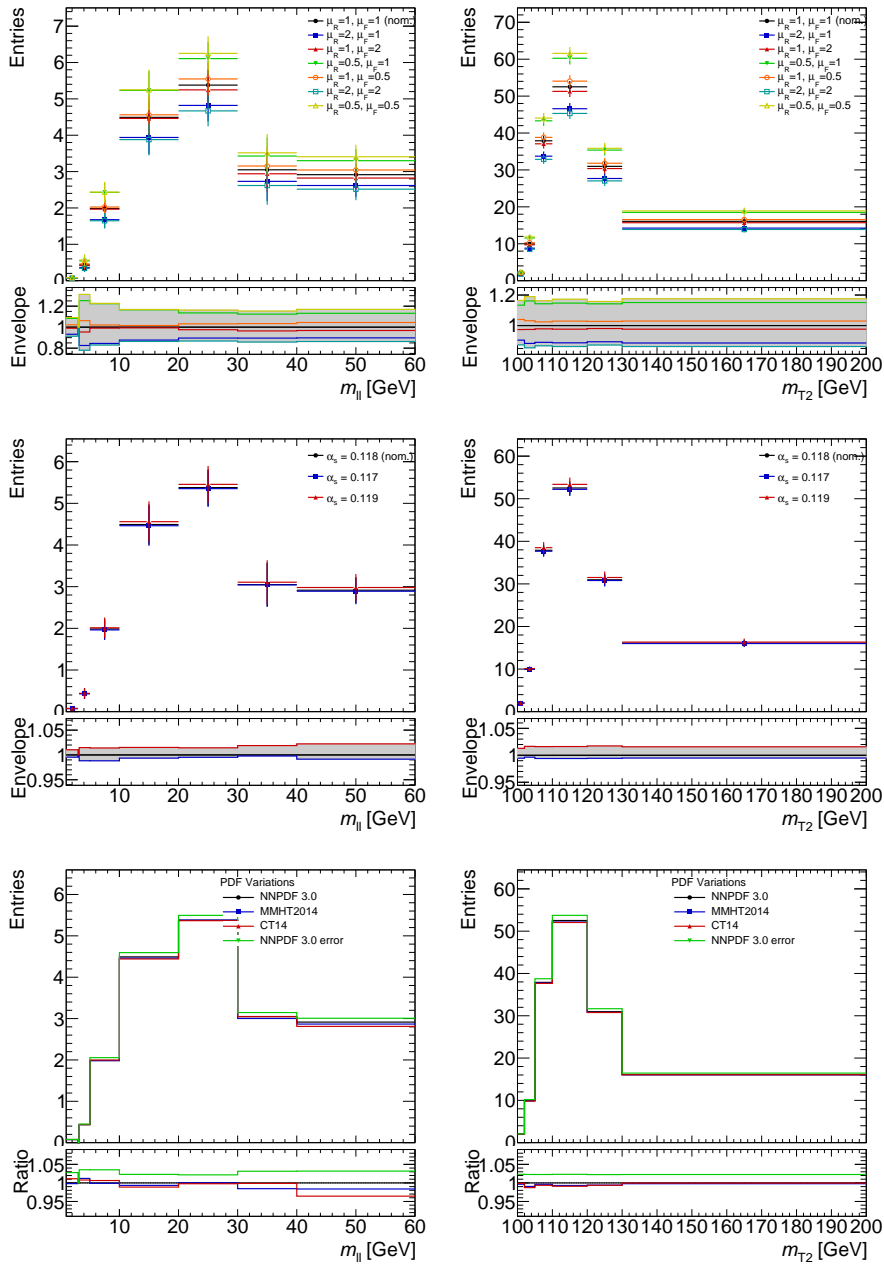


Figure 9.1: QCD scale, α_s and PDF uncertainties on the shape and normalization of the diboson background in the Higgsino and slepton signal regions (with no lepton flavor requirement).

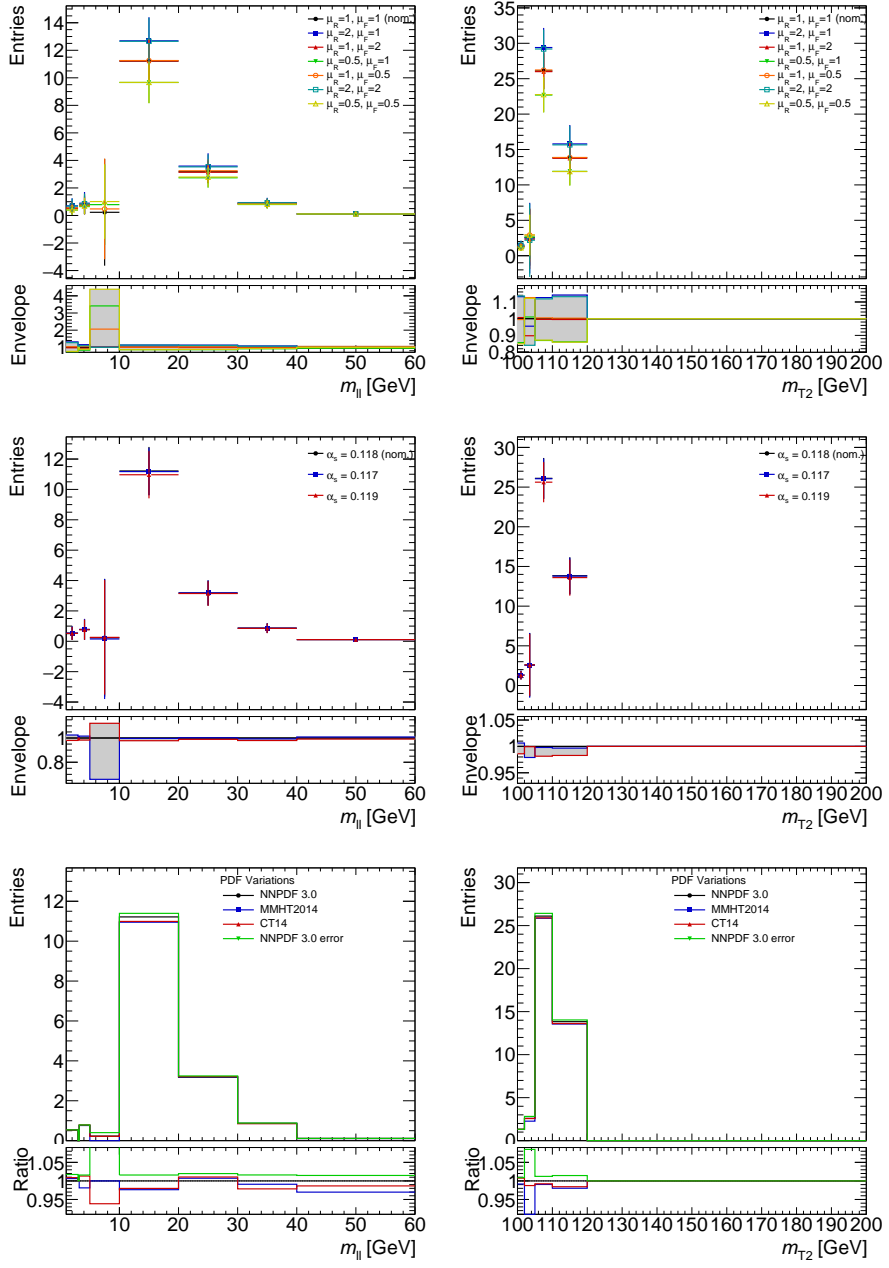


Figure 9.2: QCD scale, α_s and PDF uncertainties on the shape and normalization of the $Z \rightarrow \tau\tau$ background in the Higgsino and slepton signal regions (with no lepton flavor requirement).

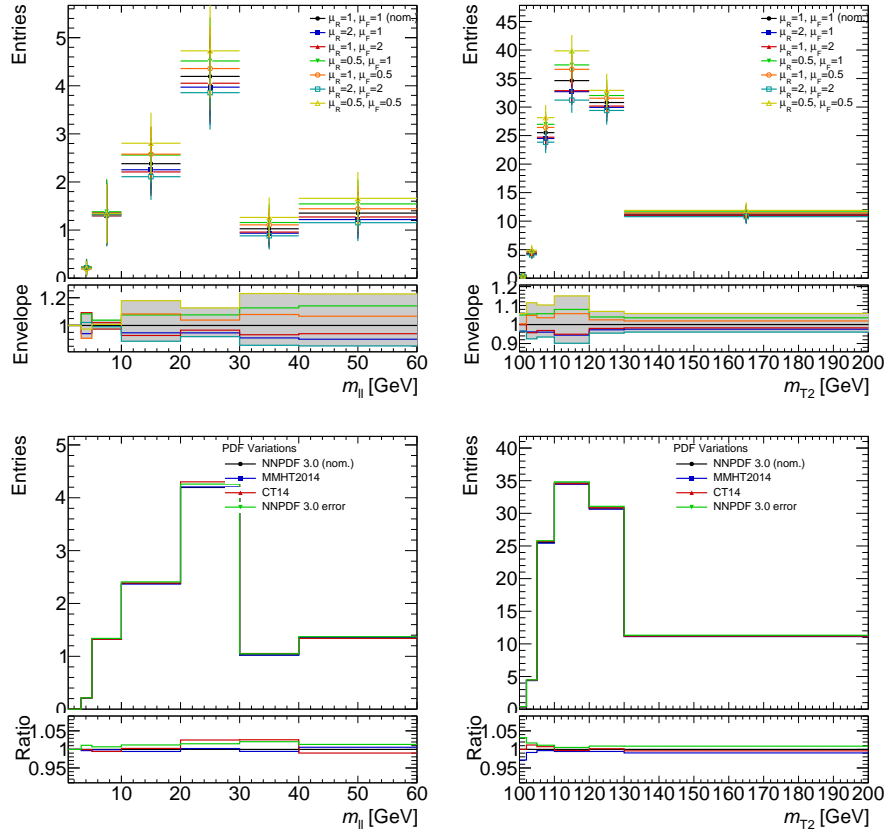


Figure 9.3: QCD scale and PDF uncertainties on the shape and normalization of the $t\bar{t}$ background in the Higgsino and slepton signal regions (with no lepton flavour requirement).

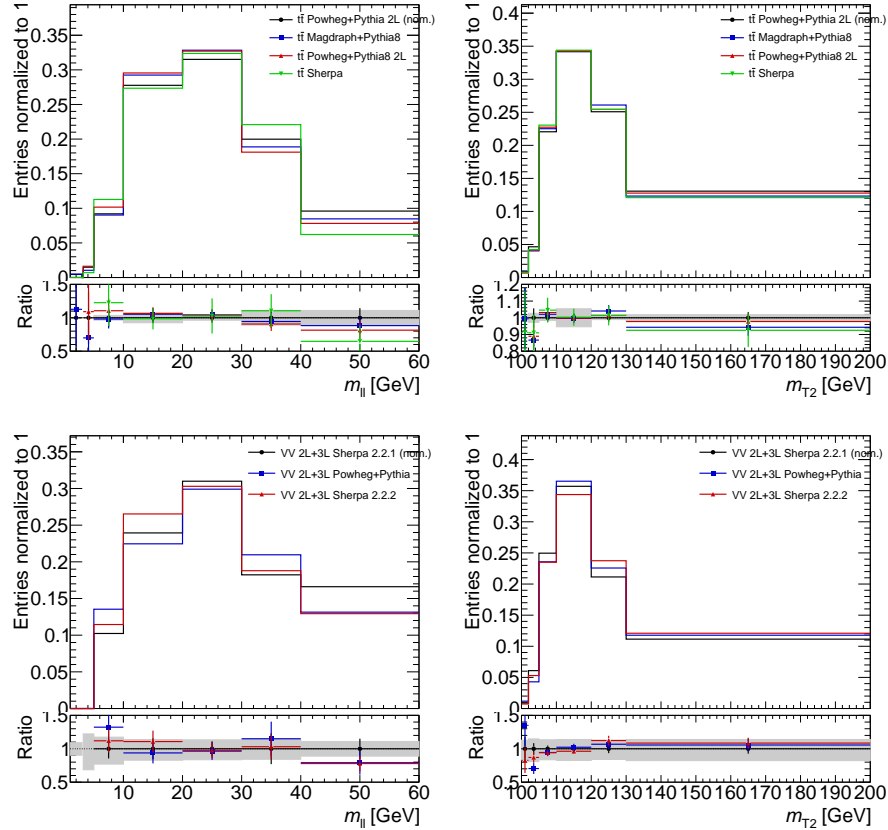


Figure 9.4: Comparison of the $m_{\ell\ell}$ (left) and m_{T2} (right) shapes predicted by different $t\bar{t}$ (top) and VV (bottom) MC generators, in the Higgsino and slepton signal regions. All distributions are normalized to the same number of entries. The gray band displayed in the ratio pad under each distribution represents the modeling uncertainty assigned to each background in each of the bins.

1673 Chapter 10

1674 Statistical Analysis

1675 **Say something here first about the fits** The model dependent analysis is per-

1676 formed by a shape fit of signal to background in the $m_{\ell\ell}$ and m_{T2} distributions. A

1677 channel object can represent a SR, CR, or VR, and channels are defined as the separate

1678 bins within them. The definition of an SR, signal region, and a CR, control region, was

1679 given in the beginning of Chapter 6. A *validation region* (VR) is a region in kinematic

1680 phase space designed to validate the model used to predict the background contribution

1681 to the SRs in data. It is defined in a way that maximizes the region's statistical sig-

1682 nificance while minimizing its signal contamination. Kinematically positioned between

1683 the CR and the SR, it should also help mediate the assumptions made in the CR to SR

1684 extrapolation. The extrapolation happens in variables chosen to separate the regions

1685 and the bins within them. Keeping the SRs and CR statistically independent means

1686 they can be described by different probability density functions and can be combined

1687 into a simultaneous fit. The statistical combination of multiple channels is based on

1688 a profile likelihood method implemented in the HistFitter package that builds proba-
 1689 bility density functions, fits them to data, and interprets them with statistical tests.
 1690 In this method, a likelihood is constructed as the product of the Poisson probability
 1691 distributions that describe the total number of events observed in each channel. The
 1692 mean is taken as the nominal MC yield in a given region and systematic uncertainties
 1693 are treated as nuisance parameters in the fit.

1694 **10.1 Test Statistics and p-values**

1695 The test statistic that provides the most powerful test is the likelihood ratio
 1696 function, given by Equation 10.1.

$$L(\mu, \vec{\theta}) = \prod_c \prod_i Pois(n_{ci}^{obs} | n_{ci}^{sig}(\mu\vec{\theta}) + n_{ci}^{bkg}(\vec{\theta})) \prod_k f_k(\theta'_k | \theta_k) \quad (10.1)$$

1697 In Equation 10.1, μ and $\vec{\theta}$ represent the signal strength and the set of nuisance param-
 1698 eters. The values of these parameters that maximize $L(\mu, \vec{\theta})$, or equivalently, minimize
 1699 $-\ln L(\mu, \vec{\theta})$ are called maximum likelihood estimates (MLEs) and denoted as $\hat{\mu}$ and $\hat{\vec{\theta}}$.
 1700 There is also a conditional maximum likelihood estimate, $\hat{\vec{\theta}}^*$, which is the value of $\vec{\theta}$ that
 1701 maximizes $L(\mu, \vec{\theta})$ for a fixed μ . These are all used with the likelihood function $L(\mu, \vec{\theta})$
 1702 to construct the profile likelihood ratio:

$$\lambda(\mu) = \left(\frac{L(\mu, \hat{\vec{\theta}}(\mu))}{L(\hat{\mu}, \hat{\vec{\theta}})} \right) \quad (10.2)$$

1703 In a physical theory, the true signal strength μ is a non-negative value, and a negative
 1704 value of $\hat{\mu}$ implies a shortage of signal-like events in the background. The boundary at

1705 $\mu = 0$ convolutes the asymptotic distributions in $\lambda(\mu)$, so μ is free to occupy positive

1706 and negative values while the full profile likelihood ratio is defined as:

$$\tilde{\lambda}(\mu) = \begin{cases} \frac{L(\mu, \hat{\theta}(\mu))}{L(\hat{\mu}, \hat{\theta})} & \hat{\mu} \geq 0 \\ \frac{L(\mu, \hat{\theta}(\mu))}{L(0, \hat{\theta}(0))} & \hat{\mu} < 0 \end{cases} \quad (10.3)$$

1707 As stated before, maximizing the likelihood is equivalent to minimizing the negative-

1708 log likelihood, which is more convenient for visualization. The test statistic \tilde{q} is defined

1709 separately for discovery and limit-setting using the negative-log likelihood ratio (NLLR).

1710 For discovery, the test statistic \tilde{q}_0 is built to distinguish the background only

1711 hypothesis $\mu = 0$ from the alternative hypothesis $\mu > 0$, where there is an excess above

1712 background. When the MLE $\hat{\mu}$ is positive, the test statistic is the NLLR, otherwise it

1713 is zero, as shown in Equation 10.4.

$$\tilde{q}_0 = \begin{cases} -2 \ln \lambda(\mu) & \hat{\mu} > 0 \\ 0 & \hat{\mu} \leq 0 \end{cases} \quad (10.4)$$

1714 When setting limits, the test statistic \tilde{q}_μ is meant to distinguish the signal

1715 hypothesis, where signal events are produced above background at some rate μ , from

1716 the alternative hypothesis with signal events produced at some rate less than or equal

1717 to μ . In this case, when the MLE $\hat{\mu}$ is less than μ , \tilde{q}_μ equals the NLLR, otherwise, it is

1718 set to zero. This is shown in Equation 10.5

$$\tilde{q}_\mu = \begin{cases} -2 \ln \lambda(\mu) & \hat{\mu} \leq \mu \\ 0 & \hat{\mu} > \mu \end{cases} \quad (10.5)$$

1719 Through the test statistic, the data is mapped to a single real-valued number
 1720 that represents the outcome of the experiment. If the experiment was performed many
 1721 times, the test profile likelihood ratio function would output a different value each time,
 1722 making a distribution of real-valued discriminating variables. In practice, Monte Carlo
 1723 simulation *get the right language here, talk about throwing the toys and such* is used
 1724 to generate numerous pseudo experiments, and while the test statistic \tilde{q} is a function
 1725 of μ , the distribution of \tilde{q} becomes explicitly a function of the nuisance parameters $\vec{\theta}$,
 1726 denoted as $f(\tilde{q}|\mu, \vec{\theta})$. The p-value for any given hypothesis represents the probability to
 1727 observe an equal or more extreme outcome given that hypothesis as the integral of the
 1728 test statistic distribution from $\tilde{q}_{\mu,obs}$ to ∞ .

$$p_{\mu, \vec{\theta}} = \int_{\tilde{q}_{\mu,obs}}^{\infty} f(\tilde{q}_\mu | \mu, \vec{\theta}) d\tilde{q}_\mu \quad (10.6)$$

1729 Conventionally in high energy particle physics experiments, a standard one-
 1730 sided frequentist confidence interval defines an upper limit on the parameter of interest
 1731 at 95% confidence level. The p-value can be used to measure how well the data agrees
 1732 with a signal hypothesis of signal strength μ , given in Equation 10.7, or it can be
 1733 used to measure how consistent the data is with the background only hypothesis, as in
 1734 Equation 10.8.

$$p_\mu = \int_{\tilde{q}_{\mu,obs}}^{\infty} f(\tilde{q}_\mu | \mu, \hat{\vec{\theta}}(\mu, obs)) d\tilde{q}_\mu \quad (10.7)$$

$$p_b = 1 - \int_{\tilde{q}_{\mu,obs}}^{\infty} f(\tilde{q}_\mu | 0, \hat{\vec{\theta}}(\mu = 0, obs)) d\tilde{q}_\mu \quad (10.8)$$

1735 1736 The CL_s upper limit on μ comes from solving as a function of μ for $p'_\mu = 0.05$, where

¹⁷³⁷ p'_μ is the ratio of p-values in Equation ??.

$$p'_\mu = \frac{p_\mu}{1 - p_b} \quad (10.9)$$

¹⁷³⁸ Confidence intervals will come up again in Chapter 11 when the actual model
¹⁷³⁹ interpretations are discussed.

¹⁷⁴⁰ **10.2 Fit and Nuisance Parameter Pull**

¹⁷⁴¹ The relative changes in the nuisance parameters and the fit are often referred
¹⁷⁴² to as the 'pull'. An example of the fit and nuisance parameter pulls are shown in
¹⁷⁴³ Figure ??..

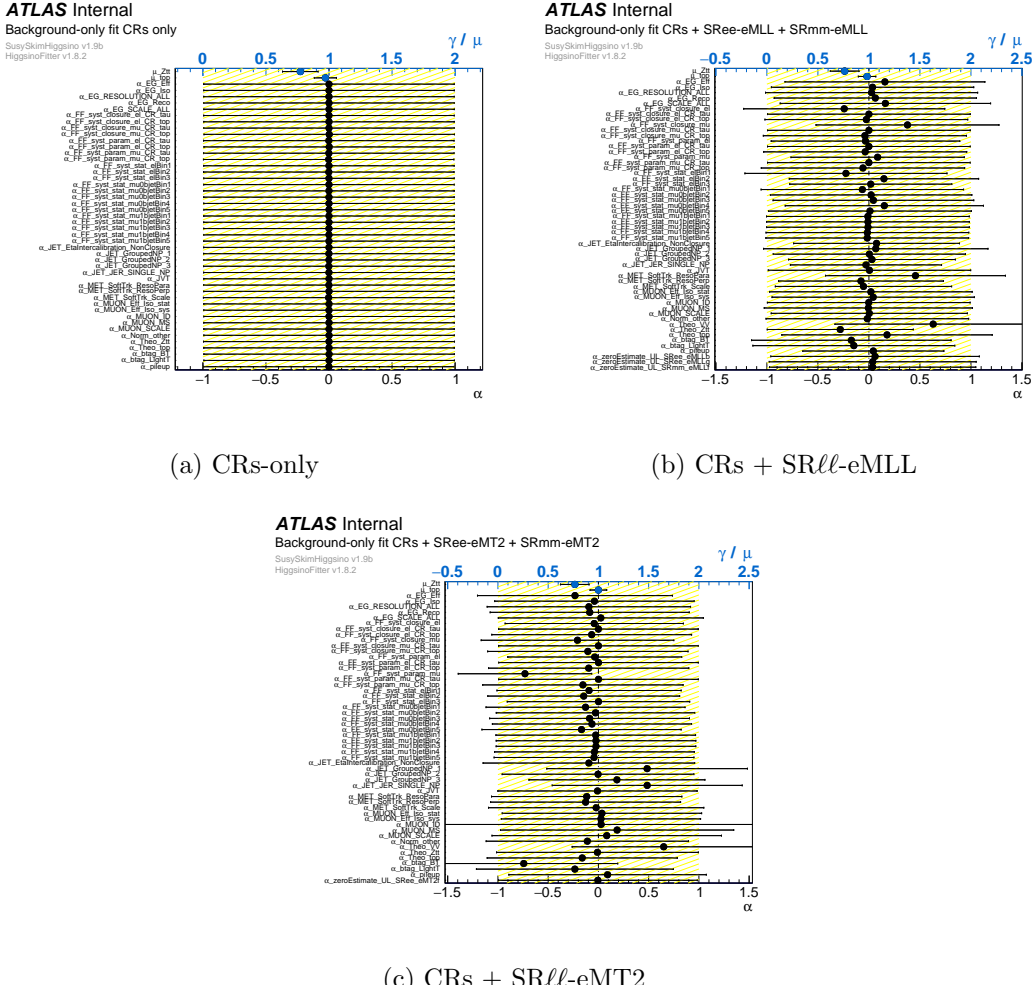


Figure 10.1: Fit parameters for background-only fit in various configurations of the regions allowed to be treated as constraining.

1744 **Chapter 11**

1745 **Results**

1746 **11.1 Background Only Fit**

1747 In the background only fit, only the CRs are used to constrain the fit pa-
1748 rameters by maximizing the likelihood function assuming there are no signal events in
1749 the CRs. In this way, the SM background predictions are independent of the signal
1750 regions. The factors μ_{top} and $\mu_{\tau\tau}$, used to normalize of the combined t , tW , and $t\bar{t}$
1751 samples and the $Z(\rightarrow \tau\tau)$ +jets samples, are obtained in a simultaneous fit to data in
1752 CR-top and CR-tau. For exclusion, two simultaneous shape fits are performed across
1753 ee and $\mu\mu$ channels, one in the $m_{\ell\ell}$ variable, and the other in the m_{T2}^{100} variable. The
1754 normalization parameters μ_{top} and $\mu_{\tau\tau}$ for the background only fit are $\mu_{top} = 0.72 \pm 0.13$
1755 and $\mu_{\tau\tau} = 1.02 \pm 0.09$, where the uncertainty is the combination of the statistical and
1756 systematic contributions.

1757 The accuracy of the background predictions is tested in the validation regions

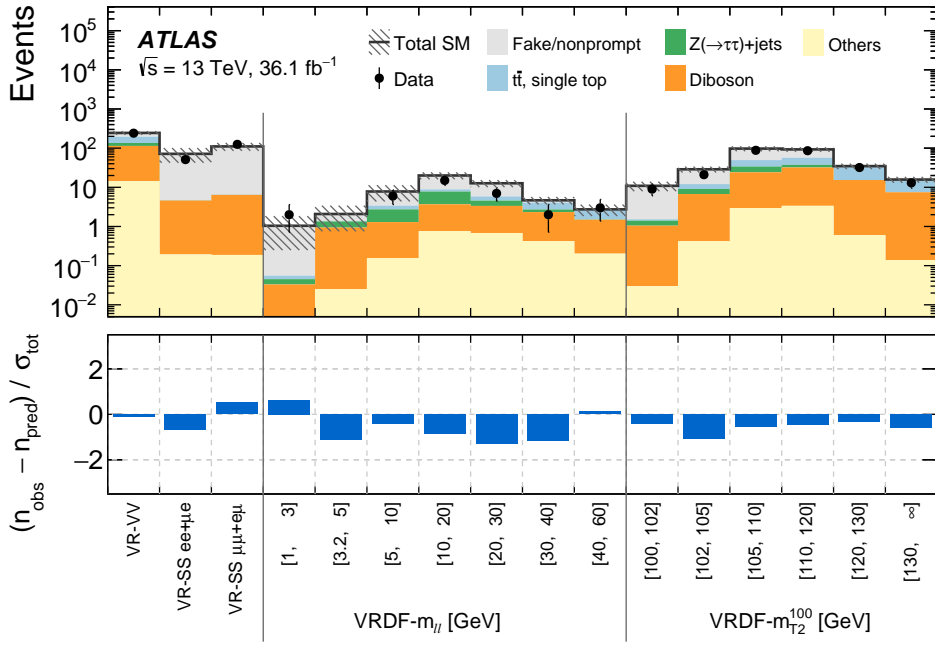


Figure 11.1: Summary of Monte Carlo yields in control, validation and signal regions in a background-only fit using data only in the two CRs to constrain the fit.

and, as shown in Figure 11.1, are consistently within 1.5 standard deviations of the observed data yields. [Talk about this plot.](#) Figure 11.2 shows distributions of the data and expected backgrounds for a selection of VRs and kinematic variables, including the $m_{\ell\ell}$ distribution in VR-VV and the m_{T2} distribution in VR-SS. Data and background predictions are compatible within uncertainties.. Figure 11.3 shows kinematic distributions of data and expected backgrounds in the inclusive Higgsino and slepton signal regions. No significant excesses above expected backgrounds are observed.

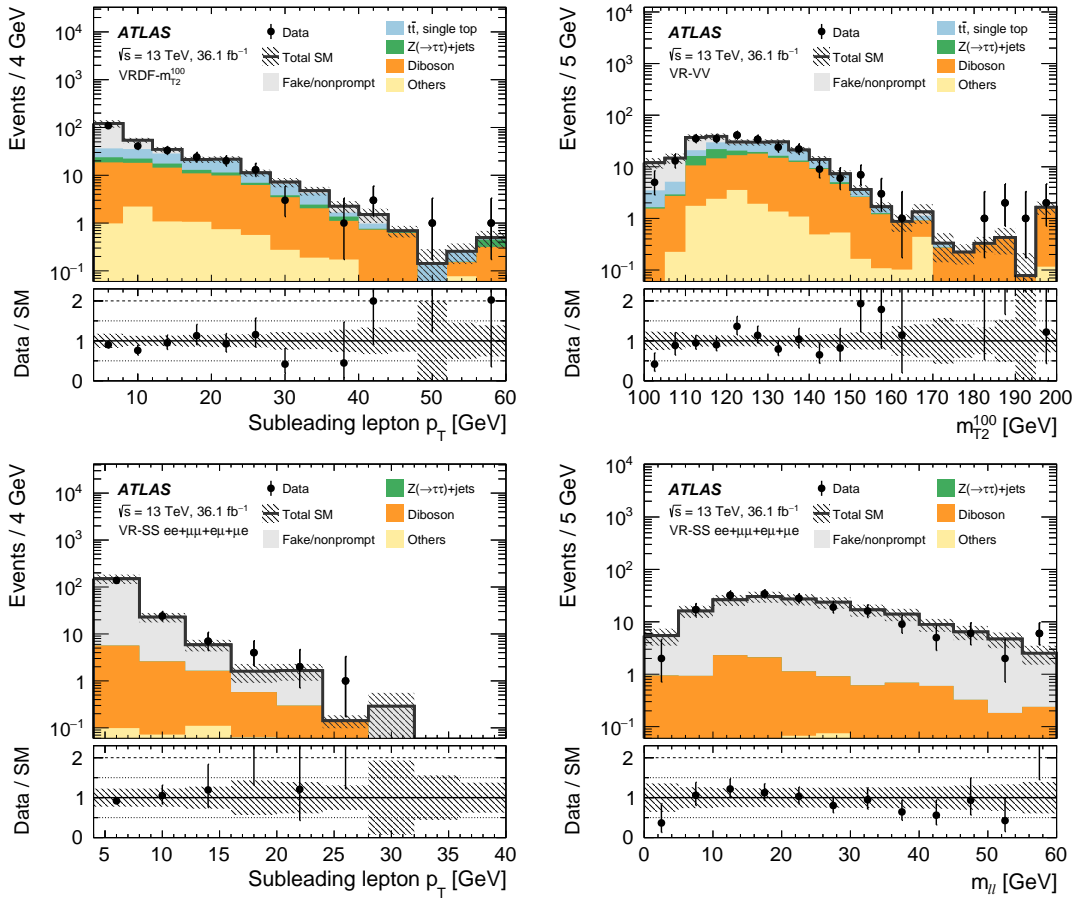


Figure 11.2: Kinematic distributions after the background-only fit showing the data and the expected background in the different-flavor validation region $\text{VRDF-}m_{\text{T2}}^{100}$ (top left), the diboson validation region VR-VV (top right), and the same-sign validation region VR-SS inclusive of lepton flavor (bottom). Similar levels of agreement are observed in other kinematic distributions for VR-SS and VR-VV . Background processes containing fewer than two prompt leptons are categorized as ‘Fake/nonprompt’. The category ‘Others’ contains rare backgrounds from triboson, Higgs boson, and the remaining top-quark production processes listed in Table. The last bin includes overflow. The uncertainty bands plotted include all statistical and systematic uncertainties. Orange arrows in the Data/SM panel indicate values that are beyond the y-axis range.

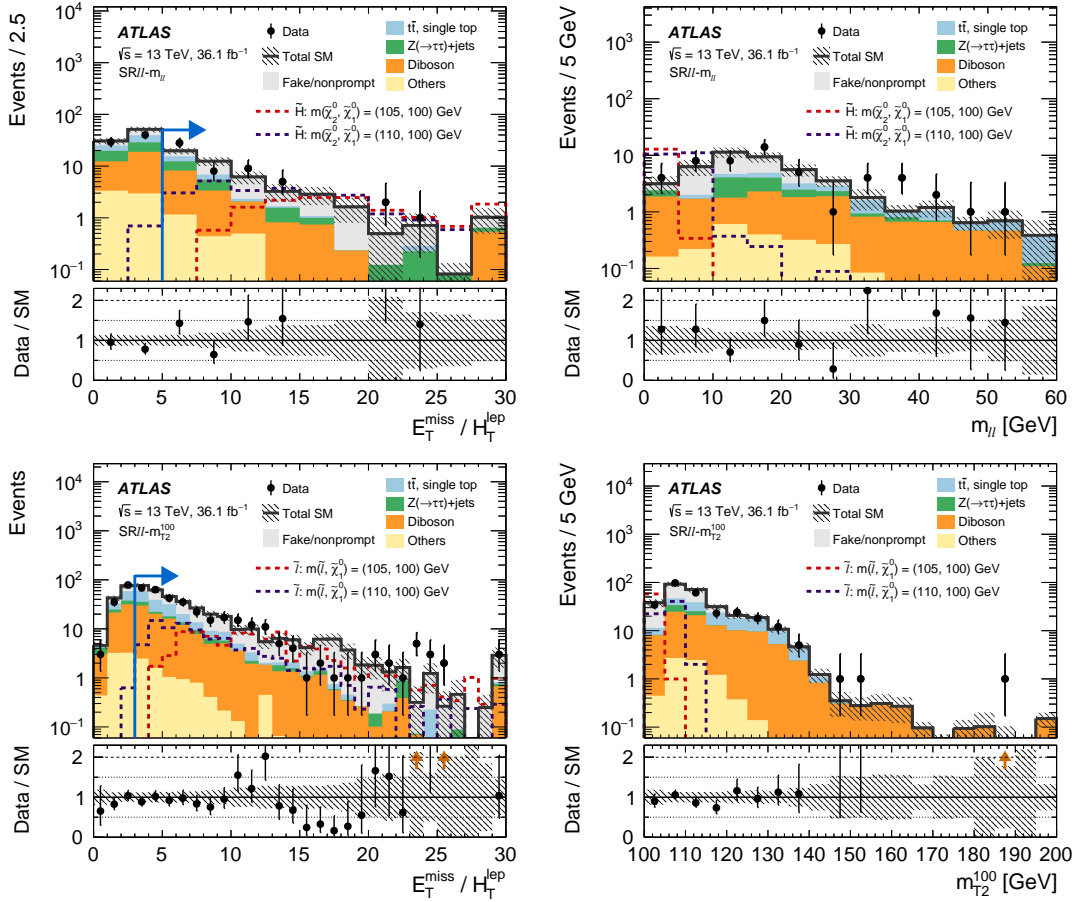


Figure 11.3: Kinematic distributions after the background-only fit showing the data as well as the expected background in the inclusive electroweakino $\text{SR}\ell\ell-m_{\ell\ell}$ [1, 60] (top) and slepton

1765 **11.2 Model Independent Upper Limits on New Physics**

1766 Model independent limits are useful so that, for any signal model of interest,
1767 one can evaluate the number of events predicted in a signal region and check if the model
1768 is excluded by current measurements. For this, single-binned inclusive SRs are used,
1769 since binning in the SRs requires some model-based assumptions about the distribution
1770 of the signal over these bins. An upper limit on the number of observed (S_{obs}^{95}) and
1771 expected (S_{exp}^{95}) signal events in each SR at 95% CL is procured in the same way as
1772 the background only fit, but now using CRs and SRs and with the observed number of
1773 events in a signal region given as inputs to the fit. The observed and predicted event
1774 yields are used to set the upper limits by including one inclusive signal region at a time
1775 in a simultaneous fit with the CRs. The profile-likelihood hypothesis test performed to
1776 get the upper limits uses the background estimates obtained from the background only
1777 test in the CRs and SRs, and both the expected and observed upper limits use the same
1778 background estimates. In this way, the expected upper limits inadvertently depend on
1779 the observed data. **Talk to Mike about the signal strength parameter being set to 1**
1780 **or 0.. talk to him about the mathematical formalism in general.** Add something about
1781 the signal contamination in the CRs is assumed to be none.

1782 Refer to **Table 11.1**. An upper limit on the visible cross-section for new physics
1783 in a given SR, $\langle\epsilon\sigma\rangle_{obs}^{95}$ [fb], is equal to product of the signal region acceptance, the re-
1784 construction efficiency, and the production cross-section. The discovery p-value, $p(s=0)$
1785 in the right most column of the table, represents the significance of an excess of events

1786 in a signal region by considering the probability that the backgrounds in a SR are more
1787 signal-like than observed.

1788 11.3 Model Dependent Sensitivity with Shape Fit

1789 Here we assume the Higgsino and slepton signals give rise to the $m_{\ell\ell}$ and
1790 M_{T2} distributions in our signal regions. This consideration provides better constraining
1791 power for these models over the model independent upper limits of the 'Discovery' fit.
1792 Like in the model independent case, the fit is performed on the CRs and SRs simulta-
1793 neously, but different from the model independent case, the multi-binned exclusive SRs
1794 and considered. Say something about the binning in signal sensitive observables $m_{\ell\ell}$
1795 and M_{T2} . Background and signal samples are included in both the CR and SR fits
1796 to account for any signal contamination in the CRs.

1797 Refer to Tables 12.1 and 12.2.

Table 11.1: Left to right: The first two columns present observed (N_{obs}) and expected (N_{exp}) event yields in the inclusive signal regions. The latter are obtained by the background-only fit of the control regions, and the errors include both statistical and systematic uncertainties. The next two columns show the observed 95% CL upper limits on the visible cross-section ($\langle \epsilon\sigma \rangle_{\text{obs}}^{95}$) and on the number of signal events (S_{obs}^{95}). The fifth column (S_{exp}^{95}) shows what the 95% CL upper limit on the number of signal events would be, given an observed number of events equal to the expected number (and $\pm 1\sigma$ deviations from the expectation) of background events. The last column indicates the discovery p -value ($p(s = 0)$), which is capped at 0.5.

Signal Region	N_{obs}	N_{exp}	$\langle \epsilon\sigma \rangle_{\text{obs}}^{95} [\text{fb}]$	S_{obs}^{95}	S_{exp}^{95}	$p(s = 0)$
SR $\ell\ell$ - $m_{\ell\ell}$ [1, 3]	1	1.7 ± 0.9	0.10	3.8	$4.3_{-0.7}^{+1.7}$	0.50
SR $\ell\ell$ - $m_{\ell\ell}$ [1, 5]	4	3.1 ± 1.2	0.18	6.6	$5.6_{-1.0}^{+2.3}$	0.32
SR $\ell\ell$ - $m_{\ell\ell}$ [1, 10]	12	8.9 ± 2.5	0.34	12.3	$9.6_{-1.9}^{+3.2}$	0.21
SR $\ell\ell$ - $m_{\ell\ell}$ [1, 20]	34	29 ± 6	0.61	22	17_{-6}^{+7}	0.25
SR $\ell\ell$ - $m_{\ell\ell}$ [1, 30]	40	38 ± 6	0.59	21	20_{-5}^{+9}	0.38
SR $\ell\ell$ - $m_{\ell\ell}$ [1, 40]	48	41 ± 7	0.72	26	20_{-5}^{+8}	0.20
SR $\ell\ell$ - $m_{\ell\ell}$ [1, 60]	52	43 ± 7	0.80	29	24_{-10}^{+5}	0.18
SR $\ell\ell$ - m_{T2}^{100} [100, 102]	8	12.4 ± 3.1	0.18	7	9_{-2}^{+4}	0.50
SR $\ell\ell$ - m_{T2}^{100} [100, 105]	34	38 ± 7	0.49	18	23_{-7}^{+7}	0.50
SR $\ell\ell$ - m_{T2}^{100} [100, 110]	131	129 ± 18	1.3	48	47_{-15}^{+13}	0.37
SR $\ell\ell$ - m_{T2}^{100} [100, 120]	215	232 ± 29	1.4	52	62_{-15}^{+21}	0.50
SR $\ell\ell$ - m_{T2}^{100} [100, 130]	257	271 ± 32	1.7	61	69_{-17}^{+22}	0.50
SR $\ell\ell$ - m_{T2}^{100} [100, ∞]	277	289 ± 33	1.8	66	72_{-17}^{+24}	0.50

1798 **Chapter 12**

1799 **Interpretations**

1800 In absence of any significant excesses over backgrounds, the results are inter-
1801 preted as constraints on the SUSY models presented in Chapter ?? using the exclusive,
1802 multi-binned Higgsino and slepton signal regions. The background only fit is extended
1803 to allow for a signal model with a corresponding signal strength parameter in a simul-
1804 taneous fit of all CRs and relevant SRs, this is referred to as the exclusion fit. I can say
1805 it better than this. In the previous chapter, background-level estimates obtained from
1806 a background-only fit in the CRs only were presented. When electroweakino simplified
1807 models are assumed, the results are interpreted in the 14 exclusive Higgsino signal re-
1808 gions, binned in $m_{\ell\ell}$ and split evenly between the ee and $\mu\mu$ channels. By statistically
1809 combining these signal regions, the signal shape of the $m_{\ell\ell}$ spectrum can be exploited
1810 to improve the sensitivity. When slepton simplified models are assumed, the results are
1811 interpreted in 12 slepton signal regions, binned in $m_{T2^{100}}$ with 6 SRs the ee -channel and
1812 6 in the $\mu\mu$ channel are used for the fit.

1813 Table 12.1 summarizes the observed event yields in the exclusive electroweakino
1814 signal regions, and Table 12.2 summarizes the observed event yields in the exclusive slep-
1815 ton signal regions after the fit is performed using an exclusion fit configuration where
1816 the signal strength parameter is set to zero. Extending the background only fit to in-
1817 clude the signal regions further constrains the background contributions in the absence
1818 of any signal, therefore these predicted yields differ slightly compared to those obtained
1819 with the background only fit. Figure 12.1 demonstrates the harmony between the fitted
1820 and observed yields in these signal regions. No significant contrast between the fitted
1821 background estimates and the observed event yields are observed in any of the exclusive
1822 signal regions.

Table 12.1: Observed event yields and exclusion fit results with the signal strength parameter set to zero for the exclusive electroweakino and slepton signal regions. Background processes containing fewer than two prompt leptons are categorized as ‘Fake/nonprompt’. The category ‘Others’ contains rare backgrounds from triboson, Higgs boson, and the remaining top-quark production processes listed in Table ???. Uncertainties in the fitted background estimates combine statistical and systematic uncertainties.

SRee-$m_{\ell\ell}$	[1, 3]	[3.2, 5]	[5, 10]	[10, 20]	[20, 30]	[30, 40]	[40, 60]
Obs Evts	0	1	1	10	4	6	2
Exp SM Evts	$0.01^{+0.11}_{-0.01}$	$0.6^{+0.7}_{-0.6}$	2.4 ± 1.0	8.3 ± 1.6	4.0 ± 1.0	2.4 ± 0.6	1.4 ± 0.5
Fakes	$0.00^{+0.08}_{-0.00}$	$0.02^{+0.12}_{-0.02}$	1.4 ± 0.9	4.0 ± 1.5	1.6 ± 0.9	0.7 ± 0.6	$0.02^{+0.11}_{-0.02}$
Diboson	$0.007^{+0.014}_{-0.007}$	$0.28^{+0.29}_{-0.28}$	0.51 ± 0.28	1.9 ± 0.6	1.36 ± 0.31	0.72 ± 0.22	0.80 ± 0.28
$Z(\rightarrow \tau\tau) + \text{jets}$	$0.000^{+0.007}_{-0.000}$	$0.3^{+0.8}_{-0.3}$	$0.3^{+0.5}_{-0.3}$	1.7 ± 0.7	$0.25^{+0.26}_{-0.25}$	0.20 ± 0.18	$0.04^{+0.28}_{-0.04}$
$t\bar{t}$, single top	$0.00^{+0.08}_{-0.00}$	$0.02^{+0.12}_{-0.02}$	$0.11^{+0.14}_{-0.11}$	0.44 ± 0.29	0.63 ± 0.35	0.7 ± 0.4	0.6 ± 0.4
Others	$0.002^{+0.015}_{-0.002}$	$0.012^{+0.013}_{-0.012}$	0.12 ± 0.11	0.25 ± 0.16	0.21 ± 0.12	$0.05^{+0.06}_{-0.05}$	$0.0018^{+0.0033}_{-0.0018}$

SR$\mu\mu-m_{\ell\ell}$	[1, 3] GeV	[3.2, 5] GeV	[5, 10] GeV	[10, 20] GeV	[20, 30] GeV	[30, 40] GeV	[40, 60] GeV
Obs Evts	1	2	7	12	2	2	2
Exp SM Evts	1.1 ± 0.6	1.3 ± 0.6	4.9 ± 1.3	13.1 ± 2.2	4.2 ± 1.0	1.4 ± 0.6	1.6 ± 0.6
Fakes	$0.00^{+0.33}_{-0.00}$	$0.4^{+0.5}_{-0.4}$	3.0 ± 1.3	7.3 ± 2.1	$0.4^{+0.8}_{-0.4}$	$0.03^{+0.19}_{-0.03}$	$0.0^{+0.5}_{-0.0}$
Diboson	0.9 ± 0.5	0.7 ± 0.4	1.3 ± 0.6	1.4 ± 0.5	1.9 ± 0.4	0.9 ± 0.5	0.97 ± 0.28
$Z(\rightarrow \tau\tau) + \text{jets}$	$0.18^{+0.25}_{-0.18}$	0.13 ± 0.12	$0.3^{+0.5}_{-0.3}$	2.4 ± 0.8	0.7 ± 0.4	$0.001^{+0.011}_{-0.001}$	$0.05^{+0.06}_{-0.05}$
$t\bar{t}$, single top	$0.01^{+0.10}_{-0.01}$	$0.02^{+0.12}_{-0.02}$	0.19 ± 0.13	1.4 ± 0.6	0.8 ± 0.4	0.37 ± 0.21	0.51 ± 0.33
Others	0.047 ± 0.030	$0.07^{+0.09}_{-0.07}$	0.13 ± 0.12	0.7 ± 0.5	0.35 ± 0.20	0.09 ± 0.07	0.020 ± 0.020

Table 12.2: Observed event yields and exclusion fit results with the signal strength parameter set to zero for the exclusive electroweakino and slepton signal regions. Background processes containing fewer than two prompt leptons are categorized as ‘Fake/nonprompt’. The category ‘Others’ contains rare backgrounds from triboson, Higgs boson, and the remaining top-quark production processes listed in Table ???. Uncertainties in the fitted background estimates combine statistical and systematic uncertainties.

SRee-m_{T2}^{100}	[100, 102] GeV	[102, 105] GeV	[105, 110] GeV	[110, 120] GeV	[120, 130] GeV	[130, ∞] GeV
Obs Evts	3	10	37	42	10	7
Exp SM Evts	3.5 ± 1.2	11.0 ± 2.0	33 ± 4	42 ± 4	15.7 ± 2.0	7.5 ± 1.1
Fakes	2.9 ± 1.2	6.8 ± 2.0	13 ± 4	14 ± 4	1.9 ± 1.2	$0.01^{+0.10}_{-0.01}$
Diboson	0.33 ± 0.12	2.3 ± 0.6	8.5 ± 1.6	12.7 ± 2.4	7.4 ± 1.4	4.3 ± 0.9
$Z(\rightarrow \tau\tau) + \text{jets}$	$0.13^{+0.23}_{-0.13}$	0.6 ± 0.4	4.1 ± 1.8	2.9 ± 1.0	$0.00^{+0.08}_{-0.00}$	$0.00^{+0.20}_{-0.00}$
$t\bar{t}$, single top	0.08 ± 0.08	1.2 ± 0.5	6.5 ± 1.6	10.7 ± 2.4	6.3 ± 1.4	3.2 ± 0.9
Others	$0.011^{+0.012}_{-0.011}$	0.17 ± 0.11	0.8 ± 0.4	1.3 ± 0.7	0.14 ± 0.09	0.06 ± 0.04

SR$\mu\mu$-m_{T2}^{100}	[100, 102] GeV	[102, 105] GeV	[105, 110] GeV	[110, 120] GeV	[120, 130] GeV	[130, ∞] GeV
Obs Evts	5	16	60	42	32	13
Exp SM Evts	6.8 ± 1.5	15.0 ± 2.1	57 ± 5	53 ± 4	24.9 ± 2.9	11.0 ± 1.4
Fakes	5.1 ± 1.5	8.2 ± 2.1	26 ± 5	18 ± 4	1.2 ± 0.8	$0.02^{+0.17}_{-0.02}$
Diboson	0.89 ± 0.22	4.1 ± 0.9	14.3 ± 2.2	18.0 ± 2.7	12.9 ± 2.2	5.9 ± 1.1
$Z(\rightarrow \tau\tau) + \text{jets}$	0.31 ± 0.23	$1.0^{+1.3}_{-1.0}$	6.6 ± 1.7	$1.6^{+1.8}_{-1.6}$	$0.03^{+0.25}_{-0.03}$	$0.02^{+0.24}_{-0.02}$
$t\bar{t}$, single top	0.43 ± 0.22	1.4 ± 0.5	8.3 ± 2.2	12.4 ± 2.9	10.5 ± 2.6	5.0 ± 1.3
Others	$0.020^{+0.024}_{-0.020}$	0.24 ± 0.15	1.8 ± 1.0	2.4 ± 1.3	0.35 ± 0.23	0.11 ± 0.07

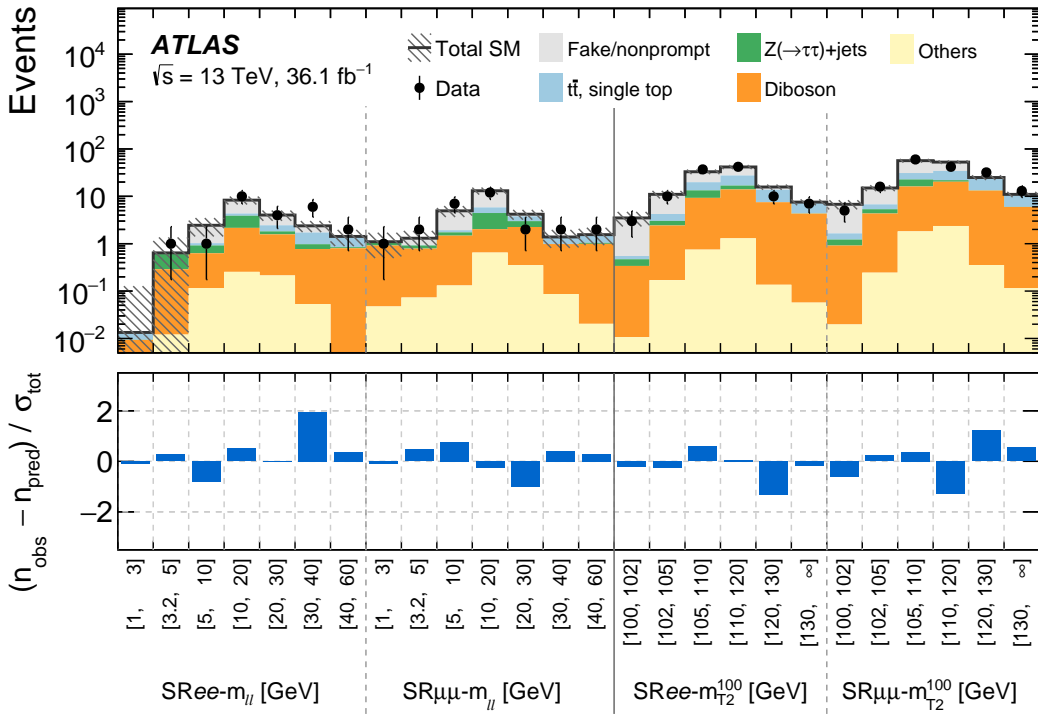


Figure 12.1: Comparison of observed and expected event yields after the exclusion fit with the signal strength parameter set to zero in the exclusive signal regions. Background processes containing fewer than two prompt leptons are categorized as ‘Fake/nonprompt’. The category ‘Others’ contains rare backgrounds from triboson, Higgs boson, and the remaining top-quark production processes listed in Table ???. Uncertainties in the background estimates include both the statistical and systematic uncertainties, where σ_{tot} denotes the total uncertainty.

1823 **12.1 Compressed Higgsino**

1824 Hypothesis tests are performed to set limits on simplified model scenarios us-

1825 ing the CL_s prescription. What is CL_s prescription?. Figure 12.2 shows the 95%

1826 confidence interval limits set on the Higgsino simplified model projected onto the plane

1827 defined by the mass difference between the lightest and next-to-lightest neutralino as

1828 a function of the next-to-lightest neutralino mass. These limits are based on an ex-

1829 clusion fit that exploits the shape of the dilepton invariant mass spectrum from the

1830 exclusive electroweakino signal regions and exclude next-to-lightest neutralino masses

1831 up to 130 GeV for mass splittings between 5 and 10 GeV. For mass splittings down to

1832 3 GeV next-to-lightest neutralino masses are excluded up to 100 GeV.

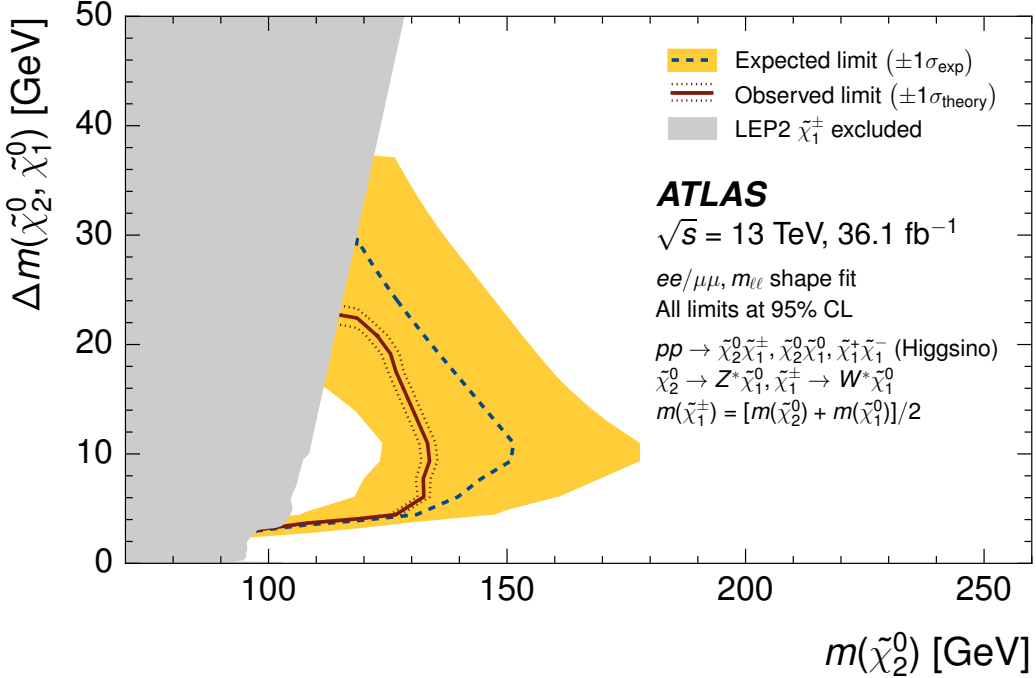


Figure 12.2: Expected 95% CL exclusion sensitivity (blue dashed line) with $\pm 1\sigma_{\text{exp}}$ (yellow band) from experimental systematics and observed limits (red solid) with $\pm 1\sigma_{\text{theory}}$ (dotted red) from signal cross section uncertainties. A shape fit of Higgsino signals to the $m_{\ell\ell}$ spectrum is used to derive the limit is displayed in the $m(\tilde{\chi}_2^0) - m(\tilde{\chi}_1^0)$ vs $m(\tilde{\chi}_2^0)$ plane. The chargino $\tilde{\chi}_1^\pm$ mass is assumed to be half way between the two lightest neutralinos. The grey region denotes the lower chargino mass limit from LEP [?].

1833 **12.2 Compressed Slepton**

1834 Figure 12.3 shows the 95% confidence interval limits set on the slepton simpli-
1835 fied model projected onto the plane defined by the mass difference between the slepton
1836 and lightest neutralino as a function of the slepton mass. These limits are based on
1837 an exclusion fit that exploits the shape of the m_{T2} spectrum from the exclusive slepton
1838 signal regions and exclude slepton masses up to 180 GeV for mass splittings down to
1839 5 GeV. For mass splittings down to 1 GeV slepton masses are excluded up to 70 GeV.
1840 In slepton simplified models, a fourfold degeneracy is assumed between the left and
1841 right-handed selectrons and smuons: $\tilde{e}_R = \tilde{e}_L = \tilde{\mu}_R = \tilde{\mu}_L =$.

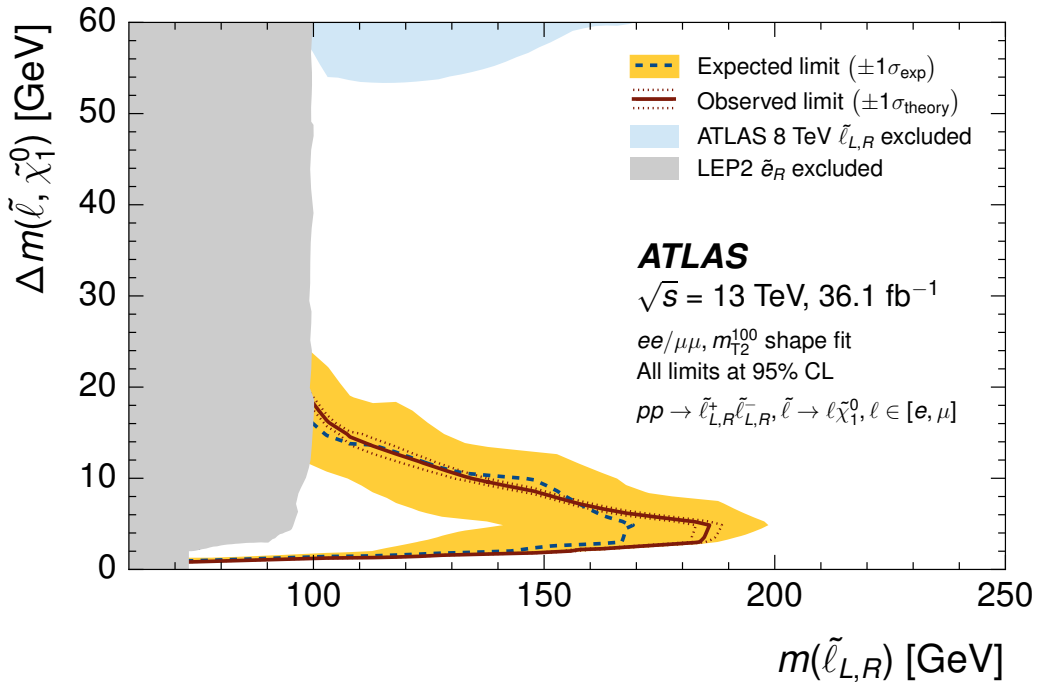


Figure 12.3: Expected 95% CL exclusion sensitivity (blue dashed line) with $\pm 1\sigma_{\text{exp}}$ (yellow band) from experimental systematics and observed limits (red solid) with $\pm 1\sigma_{\text{theory}}$ (dotted red) from signal cross section uncertainties. A shape fit of slepton signals to the m_{T2}^{100} spectrum is used to derive the limit projected into the $m(\tilde{\ell}) - m(\tilde{\chi}_1^0)$ vs $m(\tilde{\ell})$ plane. The slepton $\tilde{\ell}$ refers to a 4-fold mass degenerate system of left- and right-handed selectron and smuon. The grey region denotes a conservative right-handed smuon $\tilde{\mu}_R$ mass limit from LEP [?], while the blue region is the 4-fold mass degenerate slepton limit from ATLAS Run 1 [?].

1842 **12.3 Compressed Wino**

1843 The 95% confidence level intervals for the wino-bino simplified model are shown
1844 in Figure 12.4. Just like in the Higgsino exclusion plot, these limits are based on an
1845 exclusion fit that exploits the shape of the dilepton invariant mass spectrum from the
1846 exclusive electroweakino signal regions. Exclusion limits are projected onto the mass
1847 difference $\Delta m(\tilde{\chi}_2^0, \tilde{\chi}_1^0)$ plane as a function of the $\tilde{\chi}_2^0$ mass. For wino-bino simplified mod-
1848 els, next-to-lightest neutralino masses are excluded up to 170 GeV for mass splittings
1849 above 10 GeV, and excluded up to 100 GeV for mass splittings down to 2.5 GeV.

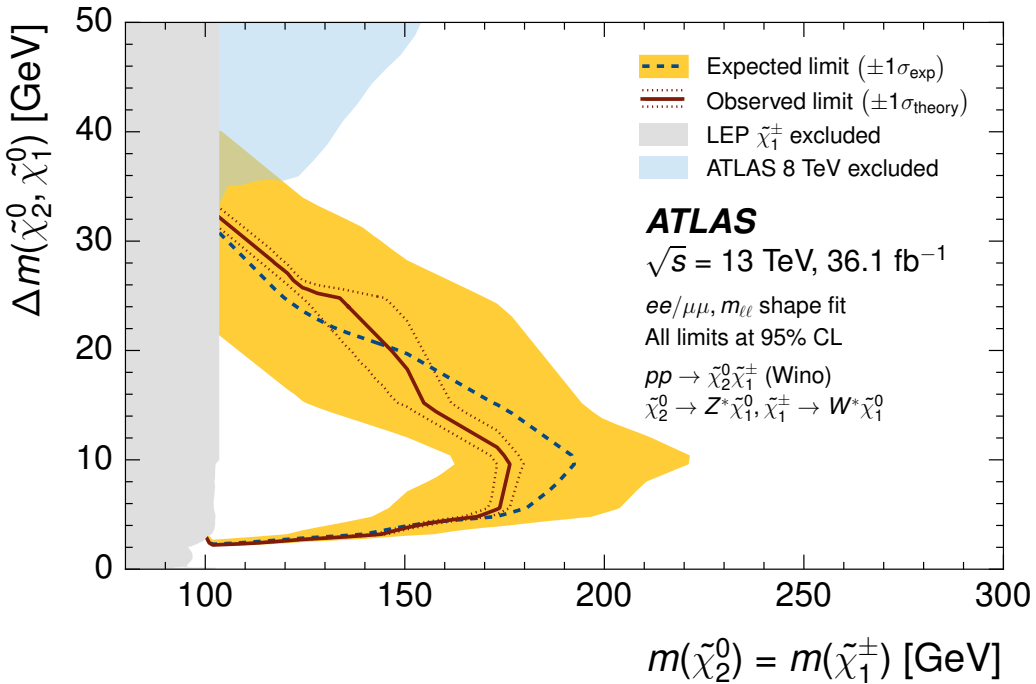


Figure 12.4: Expected 95% CL exclusion sensitivity (blue dashed line) with $\pm 1\sigma$ exp (yellow band) from experimental systematic uncertainties and observed limits (red solid line) with $\pm 1\sigma$ theory (dotted red line) from signal cross-section uncertainties for simplified models direct wino production. A shape fit of wino signals to the $m_{\ell\ell}$ spectrum is used to derive the limit is displayed in the $m(\tilde{\chi}_2^0) - m(\tilde{\chi}_1^0)$ vs $m(\tilde{\chi}_2^0)$ plane. The chargino $\tilde{\chi}_1^\pm$ mass is assumed equal to the $m(\tilde{\chi}_2^0)$ mass. The grey region denotes the lower chargino mass limit from LEP [?], and the blue region in the lower plot indicates the limit from the 2 ℓ +3 ℓ combination of ATLAS Run 1.

1850 **Chapter 13**

1851 **Conclusion**

1852 A search for supersymmetry in scenarios with compressed mass spectra was
1853 performed using ATLAS data collected in 2015 and 2016 at $\sqrt(s)$ 13 TeV, corresponding
1854 to $36.1 fb^{-1}$. We searched for directly produced electroweakinos and sleptons in events
1855 containing two soft, oppositely signed and same flavored leptons and including missing
1856 transverse momentum energy recoiling against initial state hadronic radiation. The
1857 directly produced electroweakinos and sleptons subsequently decay to their Standard
1858 Model partners and the lightest SUSY particle which is nearly degenerate in mass. No
1859 significant excess in data over Standard Model background was found; therefore, results
1860 were consistent with Standard Model prediction.

¹⁸⁶¹ **Appendix A**

¹⁸⁶² **Appendix A**

¹⁸⁶³ Auxiliary fake factor materials

¹⁸⁶⁴ **A.1 Fake lepton composition study**

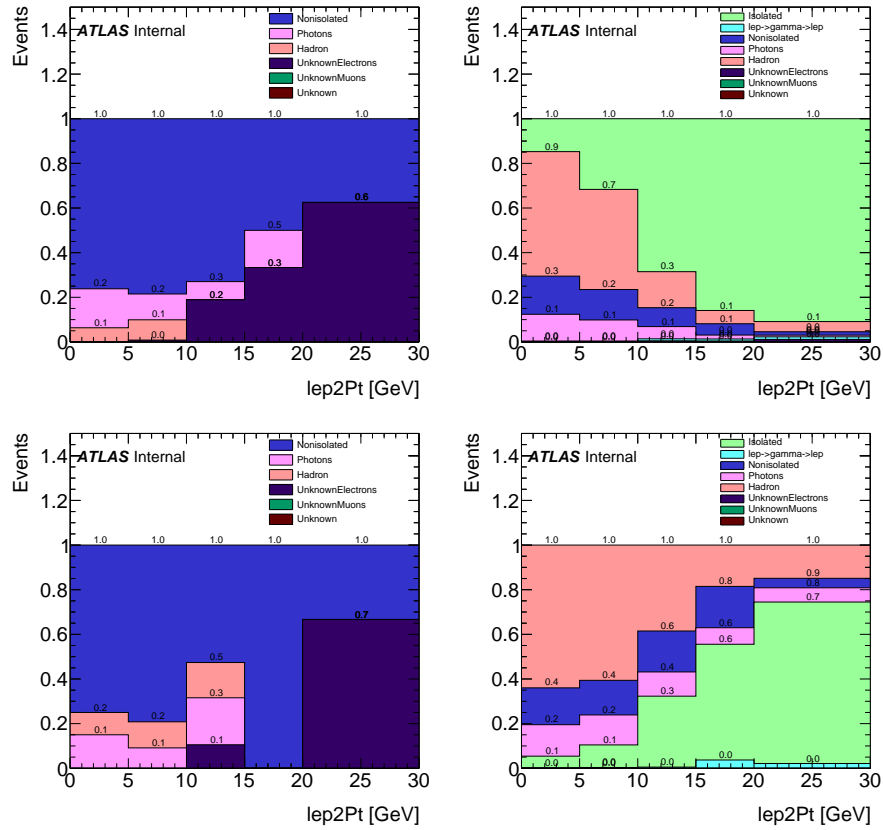


Figure A.1: Fake lepton composition in opposite sign signal and control region as a function of leading and subleading lepton p_T , with and without prompt (“Isolated” plus “ $\text{lep} \rightarrow \text{gamma} \rightarrow \text{lep}$ ”) leptons, for opposite sign electron pairs in the signal region.

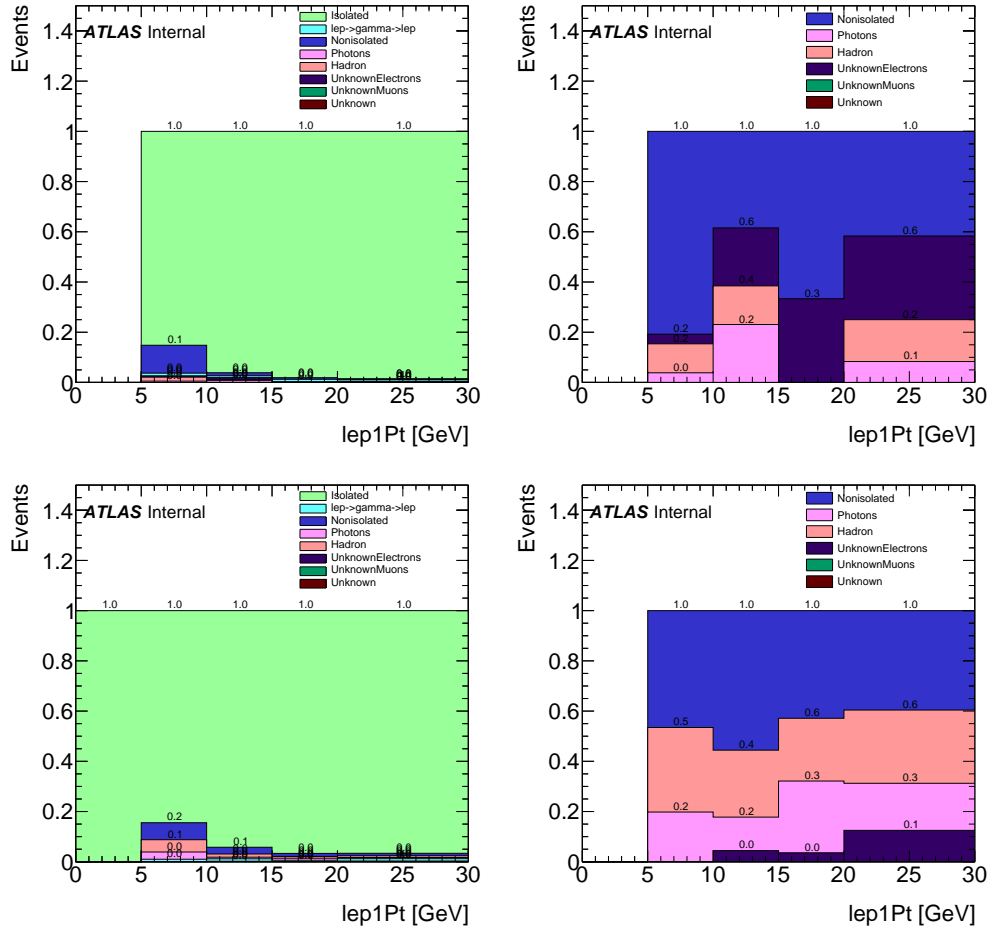


Figure A.2: Fake lepton composition as a function of leading and subleading lepton p_T , with and without prompt (“Isolated” plus “ $\text{lep} \rightarrow \text{gamma} \rightarrow \text{lep}$ ”) leptons, for opposite sign electron pairs in the signal region.

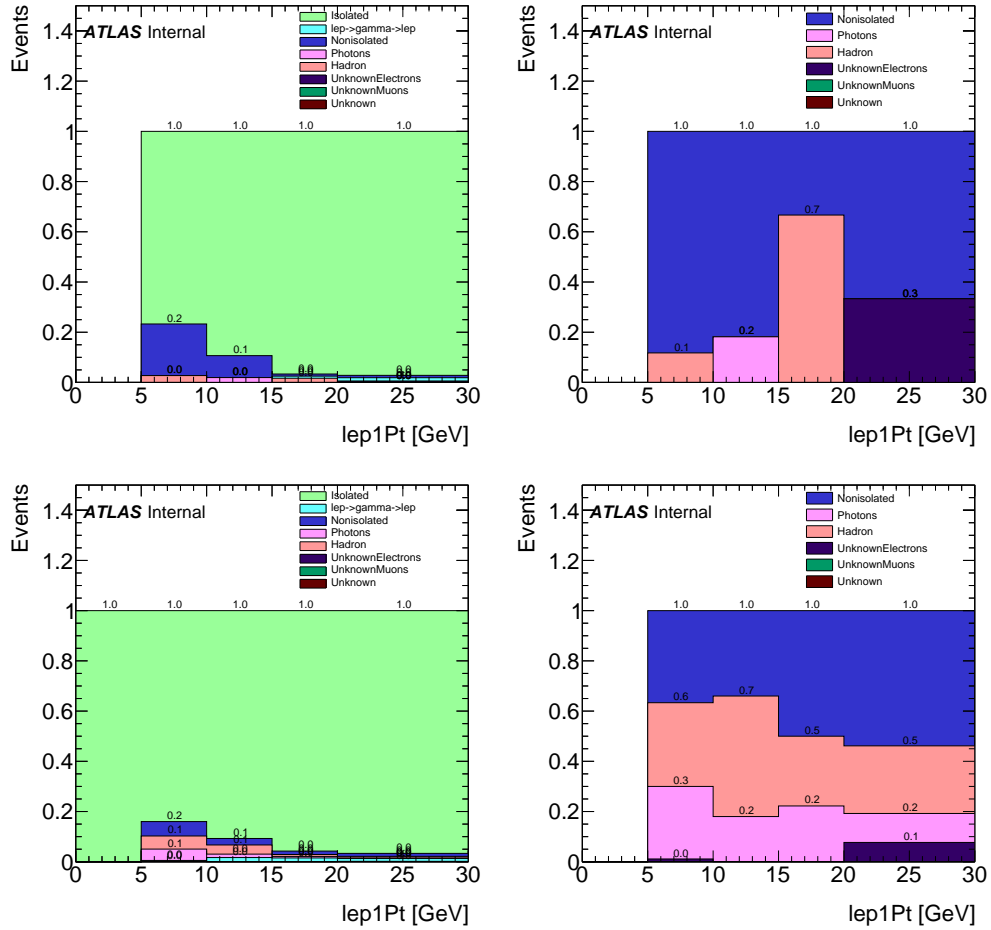


Figure A.3: Fake lepton composition as a function of leading and subleading lepton p_T , with and without prompt (“Isolated” plus “ $\text{lep} \rightarrow \text{gamma} \rightarrow \text{lep}$ ”) leptons, for same sign electron pairs in the signal region.

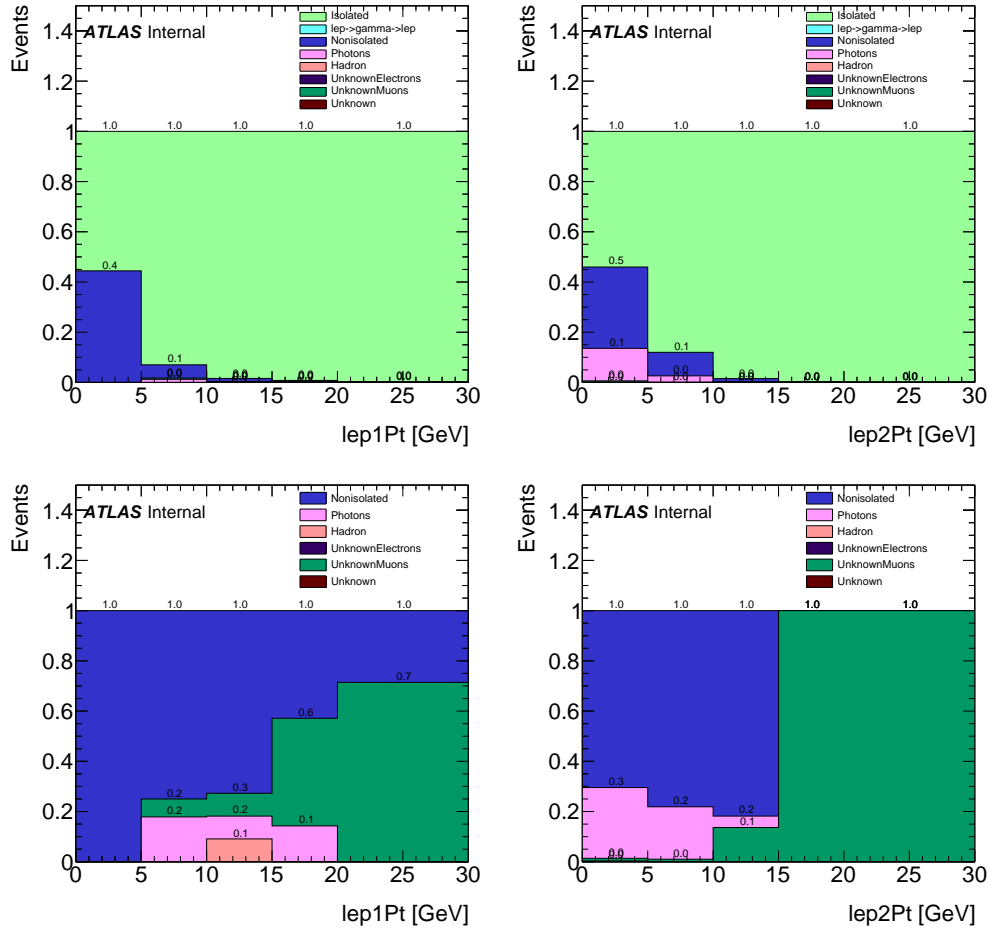


Figure A.4: Fake lepton composition as a function of leading and subleading lepton p_T , with and without prompt (“Isolated” plus “ $\text{lep} \rightarrow \text{gamma} \rightarrow \text{lep}$ ”) leptons, for opposite sign muon pairs in the signal region.

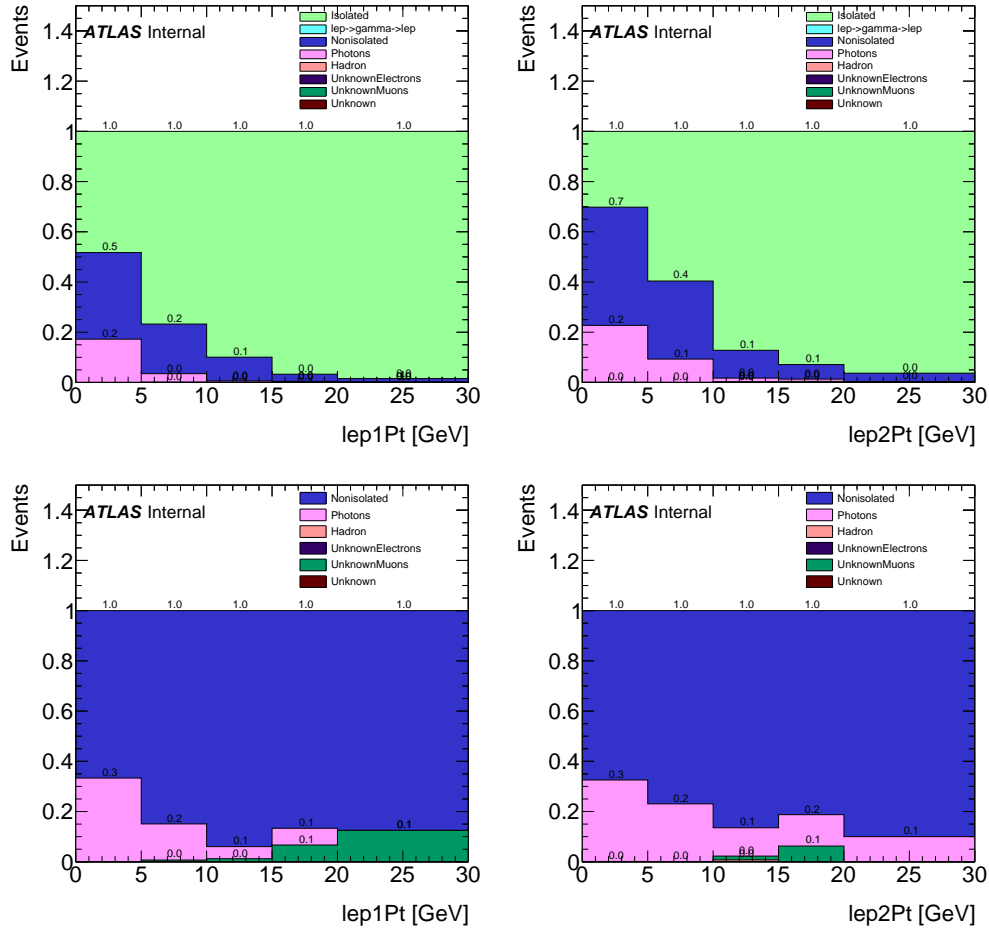


Figure A.5: Fake lepton composition as a function of leading and subleading lepton p_T , with and without prompt (“Isolated” plus “ $\text{lep} \rightarrow \text{gamma} \rightarrow \text{lep}$ ”) leptons, for opposite sign muon pairs in the fake lepton control region.

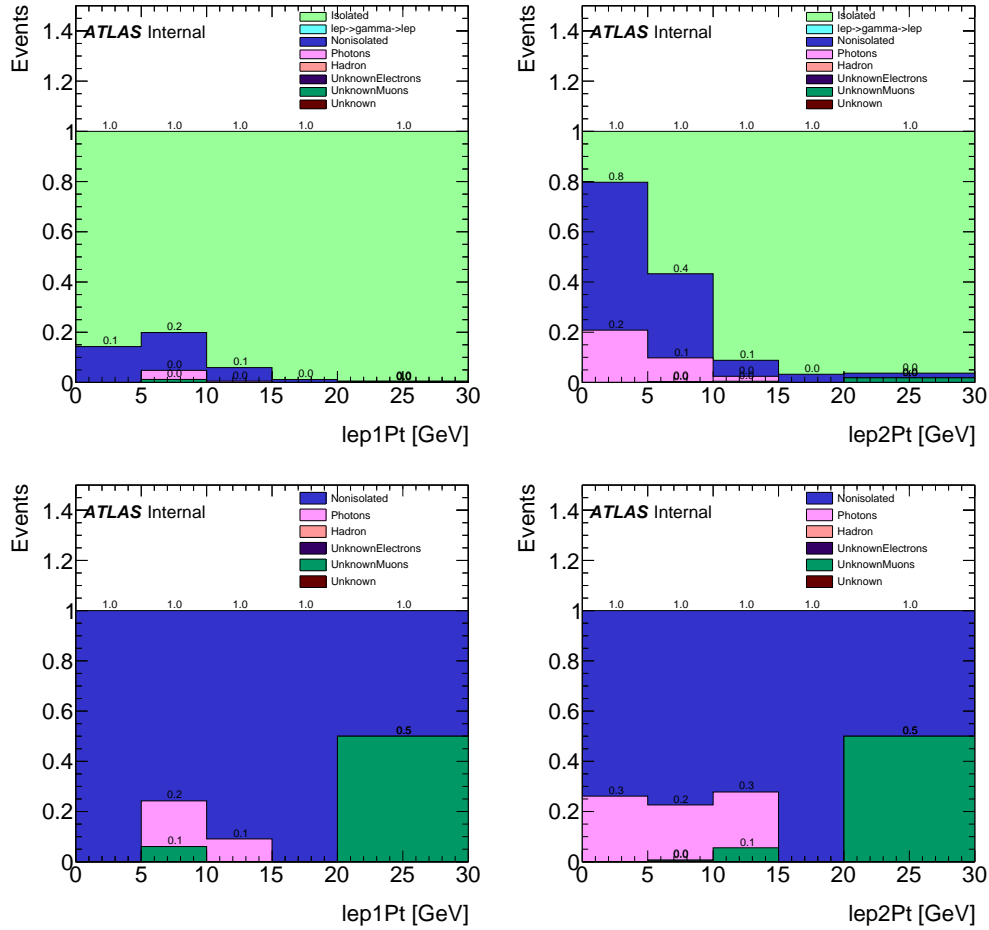


Figure A.6: Fake lepton composition as a function of leading and subleading lepton p_T , with and without prompt (“Isolated” plus “le γ →γ→le γ ”) leptons, for same sign muon pairs in the signal region.

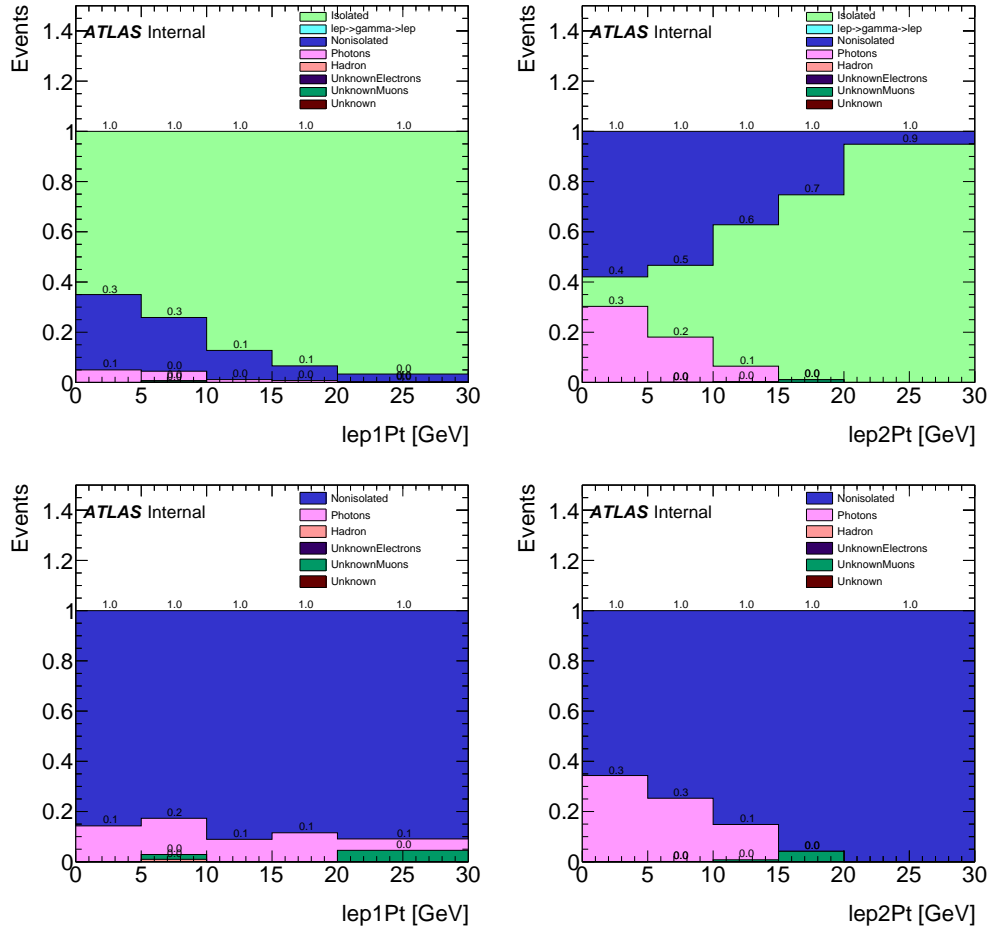


Figure A.7: Fake lepton composition as a function of leading and subleading lepton p_T , with and without prompt (“Isolated” plus “ $\text{lep} \rightarrow \text{gamma} \rightarrow \text{lep}$ ”) leptons, for same sign muon pairs in the fake lepton control region.

¹⁸⁶⁵ **Appendix B**

¹⁸⁶⁶ **Appendix B**

¹⁸⁶⁷ Auxiliary CR and VR material

¹⁸⁶⁸ **B.1 Control Region Plots**

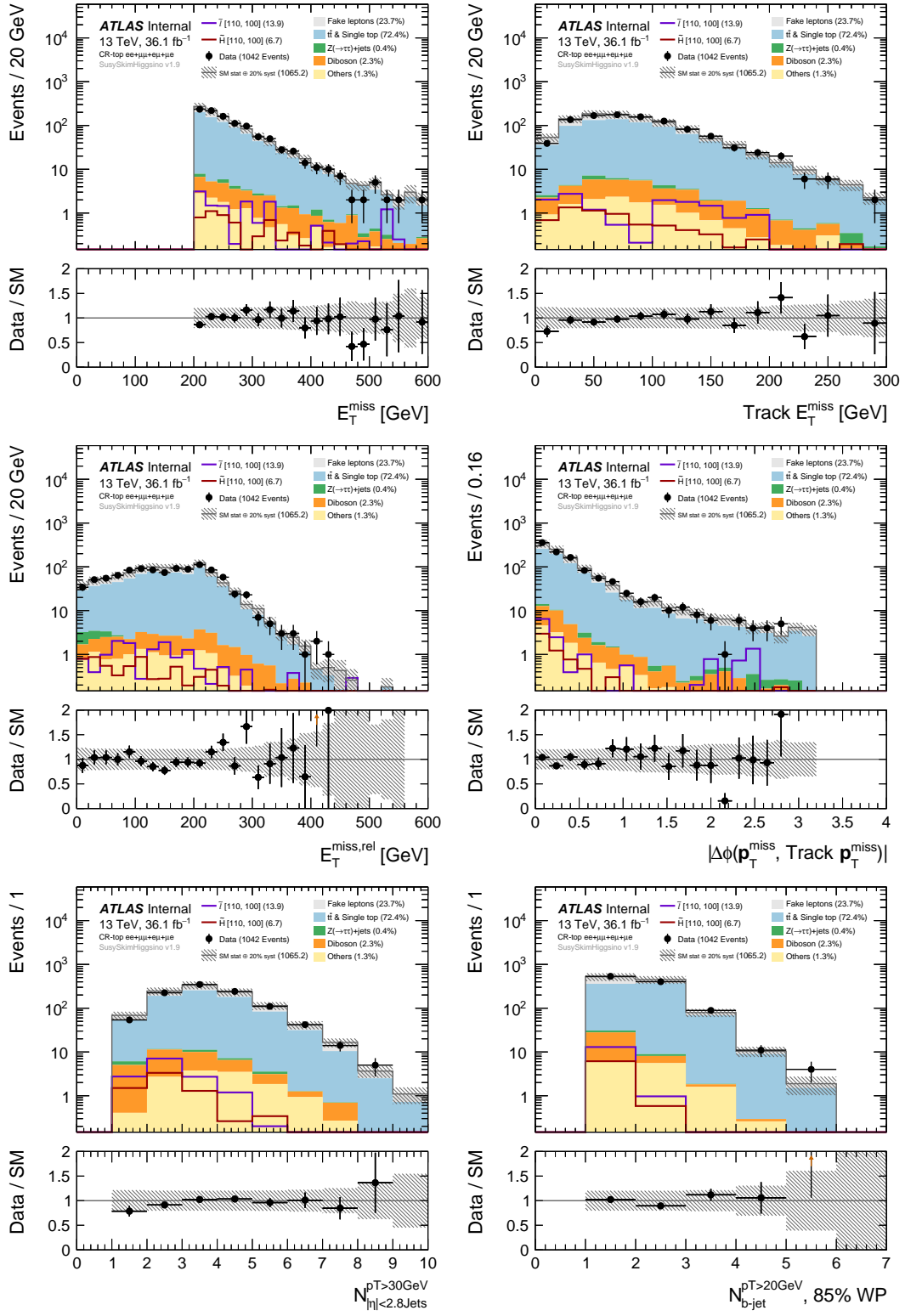


Figure B.1: CR-top $ee + \mu\mu + e155\mu e$ channel, pre-fit distributions.

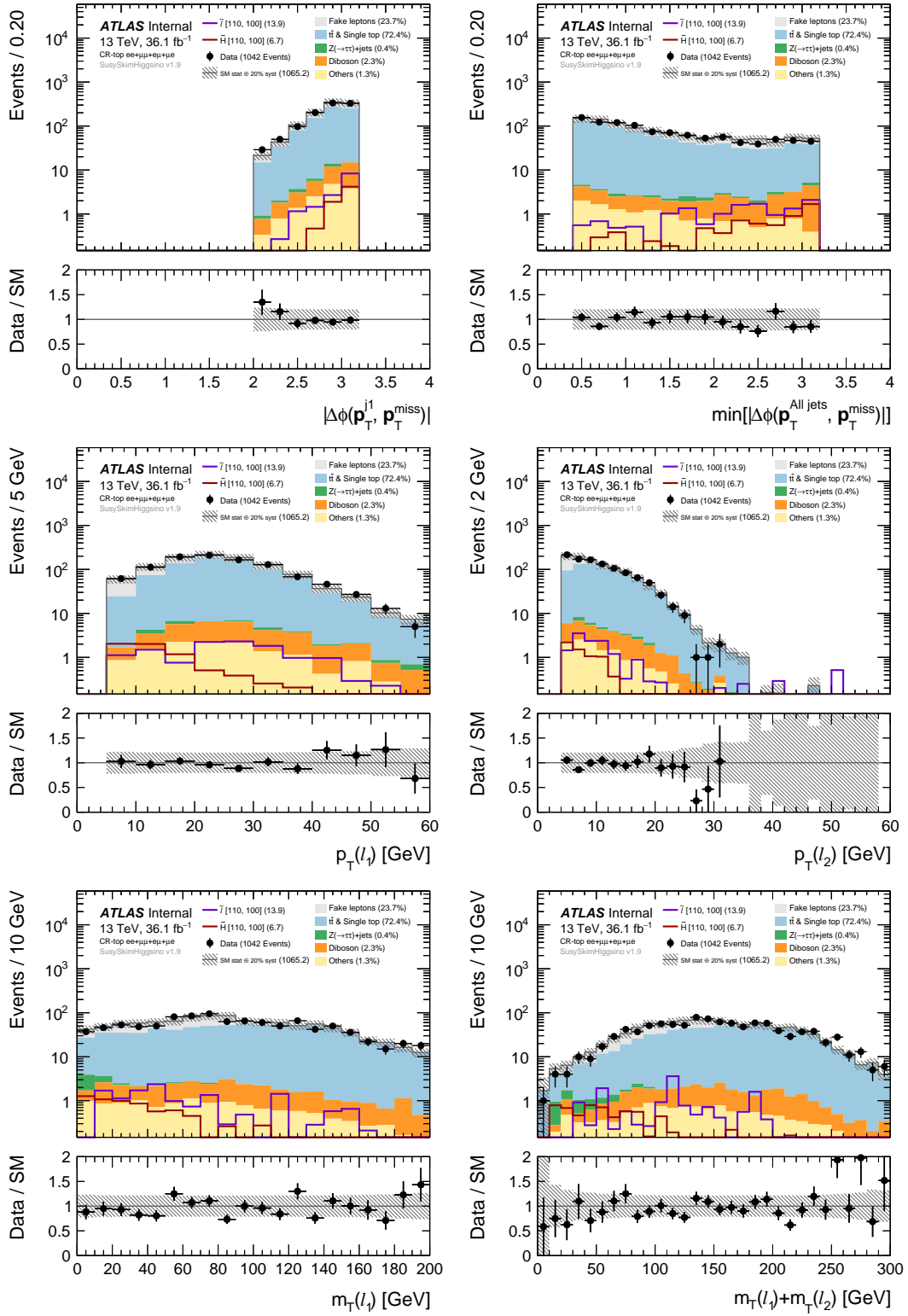


Figure B.45 $\ell_1 + m_T^{\ell_1}$

Figure B.3: CR-top $ee + \mu\mu + e\mu + \mu e$ channel, pre-fit distributions.

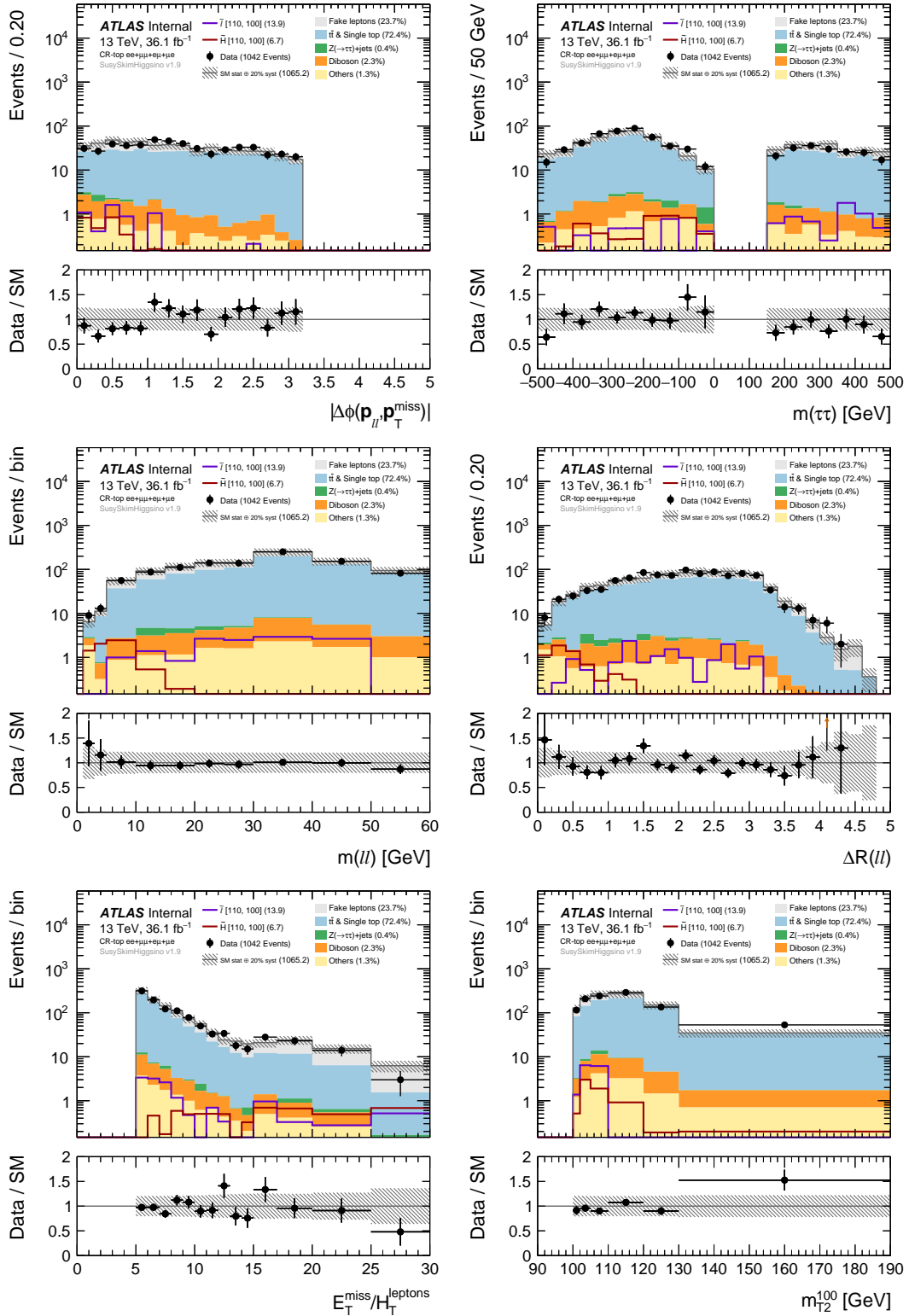


Figure B.5: m_{T2}^{100}

Figure B.5: CR-top $ee + \mu\mu + e\mu + \mu e$ channel, pre-fit distributions.

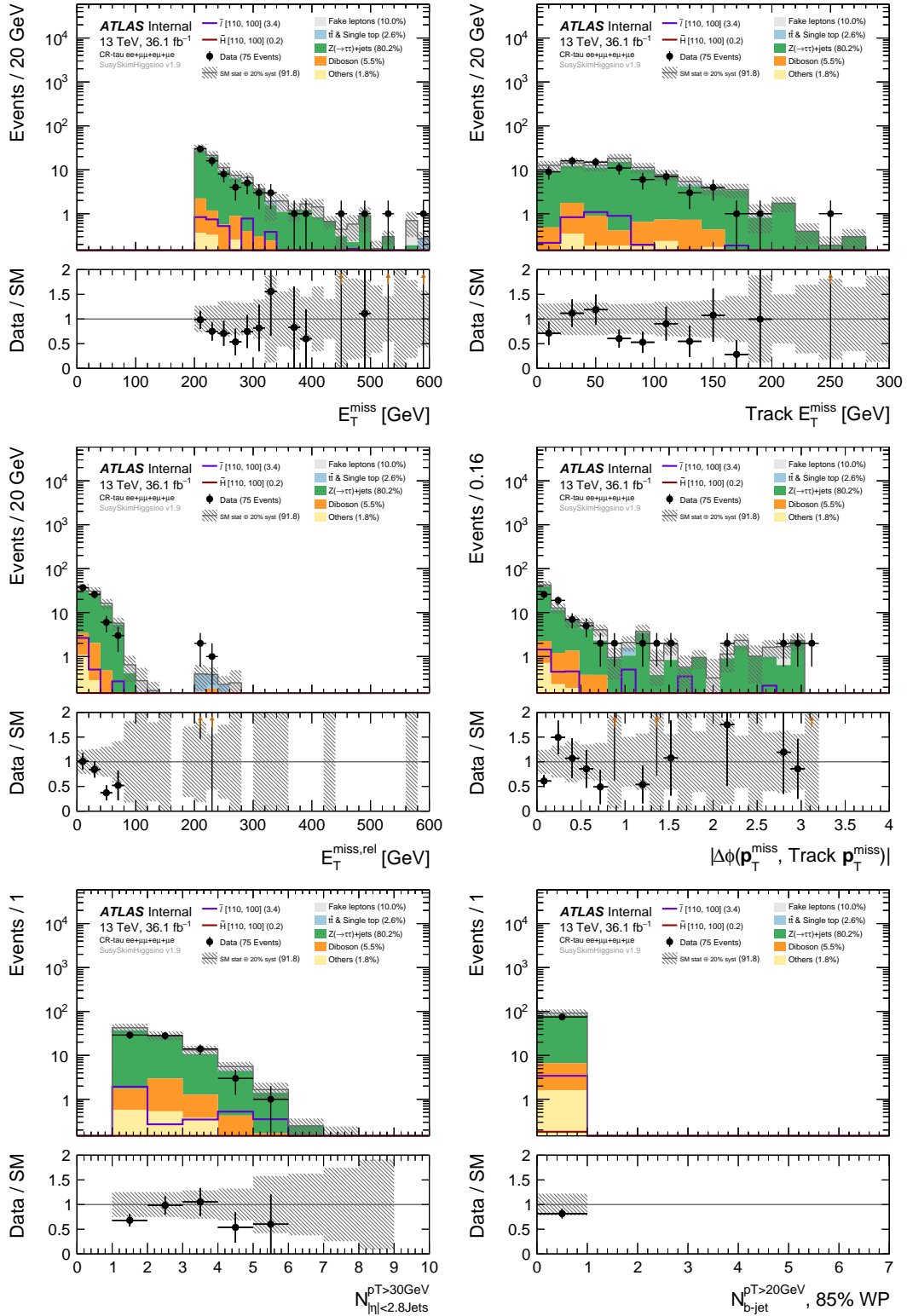


Figure B.6: CR-tau $ee + \mu\mu + e158\mu e$ channel, pre-fit distributions.

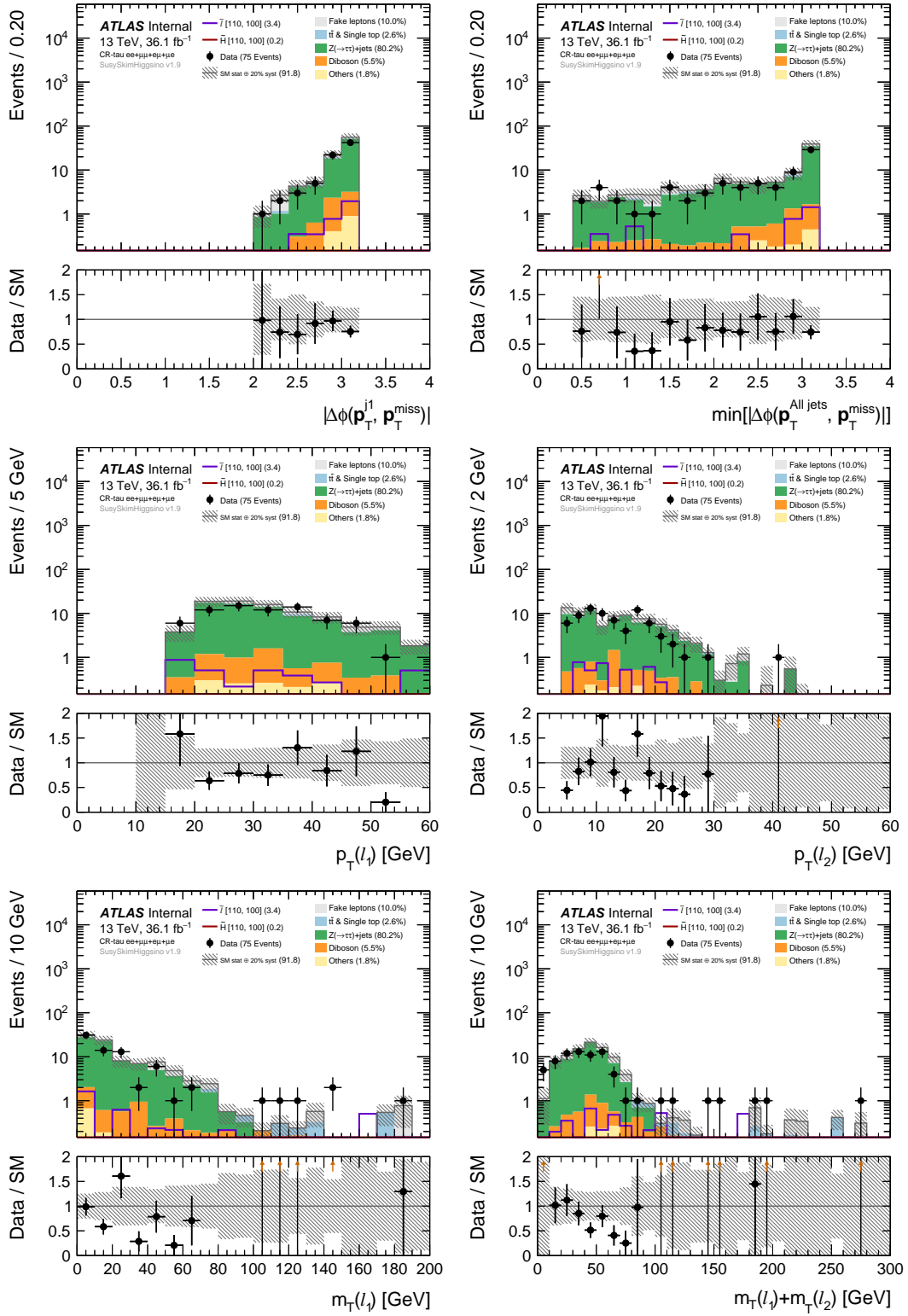


Figure B.7: CR-tau ee + $\mu\mu$ + e159 μe channel, pre-fit distributions.

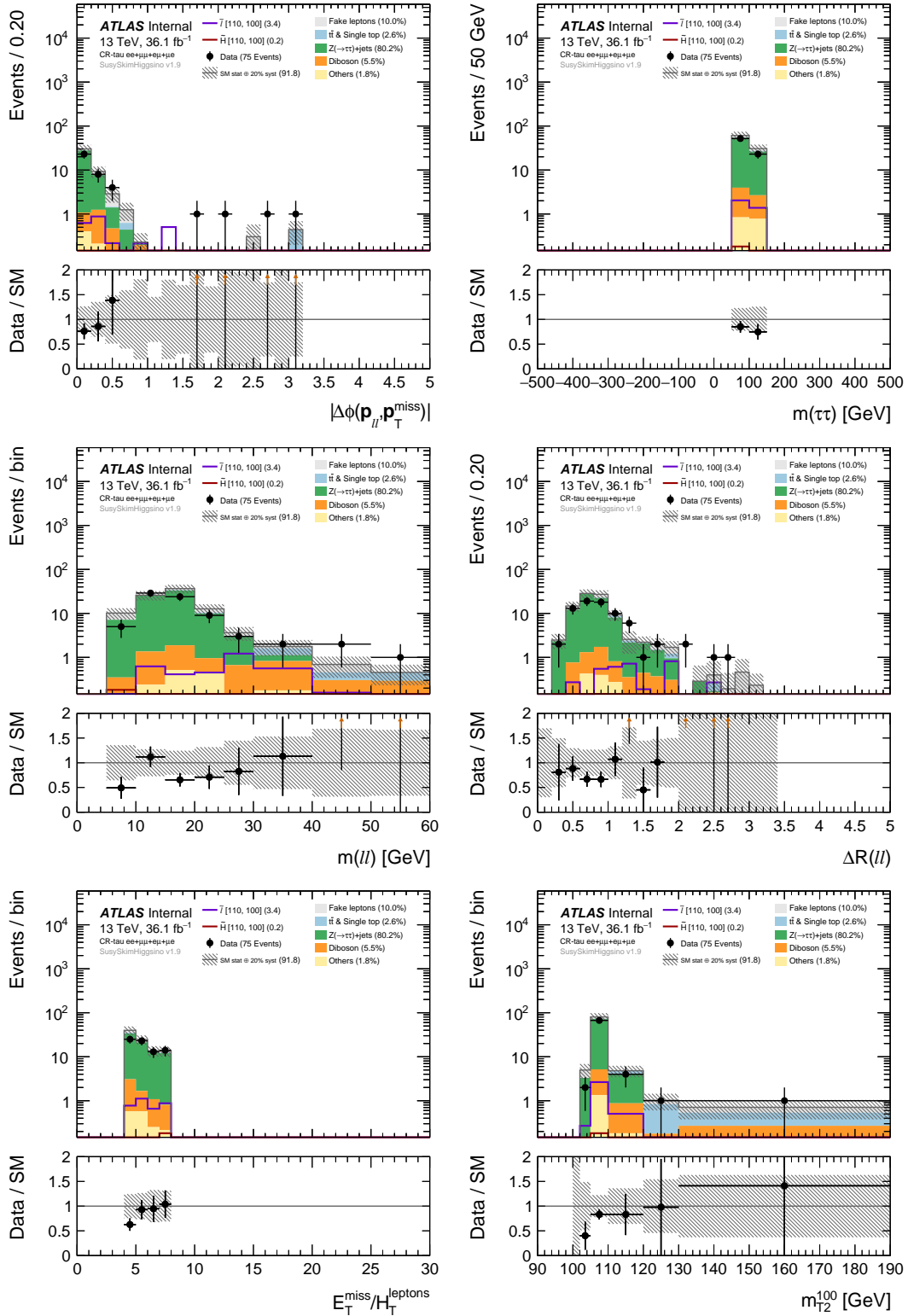


Figure B.8: CR-tau $ee + \mu\mu + e160\mu e$ channel, pre-fit distributions.

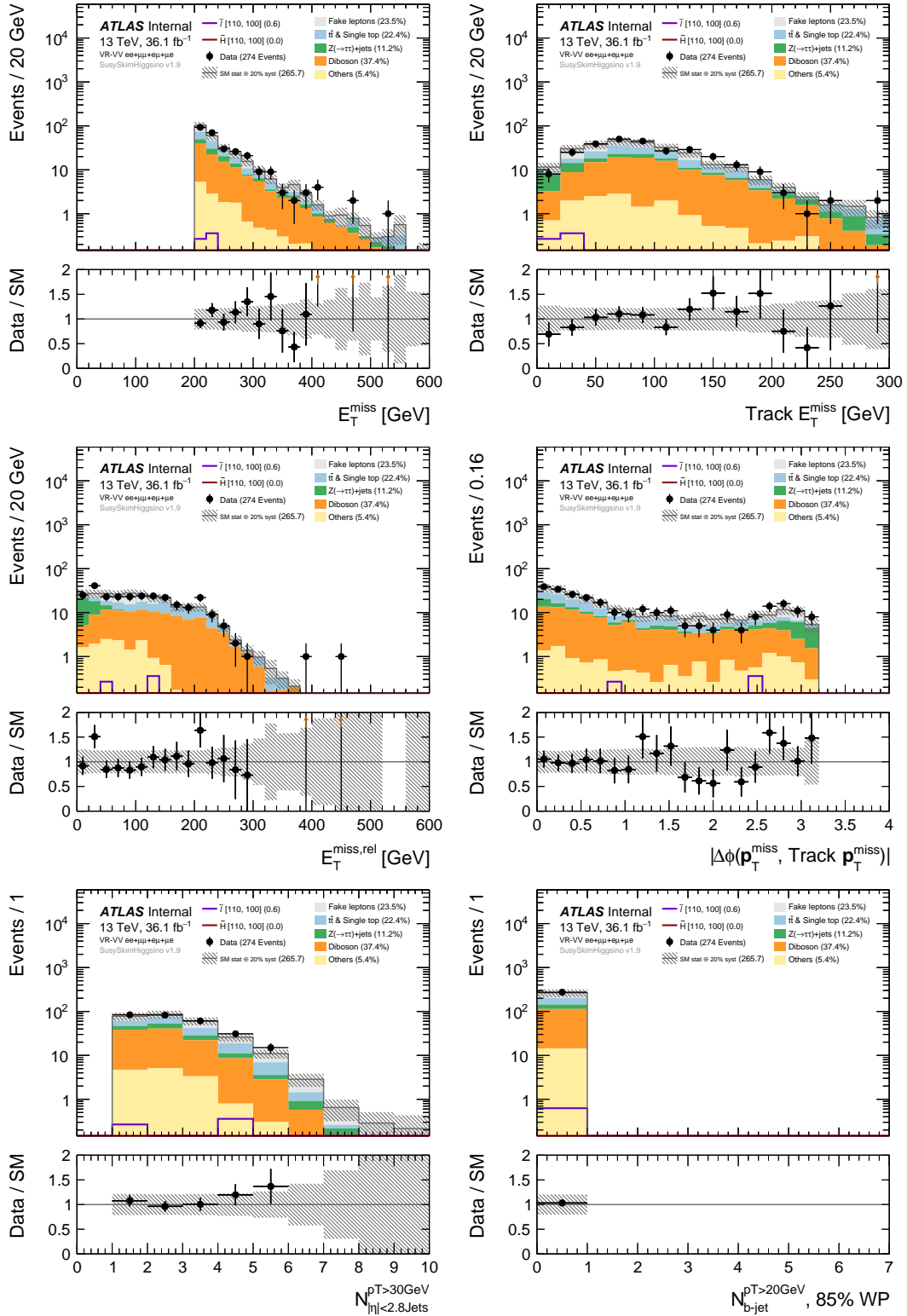


Figure B.9: VR-VV $ee + \mu\mu + eT_{miss}$ channel, pre-fit distributions.

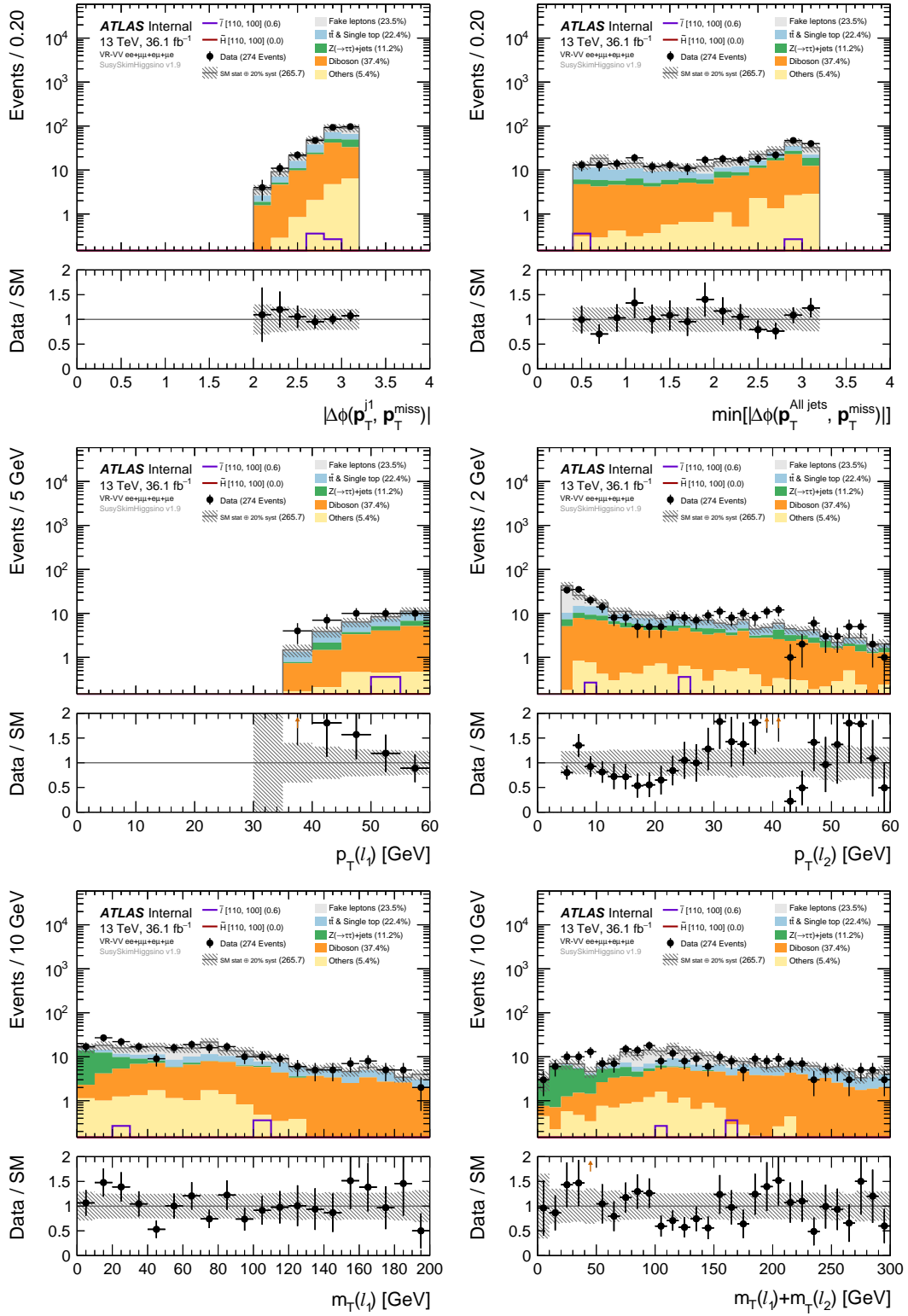


Figure B.10: VR-VV $ee + \mu\mu + e162\mu e$ channel, pre-fit distributions.

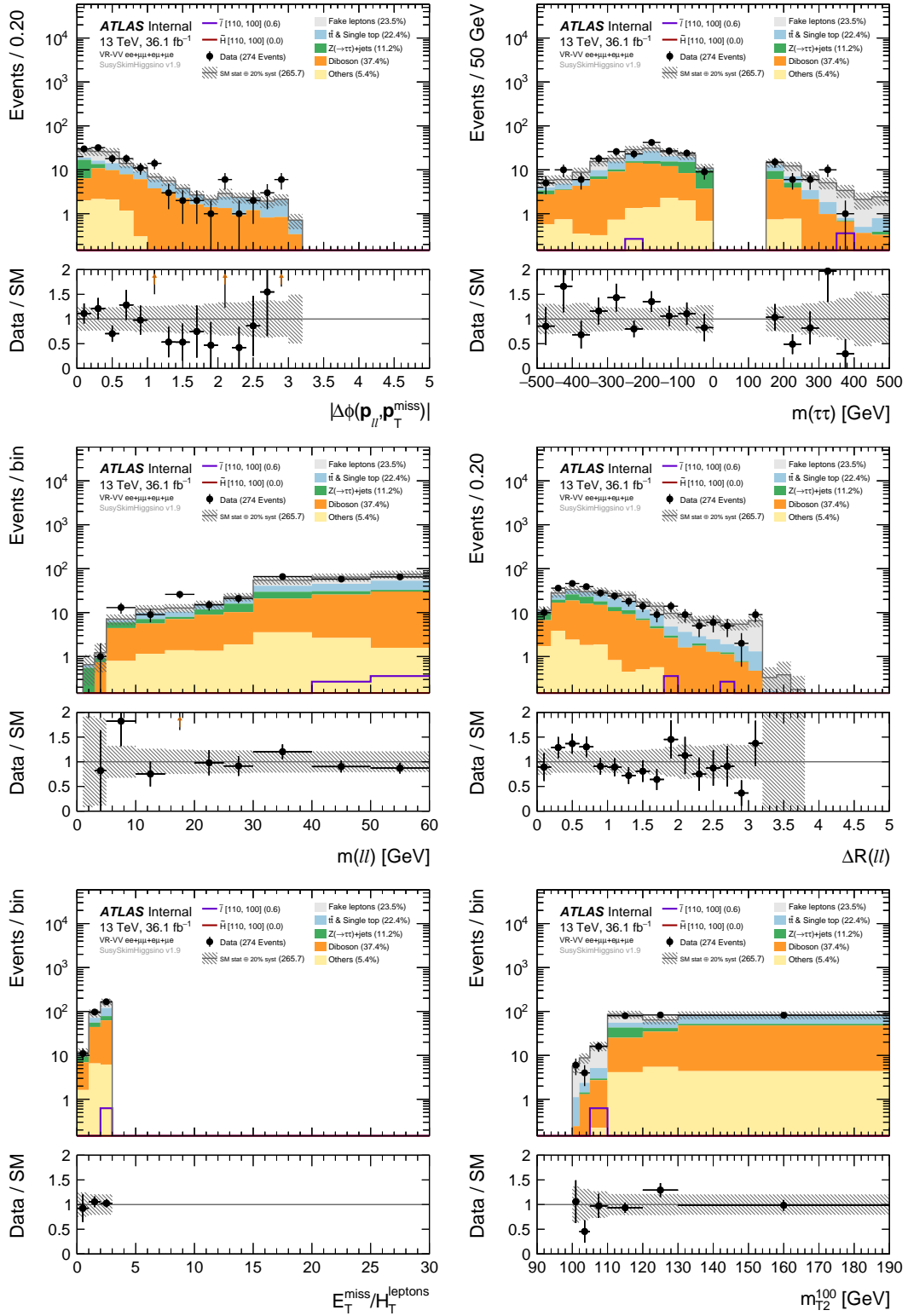


Figure B.11: VR-VV $ee + \mu\mu + e$ channel, pre-fit distributions.

1869 Ancillary material should be put in appendices, which appear after the bibli-
1870 ography.